WARSAW UNIVERSITY OF TECHNOLOGY

Ph.D. Thesis

Discipline of Science: Chemical Sciences /
Field of Science: Natural Sciences

Juhi, M.Sc.

Design and Characterization of $CsPbCl_3$ Perovskite-Based Anodes and Artificial SEI in Lithium Batteries

Supervisors
Professor **Władysław Wieczorek,** Ph.D., D.Sc.
Professor **Robert Dominko,** Ph.D.

Warsaw 2025

Acknowledgements

As this amazing journey comes to an end, I am deeply grateful to everyone who has guided, mentored, and supported me throughout my PhD. I sincerely thank my supervisors, Prof. Dr. Władysław Wieczorek and Prof. Dr. Robert Dominko, for their constant guidance, encouragement, and trust, which have shaped me both as a researcher and as a person.

My heartfelt thanks to my wonderful NIC lab mates: Mariana, Luis, Ahmad, Lana, Burcu, and Rabail, for their friendship and support. I am especially grateful to Dr. Elena Chernyshova and Dr. Sara Drvari Talian for their invaluable help with XPS and EIS, and to Nikhil Subhash and Prof. Dr. Andrzej Ostrowski for assistance with XRD measurements. I also thank my colleagues at WUT: Eva Del Campo Ortiz, Aginmariya Kottarathil, and Aleksandra Ossowska, for their support, and Karol Jagodziński from CIC energiGUNE for providing Si-anodes.

I would like to express my appreciation to Prof. Christian Masquelier for welcoming me into an inspiring research community, and to Louise Vrand and Béatrice Messana for their kind and efficient coordination.

I acknowledge the funding from the DESTINY PhD Programme (European Union's Horizon 2020 Research and Innovation Programme) under the Marie Skłodowska-Curie Actions COFUND (Grant Agreement No. 945357). I also acknowledge the financial support of the Slovenian Research and Innovation Agency through Grant P2-0423. The support from the PSIONIC Project, which has received funding from the European Union's Horizon Europe Research and Innovation Programme under Grant Agreement No. 101069703, is also acknowledged. I further gratefully acknowledge the National Science Centre, Poland, for financial support through Grants OPUS 2021/41/B/ST5/04450 and MAESTRO 11 No. 2019/34/A/ST5/00416. Financial support from the Slovenian Research and Innovation Agency (Grants P2-0423 and Z2-4465) is also acknowledged.

NATIONAL INSTITUTE
OF CHEMISTRY

Abstract

The demand for higher energy density and improved stability in Li-ion batteries (LIBs) has driven significant interest in the development of alternative anode materials and interfacial engineering strategies. While graphite remains the commercial standard due to its affordability and structural integrity, its low theoretical capacity (372 mAh/g) and unstable solid electrolyte interphase (SEI) limit its long-term performance. Li-metal, with its ultrahigh theoretical capacity, presents a compelling alternative but suffers from dendritic growth and unstable SEI formation. This research explores the use of cesium lead chloride ($CsPbCl_3$), both as an anode material and as a protective interfacial coating for Li, graphite, and Si electrodes.

In the first part of the study, $CsPbCl_3$ was investigated as an active anode material in half-cell configurations using a liquid electrolyte system. The cells delivered initial discharge capacities of ~ 600 mAh/g. Post-cycling XPS and XRD analyses revealed a multi-step Li-ion storage mechanism, conversion and alloying reactions.

In the second part, $CsPbCl_3$ was applied as a protective coating on Li-metal anodes using a simple drop-casting method. Electrochemical evaluation in symmetric (Li||Li), asymmetric (Li||Cu), and full cell (Li||LFP) configurations demonstrated that the coating effectively suppresses dendrite formation, enhances interfacial stability, and improves cycling performance.

Finally, the same coating strategy was applied to graphite and Si electrodes. The $CsPbCl_3$ layer was shown to improve the electrochemical stability of half-cells, likely by regulating SEI formation and protecting the electrode surface.

Overall, this work demonstrates the versatility of $CsPbCl_3$ as both an active material and an interfacial layer, highlighting its potential in the advancement of high-performance Li-based energy storage systems.

Keywords:
Li-ion batteries, lithium metal anode, graphite, silicon anode, $CsPbCl_3$, perovskite, solid electrolyte interphase (SEI)

Streszczenie

Zapotrzebowanie na baterie litowo-jonowe (LIB) o większej gęstości energii i lepszej stabilności spowodowało znaczne zainteresowanie opracowaniem alternatywnych materiałów anodowych i nowych strategii prowadzących do poprawy charakterystyki międzyfazowej elektroda- elektrolit. Chociaż grafit pozostaje standardem komercyjnym ze względu na swoją przystępną cenę i integralność strukturalną, jego niska pojemność teoretyczna (372 mA/g) i niestabilna warstwa międzyfazowa na granicy faz elektroda - elektrolit (SEI) ograniczają czas pracy ogniw i stabilność uzyskiwanych z nich pojemności. Metaliczny lit, dzięki swojej ultra wysokiej teoretycznej pojemności, stanowi atrakcyjną alternatywę dla ogniw litowo-jonowych na bazie grafitu. Jego wykorzystanie ogranicza wysoka reaktywność litu prowadząca do powstawania i wzrostu warstw dendrytów w ogniwie i niestabilne tworzenie się SEI. Celem mojej pracy jest poprawa właściwości granicy faz elektroda elektrolit w szeregu typach baterii litowo-jonowych, jak również w ogniwach z anodą z metalicznego litu poprzez wykorzystanie chlorku ołowiowo- cezowego ($CsPbCl_3$) o strukturze perowskitu.

W pierwszej części pracy $CsPbCl_3$ został zbadany jako aktywny materiał anodowy w półogniwach z wykorzystaniem elektrolitu ciekłego. Ogniwa te osiągnęły początkową pojemność rozładowania w zakresie od 600 mAh/g . Analizy XPS i XRD przeprowadzone po zakończeniu cyklu ładowania, rozładowania ogniwa wykazały wieloetapowy mechanizm magazynowania litu zachodzący w wyniku reakcji konwersji i stopowania.

W drugiej części pracy zastosowano $CsPbCl_3$ jako powłokę ochronną na anodach litowych. Warstwy perowskitu nanoszono na powierzchnię elektrod metodą prostego odlewania kroplowego. Badania elektrochemiczne w konfiguracjach symetrycznych (Li||Li), asymetrycznych (Li||Cu) półogniw i w pełnych ogniwach (Li||LFP) wykazały, że powłoka taka skutecznie hamuje tworzenie się dendrytów, zwiększa stabilność międzyfazową i znaczącą zwiększa ilość cykli pracy ogniwa.

Tą samą strategię zastosowano do powlekania elektrod grafitowych i krzemowych. Wykazano, że warstwa $CsPbCl_3$ poprawia stabilność elektrochemiczną półogniw, poprzez tworzenie się SEI o odpowiednie strukturze pozwalającej na skuteczną ich ochronę powierzchni elektrody.

Uzyskane wyniki wskazują na wszechstronność $CsPbCl_3$ zarówno jako materiału aktywnego, jak i warstwy międzyfazowej, podkreślając jego potencjalne zastosowanie w wysokowydajnych systemów magazynowania energii w tym ogniwach z anodą z metalicznego litu.

Słowa kluczowe:
baterie litowo-jonowe, anoda litowo-metaliczna, grafit, anoda krzemowa, $CsPbCl_3$, perowskit, międzyfazowa warstwa elektrolitu (SEI)

Table of Contents

List of Abbreviations

ABX_3 – Perovskite general formula

AC – Alternating Current

ACS – American Chemical Society

ASEI – Artificial Solid Electrolyte Interphase

BE – Binding Energy

CAGR – Compound Annual Growth Rate

CBM – Conduction Band Minimum

CE – Coulombic Efficiency

CNT – Carbon Nanotube

CPB – Cesium Lead Bromide

CR2450 – Coin Cell type

CV – Cyclic Voltammetry

DC – Direct Current

DEC – Diethyl Carbonate

DFT – Density Functional Theory

DME – Dimethoxyethane

DMSO – Dimethyl Sulfoxide

DOI – Digital Object Identifier

DOL – Dioxolane

EDX – Energy Dispersive X-ray Spectroscopy

EIS – Electrochemical Impedance Spectroscopy

EV – Electric Vehicle

FA – Formamidinium

FEC – Fluoroethylene Carbonate

LFP – Li Iron Phosphate

LIB – Li-Ion Battery

LMA – Li-metal Anode

LMB – Li-metal Battery

LP40 – Commercial electrolyte (1 M $LiPF_6$ in EC:DMC 1:1)

LRCS – Laboratoire de Réactivité et Chimie des Solides

LTO – Li Titanate

MA – Methylammonium

MHP – Metal Halide Perovskite

NMP – N-Methyl-2-pyrrolidone

OCV – Open Circuit Voltage

PC – Propylene Carbonate

PCE – Power Conversion Efficiency

PE – Polyethylene

PEIS – Potentiostatic Electrochemical Impedance Spectroscopy

PL – Photoluminescence

PVDF – Polyvinylidene Fluoride

RSC – Royal Society of Chemistry

SEI – Solid Electrolyte Interphase

SEM – Scanning Electron Microscopy

SDS – Sodium Dodecyl Sulfate

THF – Tetrahydrofuran

XPS – X-ray Photoelectron Spectroscopy

XRD – X-ray Diffraction

List of Figures

List of Tables

Chapter 1

Introduction

This chapter provides an introduction to the key topics explored in the thesis. It begins with highlighting the growing global need for renewable energy, particularly in electricity generation and energy storage, especially batteries. The chapter then explains the need to explore new battery materials.

Next, it introduces the fundamental properties of metal halide perovskites and factors affecting their physicochemical properties. This chapter then explains their role as a new class of materials in the fabrication of anodes and also protective coatings in Li-batteries. Moreover, this chapter explains the interaction between the Li-ion and the perovskites. Finally, it offers a brief overview of the structure and content of the thesis.

A part of this chapter has been published as a review in Journal of Materials Chemistry A: Juhi Juhi, Marcin Saski, Maria K. Kochaniec, Władyslaw Wieczorek, Robert Dominko, Janusz Lewiński. "Exploring Metal Halide Perovskites as Active Architectures in Energy Storage Systems." DOI: https://doi.org/10.1039/D5TA04267D

1.1. Energy Transition and Storage

In today's technological era, electrical energy has become one of the most vital resources for human survival. As the global population continues to grow, the power demand has surged dramatically. Traditionally, this demand has been met through the combustion of fossil fuels such as coal and oil. However, this approach releases harmful greenhouse gases such as CO_2, CO, and CH_4 into the environment, contributing significantly to air and water pollution, as well as global warming. To address these environmental concerns and the ongoing energy crisis, there is an urgent shift toward renewable energy sources such as solar, wind, hydropower, and geothermal energy.[1,2] Among these, solar energy is considered the most abundant and clean alternative to conventional energy generation. However, the intermittent nature of renewable

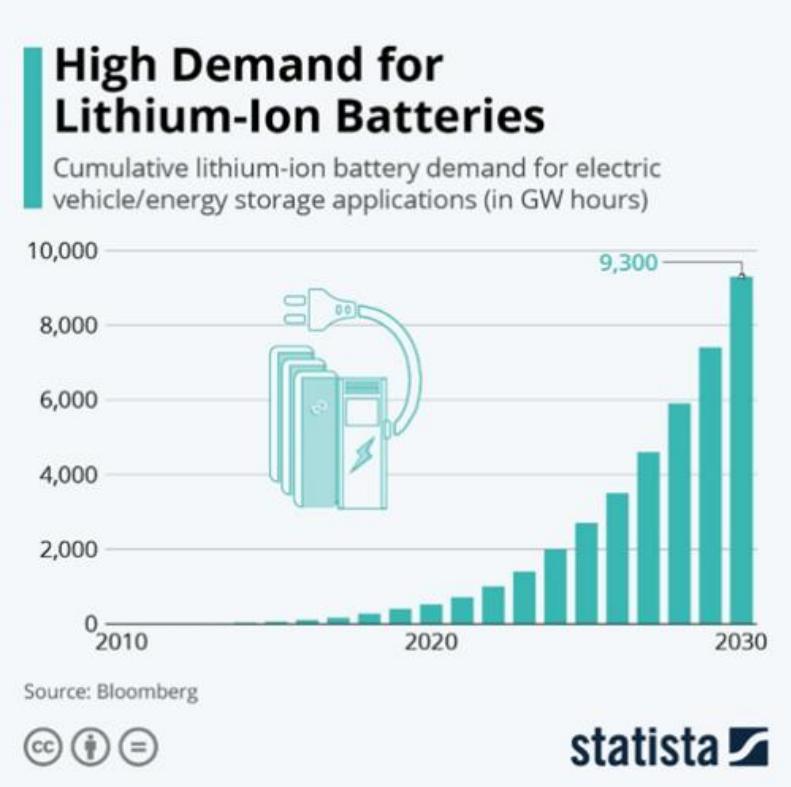

Fig. 1. Cumulative LIB demand in the energy storage market.[7]

sources presents a major challenge, highlighting the need for efficient and reliable energy storage systems. This need has become even more pressing in the context of the fourth technological revolution, which calls for advanced energy storage technologies like batteries to maximize the utility of electricity generated from renewable sources.[3,4] Among different battery technologies developed so far, Li-ion batteries (LIBs) currently represent the most widely adopted technology in the energy storage market. First developed in the late 1980s and

early 1990s, LIBs received global recognition with the awarding of the Nobel Prize in Chemistry in 2019. Their high energy density (100-265 Wh/kg) and power output have made them the benchmark for portable electronics and a key enabler in the transition to battery electric vehicles (BEVs).[5,6] The global LIB industry is projected to grow at a compound annual growth rate (CAGR) of 12.3% between 2021 and 2030, increasing from USD 41.1 billion to USD 116.6 billion. In 2010, global demand stood at just 0.5 gigawatt-hours (GWh); by 2020, it had reached 526 GWh. This demand is expected to soar even further, reaching an estimated 9,300 GWh by 2030 (Fig. 1)[7].

Despite their widespread success, LIBs still face critical challenges such as capacity degradation, safety concerns, and limited cycle life.[7,8] These limitations hinder their ability to fully support global decarbonization goals and highlight the urgent need for further research and innovation. Advancing LIB technology to the next generation, featuring longer lifespan, faster charging, improved safety, and reduced cost, relies heavily on breakthroughs in key components, including electrodes, electrolytes, and interfacial materials. Consequently, the scientific community must focus on the development of cost-effective, efficient, easily accessible, and durable energy storage materials. A deeper understanding of the underlying storage mechanisms, material properties, challenges, and future directions will be essential in driving this progress forward.

1.2. Basic concept of LIB

A LIB is a rechargeable battery that stores and releases energy through the movement of Li-ions between two electrodes, the anode (negative) and the cathode (positive), via an ion-conducting electrolyte. This movement of ions is fundamental to the battery's operation, enabling the conversion between chemical and electrical energy. During discharge, Li-ions migrate from the anode to the cathode through the electrolyte, while electrons travel through an external circuit, generating an electric current to power devices. In contrast, during charging, an external voltage forces Li-ions to move from the cathode back to the anode, reversing the process and restoring the battery's stored energy.[9] A key challenge in LIBs arises from side reactions, particularly at the electrode/electrolyte interface. On the anode side, especially during the first cycle, the electrolyte tends to decompose, forming a passivation layer known as the solid electrolyte interphase (SEI). This layer is critical for battery stability, as it allows Li-ion transport while preventing further electrolyte decomposition. Therefore, beyond

selecting an electrolyte with a wide electrochemical stability window, it is often advantageous to use formulations that deliberately react with the electrode to form a robust SEI. Overall, the performance and reliability of Li-ion batteries depend on the careful selection and interaction of active materials, conductive additives, binders, and electrolyte components.[10] Fig. 2 illustrates a typical schematic of a LIB, highlighting the key elements and ion/electron flow paths during operation.

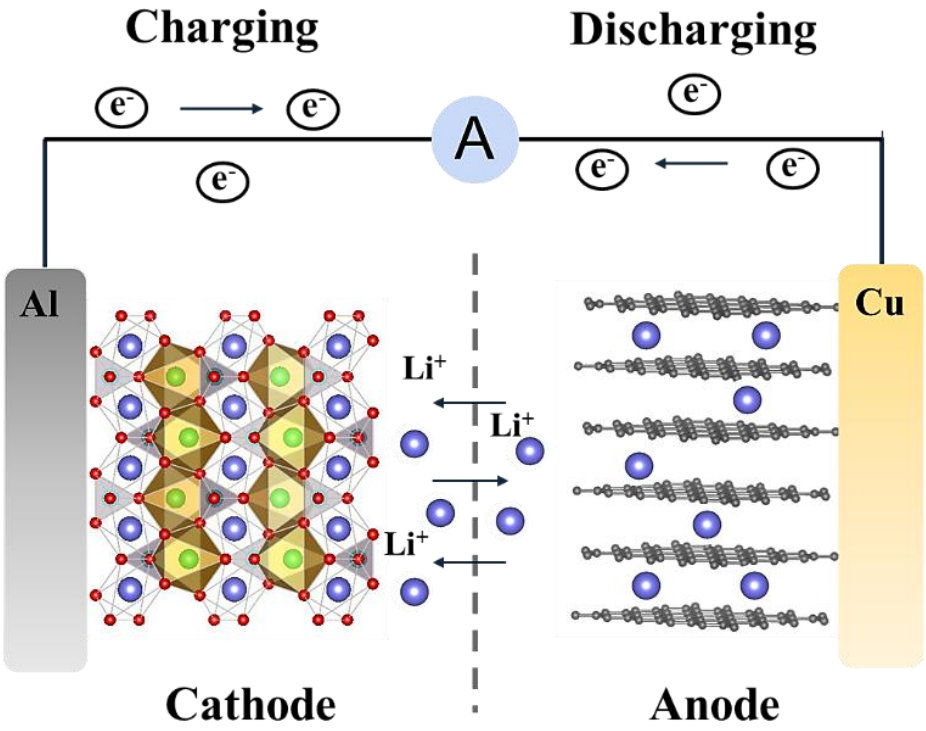

Fig. 2. Schematic representation of LIB.

1.3. Limitations of current anode materials in LIBs

Graphite, with a theoretical capacity of 372 mAh/g, remains the most widely used anode material in modern LIBs. While it has proven to be a reliable choice, graphite suffers from several limitations, especially in the context of the growing demand for high-performance batteries in applications such as EVs, energy storage for grid applications, etc. These limitations include its moderate energy density, which restricts driving range; slow Li-ion diffusion kinetics, which impede fast charging; supply chain risks, given that China controls approximately 85% of global battery-grade graphite production; and environmental concerns linked to graphite mining and synthetic production.[11] Furthermore, graphite anodes are nearing their theoretical performance ceiling, making it increasingly difficult to meet future energy

density targets that exceed 350 Wh/kg at the cell level.[12] To address these challenges, researchers are actively exploring alternative anode materials that offer higher capacities and better performance. Other carbon-based materials have also been extensively studied. For example, graphene enhances the theoretical electrode capacity to 540 mAh/g, and improves the capability rate due to reduced dimensionality, resulting in faster diffusion of Li-ions. In Li-intercalated graphene, the theoretical capacity is increased up to 1040 mAh/g.[13] Transition metal oxides are another group of materials used as negative electrodes, and their primary principle of operation relies on the metal oxidation state change at low potentials. The most common example is lithium titanate (LTO) spinel, which exhibits safety characteristics, a long lifetime, and negligible volume expansion during charging. Despite the above-mentioned advantages, LTO has a low theoretical capacity (175 mAh/g), a higher potential of 1.55 V (versus Li), and a price. Thus, LTO is a suitable material given battery exploitation safety.[14,15,16] An ideal replacement should possess low density and molecular weight to facilitate multi-electron transfer reactions, while also maintaining excellent capacity retention over many charge-discharge cycles. Silicon (Si), for instance, is attracting a lot of interest due to its extremely high theoretical capacity (~3579 mAh/g). Si can store significantly more Li than graphite, offering the potential to improve energy density drastically.[17] However, it suffers from severe volume expansion up to 300% during lithiation, which leads to electrode cracking, unstable SEI formation, and rapid capacity fading.[18] To mitigate these issues, graphite-silicon (G-Si) composite anodes have been developed, aiming to combine the structural stability of graphite with the high capacity of silicon. Despite this progress, practical challenges remain. Under commercial operating conditions (e.g., areal capacities > 3 mAh/cm^2 and volumetric capacities > 500 mAh/cm^3), it is still difficult to incorporate more than 10 wt% of silicon into graphite electrodes due to the mechanical stresses from silicon's volume changes. Moreover, Si exhibits weak Li-ion conductivity (chemical diffusion coefficient of Li in Si is 10^{-13} cm^{2}s^{-1}), which is also a significant drawback for its use as an anode material in LIBs. Other materials such as tin (Sn), germanium (Ge), and transition metal oxides have shown promise, but face similar issues with volume instability, high cost, or poor rate capability. The pros and cons of significant anode materials are given in Table 1.

Table 1. An overview of the pros and cons linked with significant anode materials.[19]

Materials	Pros	Cons
Silicon	Enhanced capability range (3579 mAh/g), isolated, inexpensive	Sudden alteration in volume surge (300 %)
Transition metal oxides	Enormous specific capacity (600–1000 mAh/g) adequate level of stability	Low Columbic efficiency, maximum achievable hysteresis
Alloys	Excellent energy storage capability (400–2300 mAh/g), adequate level of security, impressive durability over multiple cycles, columbic efficiency achieved to the satisfaction	Reduced conductivity, significant volume fluctuation, decrease in capacity
Carbon	Enhanced safety, excellent structural integrity, superior conductivity characteristics, prolonged lifespan	Limitations of capacity, irregularities in safety, extended lifespan, and reduction in discharge rate

Another critical factor influencing the performance of LIBs is the electrode/electrolyte interface, which plays a dual role: enabling energy storage and serving as the site where many degradation processes are initiated. One of the most important and widely studied interfacial phenomena is the formation of the SEI on the negative electrode, as illustrated in Fig. 3.[19,20] The SEI is a passivation layer that forms primarily during the initial charge-discharge cycles through the reductive decomposition of electrolyte components. An ideal SEI layer is selectively permeable, allowing Li-ion transport while blocking the passage of electrons and electrolyte solvents. This prevents continuous electrolyte decomposition and enables reversible Li-ion diffusion, thereby contributing to cycling stability and the extended electrochemical window of organic electrolytes. However, the SEI is not entirely stable. Although it initially forms during the early cycles, it continues to evolve throughout the battery's lifespan, often thickening due to ongoing parasitic reactions. This continual growth leads to several problems,

including increased impedance, loss of active Li, reduced ionic conductivity, and eventual capacity fading. Additionally, the heterogeneous and mechanically fragile nature of the SEI can lead to cracking and reforming during cycling, further accelerating degradation. Therefore, understanding and controlling SEI properties is also essential for improving battery longevity, safety, and overall performance.[20,21]

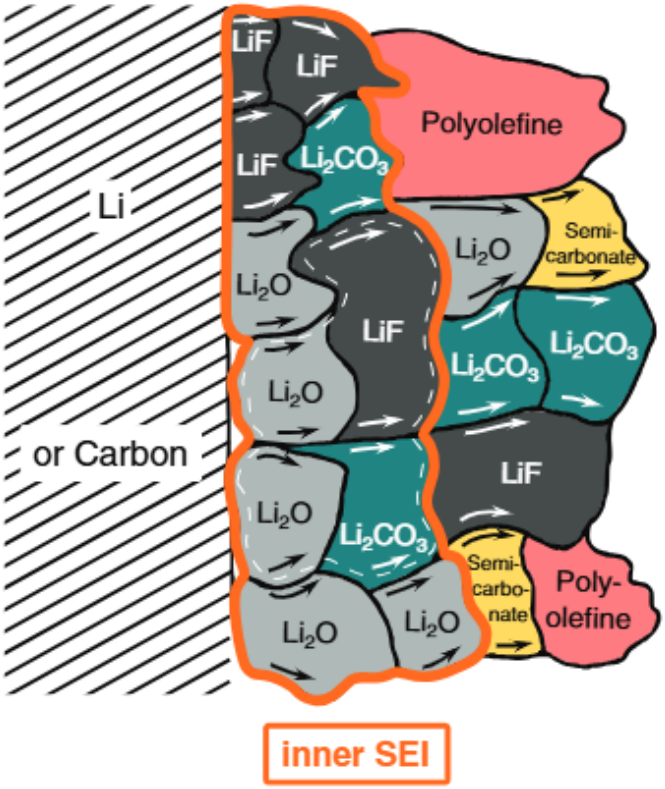

Fig. 3. Mosaic model of the SEI according to Peled *et al.*[20,21]

1.4. Next-generation Li-metal batteries

Among emerging battery technologies, rechargeable systems beyond conventional LIBs, such as Li/nickel-rich transition metal oxide, Li-sulfur (Li-S), Li-solid state batteries (SSBs), and Li-oxygen (Li-O_2) batteries, offer significantly higher energy densities of approximately 440, 650, and 950 Wh kg^{-1}, respectively.[22] These advanced chemistries are being actively explored as next-generation energy storage solutions. A key component common to all these high-energy systems is the use of Li-metal as the anode. Compared to traditional anode materials used in LIBs (discussed in the previous section), Li-metal stands out due to its exceptionally high theoretical capacity (3861 mAh/g), the lowest redox potential (-3.04 V vs. the standard hydrogen electrode), excellent electronic and ionic conductivity, and competitive cost per unit

of energy stored. Furthermore, Li-metal is uniquely suited for pairing with high-energy sulfur and oxygen cathodes, as it serves as an intrinsic source of Li ions, an essential requirement in Li-S and Li-O_2 systems.[23]

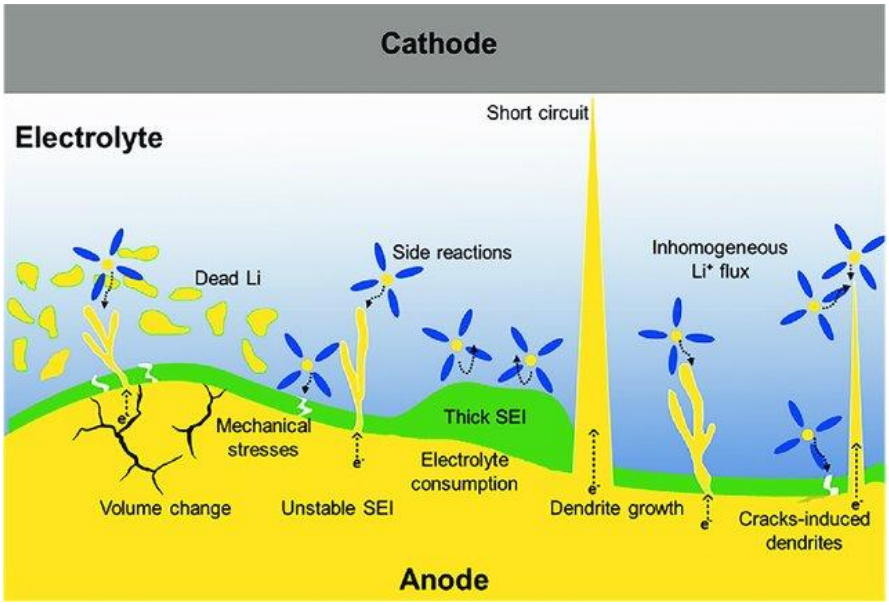

Fig. 4. Schematic illustration of the failure mechanisms that occur in the Li-metal anode.[24]

These advantages make Li-metal batteries (LMBs) highly attractive candidates for next-generation energy storage applications, particularly in fields such as electric transportation and grid-level storage. However, Li with traditional liquid electrolytes faces significant challenges that hinder their long-term stability and the safety of the LMA-based battery system (Fig. 4).[23] A key issue is the uncontrolled growth of Li dendrites during repeated charge-discharge cycles, which can pierce the separator, cause internal short circuits, and lead to thermal runaway. Additionally, the extreme volume changes that occur during Li plating and stripping stress the electrode structure and compromise performance. Due to Li's high reactivity, the electrolyte forms a SEI layer on the anode surface, which initially helps to protect the Li and limits further electrolyte decomposition. However, continuous dendritic growth and volume fluctuation damage the SEI, leading to cracks. These cracks expose fresh Li, promoting further dendrite growth via the tip effect and accelerating SEI degradation. Over time, uneven Li deposition results in the formation of "dead Li" that becomes electrochemically inactive, causing rapid capacity fade. In severe cases, dendrites can breach the separator and contact the cathode, triggering catastrophic failure.[24, 25] To address these issues, recent advancements focus on four main strategies (Fig. 5)[26] for stabilizing LMAs: (i) surface coatings that enhance SEI stability

and suppress dendrite formation,[27,28] (ii) 3D porous current collectors that accommodate volume changes and ensure uniform Li distribution,[29,30] (iii) advanced liquid electrolytes engineered to form stable SEI layers,[31,32] and (iv) solid-state electrolytes (SSEs) that offer mechanical robustness and dendrite suppression.[33,34] Together, these approaches aim to enable safer and longer-lasting LMB.[35] Among these, the application of *ex-situ* artificial solid electrolyte interface (ASEI) on the Li-metal surface has emerged as one of the most effective

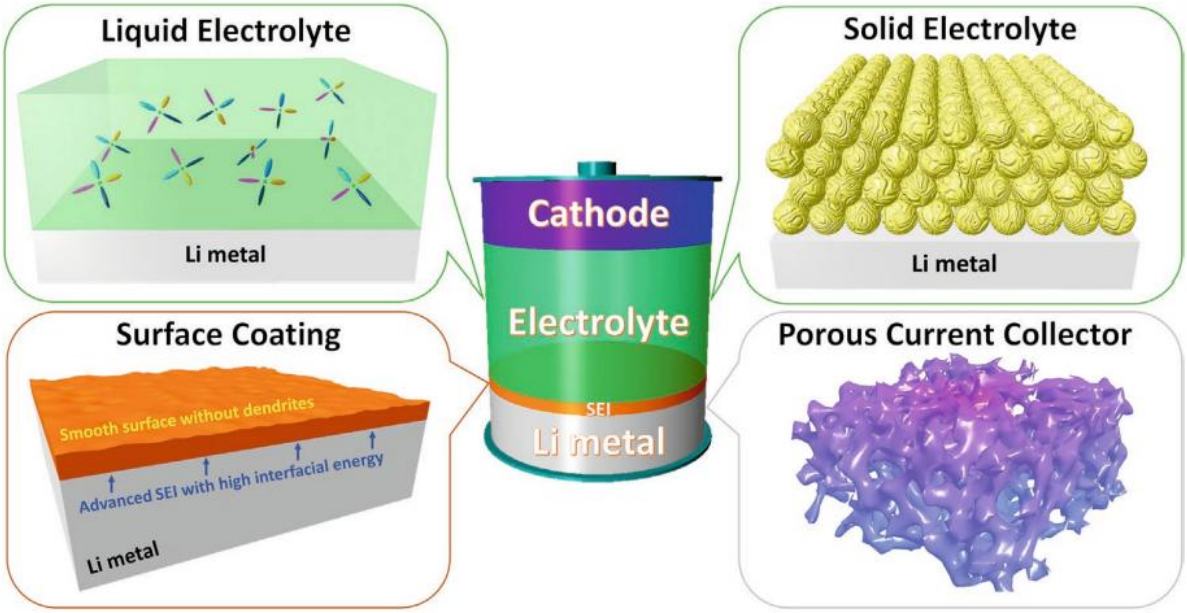

Fig. 5. The schematic illustration of strategies for Li-metal anode in stable and safe LMBs.[27]

approaches. These ASEI help in regulating Li-ion distribution and enhance the stability of the electrode/electrolyte interface, thereby mitigating dendrite growth and improving long-term battery performance. So far, a variety of coating materials, including inorganics,[36] polymers,[37] and hybrids [38] have been applied. The ideal ASEI should exhibit high Li-ion conductivity, excellent electrolyte stability, electronic insulation, and mechanical flexibility to accommodate the volumetric changes of the LMA during cycling.[39] However, achieving an optimal balance between structural stability and high ion conductivity remains a critical challenge, since most of the existing coatings either introduce ASEI materials that are structurally stable or have a high Li-ion conductivity.[36] Hence, there is a constant search for new ASEI materials.

1.5. Metal halide perovskites and their fundamental properties

One of the emerging groups of active materials in the field of energy storage is inorganic and organic-inorganic metal halide perovskites (MHPs) with the general formula ABX_3, where 'A' stands for a small organic or inorganic cation, 'B' is a divalent metal ion, and 'X' is a halogen

anion. MHPs are a specific family of crystalline materials featuring a soft crystal lattice with excellent structural and compositional tunability.[40] These perovskites are characterized by a soft crystal lattice and exceptional structural and compositional tunability, which make them highly attractive for a range of applications. Over the past decade, MHP materials and their wide-ranging applications have experienced remarkable growth. Their exceptional optoelectronic properties, combined with the ability to control photogenerated ions and electronic charges simultaneously, make them an outstanding platform for numerous technological uses. MHPs first gained prominence as the foundation for a new era in photovoltaics, with perovskite solar cells (PSCs) rapidly transforming the renewable energy landscape.[41,42,43,44] The breakthrough for MHPs in photovoltaics began with their application in dye-sensitized architectures in 2009, achieving a power conversion efficiency (PCE) of ~3.8%.[45] Since then, advances in material engineering, especially compositional tuning at the A-site and X-site ions, have driven PCEs above 26%.[46,47] Due to their tunable optical and electronic properties, combined with rapid progress in their compositional engineering, they have positioned them as promising candidates for a wide range of optoelectronic applications, such as light-emitting diodes (LEDs),[48] photodetectors, and photocatalysts.[49,50,51] Not surprisingly, MHPs have also begun to show promise in LIBs. Their tunable bandgap (ranging from 400 to 800 nm), high charge carrier mobility (1–10 $cm^2\ V^{-1}\ s^{-1}$), long diffusion lengths (~1 μm), cost-effective processing, and availability of precursors make them attractive for energy storage applications.

1.5.1. Compositional engineering and phase transitions

As mentioned previously, the typical three-dimensional (3D) MHPs share the basic chemical formula ABX_3, where 'A' is a monovalent cation (such as Cs^+, $CH_3NH_3^+$ or MA, $HC(NH_2)_2^+$ or FA etc.), 'B' is a divalent transition metal cation (generally Sn^+, Pb^+, etc.), and 'X' is a monovalent halide anion (Cl^-, Br^-, I^-), forming corner-sharing $[BX_6]^{4-}$ octahedra cavities containing the 'A' cations as shown in Fig. 6a.[48,52] This family of materials can be further divided into two groups according to the nature of the A-site cation: all-inorganic halide perovskites incorporating inorganic cations and organic-inorganic halide perovskites (or so-called hybrid halide perovskites) incorporating charge-compensating amine cation. For achieving structural stability in the 3D network, the ionic radii of the cations and anions should follow the empirically derived Goldschmidt tolerance factor (t) and octahedral factor (μ).[53] Both tolerance and octahedral factor predict the perovskite crystal stability with variations in

metal cations and halide anions. The tolerance factor can be described by the following equation:

$$t = \frac{r_A + r_X}{\sqrt{2}(r_B + r_X)} \quad (1)$$

where r_A and r_X are the ionic radii of the A-site cation and X-site halide anion, and r_B is the Shannon ionic radius of the B-site cation, respectively, in the ABX_3 perovskite halide compounds. The octahedral factor can be expressed by the following equation.[54] :

$$\mu = \frac{r_B}{r_X} \quad (2)$$

A stable 3D perovskite structure at room temperature and ambient pressure is generally achieved when the *t* and μ fall within the ranges $0.813 < t < 1.107$ and $0.442 < \mu < 0.895$, respectively.[55] Moreover, a highly symmetric cubic structure characteristic of MHPs is typically stabilized only within a narrower tolerance factor range of $0.9 < t < 1$. Deviation from

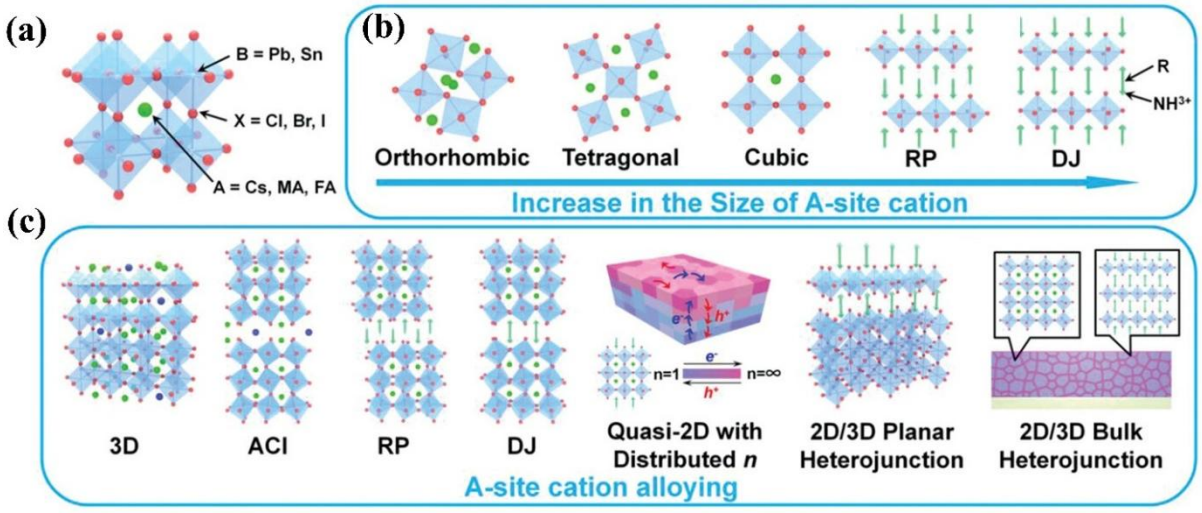

Fig. 6. (a) Schematic illustration of the typical ABX_3 structure of MHPs. (b) Formability of 3D MHPs as a function of the size of the A-site cation. (c) ABX_3 structure evolution with A-site cation alloying.[52]

this range results in distortion of the cubic lattice, leading to lower symmetry structures. The size of the A-site cation plays a crucial role in dictating the structural stability of perovskites. Since the A-site cations reside within the $[BX_6]^{4-}$ framework, a cation that is lower than the ideal size causes tilting of the BX_6 octahedra. This tilting induces structural distortion, giving rise to lower symmetry phases such as tetragonal or orthorhombic forms. Moreover, if the size of the A-site cation is larger than the ideal size, two-dimensional (2D) structures like

Ruddlesden-Popper (RP) phase and Dion-Jacobson (DJ) phase will be formed (Fig. 6b).[56] Moreover, when A-site cations are alloyed by small or oversized cations, various crystal structures will be formed, including one-dimensional (1D) structures (Fig. 6c).[57,58]

1.5.2. Factors guiding chemical and physical properties of MHPs

a) Compositional Factors

The physicochemical properties of MHP materials originate from their unique inorganic lattice and the intricate interactions between the inorganic framework and organic components.[59] Consequently, structural modification of MHPs achieved by introducing specific cations or anions at various sites within the parent ABX_3 perovskite structure has become a widely adopted strategy to tailor their fundamental physical and chemical characteristics. Initially, the prevailing belief was that the role of the A-site cation was to maintain the overall charge neutrality. However, more recent studies have demonstrated that the versatility of the A-site cation indirectly affects the structure-property-performance.[60] In contrast, the electronic properties of MHPs are more directly governed by the composition of the B- and X-site ions.[61,62] For example, in $MPbX_3$, the deeper region of valence band minima (VBM) consists mainly of *p* orbitals of the 'X' ions and a small contribution from the overlapping of *s* orbitals of the 'B' ions. The edge of VBM consists of anti-bonding states of the *s* orbitals of 'B' ions and *p* orbitals of 'X' site ions. Therefore, when different halides are used with different electronegativity, the position of the VBM edge changes, hence the bandgap changes. On the other hand, the conduction band minima (CBM) are mainly determined by the antibonding overlap between the *p* orbitals of 'B' site ions and a small contribution of the *p* orbitals of 'X' site ions.[63] A detailed discussion on the influence of A-, B-, and X-site doping on the physicochemical properties of MHPs is provided in the subsequent sections.

'A' cation: The A-site cation in MHPs plays an indirect but important role in influencing their electronic properties. By altering the lattice volume and introducing structural distortions to the ideal cubic ABX_3 framework, the A-site cation leads to the formation of various non-cubic phases. Although these structural changes have only a limited impact on the electronic band structure, they are critical for understanding and optimizing the optoelectronic performance of MHPs.[64,60] A highly symmetric cubic structure tends to exhibit reduced band gaps due to improved packing symmetry. However, as the A-site cation size increases beyond this optimal range ($t > 1$), the resulting lattice expansion and structural deformation lead to bandgap

widening.[65] Specifically, structural deformation primarily affects ionization energy (IE), while volumetric expansion has a more pronounced influence on electron affinity (EA). The ionic nature of MHPs renders them susceptible to ion migration, particularly under external electric fields or illumination. Such migration can create crystal defects that degrade device performance through current–voltage hysteresis, phase segregation, and chemical corrosion. A-site engineering has emerged as an effective strategy to mitigate these challenges. Additionally, A-site doping can stabilize desirable perovskite phases and address long-standing issues in long-term operational stability, a key barrier to commercialization.[66]

'B' cation: In MHPs, the B-site is typically occupied by divalent metal cations such as Ge^{2+}, Sn^{2+}, and Pb^{2+}, which possess fully or partially filled 4s, 5s, and 6s valence orbitals, respectively. These ns^2 lone-pair electrons contribute significantly to the upper region of the VB, playing a crucial role in determining the VBM and, consequently, the electronic structure of MHPs. The stereochemical activity of these lone pairs strongly influences the electronic properties, and an increase in atomic radius (from Ge to Sn to Pb) has been shown to correspond with a widening of the bandgap. This trend is attributed to the changes in the energy level and activity of the lone-pair states. In 2D MHPs, reduced structural dimensionality allows for a broader range of off-center displacements of the B-site metal cation. As a result, the stereochemical activity of the ns^2 lone-pair electrons is more pronounced in 2D Ge-, Sn-, and Pb-based perovskites.[62] Goesten and Hoffmann [61] conducted an in-depth analysis of the impact of substituting Pb^{2+} with Sn^{2+} or Ge^{2+}, along with halide variation, on the bandgap of $CsPbBr_3$. Complementarily, Nishat *et al*.[67] proposed that a reduction in the B-site cation's atomic radius increases the nuclear electrostatic attraction on valence electrons, thereby raising the IE and EA. This stronger binding of valence electrons can lower both the bandgap and bonding energy. Thus, a decrease in atomic radius may result in narrower bandgaps, in contrast to trends driven by lone-pair effects.

'X' anion: The composition of the halide (X-site) in MHPs plays a pivotal role in determining the feasibility of perovskite lattice formation and enables fine-tuning of key physicochemical properties, including bandgap energy and photoluminescence characteristics. For instance, $APbCl_3$ perovskites exhibit a wide bandgap of approximately 3.0 eV, resulting in white coloration and luminescence in the 400-450 nm range. In comparison, $APbBr_3$ analogues possess a narrower bandgap (~2.2 eV) with emission centered around 500–550 nm, whereas $APbI_3$ counterparts exhibit the narrowest bandgap (~1.5 eV), corresponding to emission in the

near-infrared range of 800-850 nm. Mixed-halide compositions exhibit intermediate band gaps and emission profiles, which are approximately proportional to their halide content. This compositional flexibility enables the rational design of perovskite materials tailored for specific optoelectronic applications. [68] Substitution at the halide site also significantly impacts the electronic structure, particularly the IE and EA of the material. This can be theoretically analysed by examining the trend in halide anion properties, such as increasing atomic radius and lone-pair electron energy levels along the series Cl^- ($3s^2$) → Br^- ($4s^2$) → I^- ($5s^2$). The CBM is primarily governed by the B-site cation p-orbital energy levels, which tend to shift downward as the atomic radius of the halide increases. This trend can be attributed to the quantum confinement effect: as the B-X bond length increases from Cl to I, the electron localization on the B-site is reduced, leading to a lowering of the CBM energy. Simultaneously, the VBM shifts upward across the same series, primarily due to the decreasing electronegativity of the halide ions (Cl > Br > I). These combined effects of halide substitution enable precise control over the electronic band structure of ABX_3 perovskites, further enhancing their suitability for a wide range of optoelectronic applications.[69]

b) Phase transition and external factors

MHPs, owing to their inherently ionic lattice structures, exhibit significant ion migration, dynamic lattice behavior, and a pronounced sensitivity to external stimuli such as temperature, pressure, and redox conditions. These characteristics render both hybrid organic–inorganic and all-inorganic MHPs highly responsive to their environment and often undergo structural phase transitions. Polymorphism is one of the most notable consequences of this structural flexibility, which profoundly influences the electronic structure.[70,71,72,73] In general, 3D MHPs adopt a high-symmetry cubic structure at elevated temperatures and undergo sequential phase transitions from cubic to tetragonal to orthorhombic upon cooling. Cs-based halide perovskites offer higher structural stability than their organic analogues; they are also susceptible to structural phase transitions under the influence of external factors. For example, $CsPbI_3$ perovskite exhibits four polymorphs with temperature-induced transitions (Fig. 7a). Remarkably, the black phase $CsPbI_3$ perovskite exhibits poor structural stability at room temperature and spontaneously transforms to the yellow, photoinactive, non-perovskite phase.[74] Moreover, as shown in Fig. 7b, these distinct phases exhibit markedly different optoelectronic characteristics, including variations in band gap, photoluminescence quantum

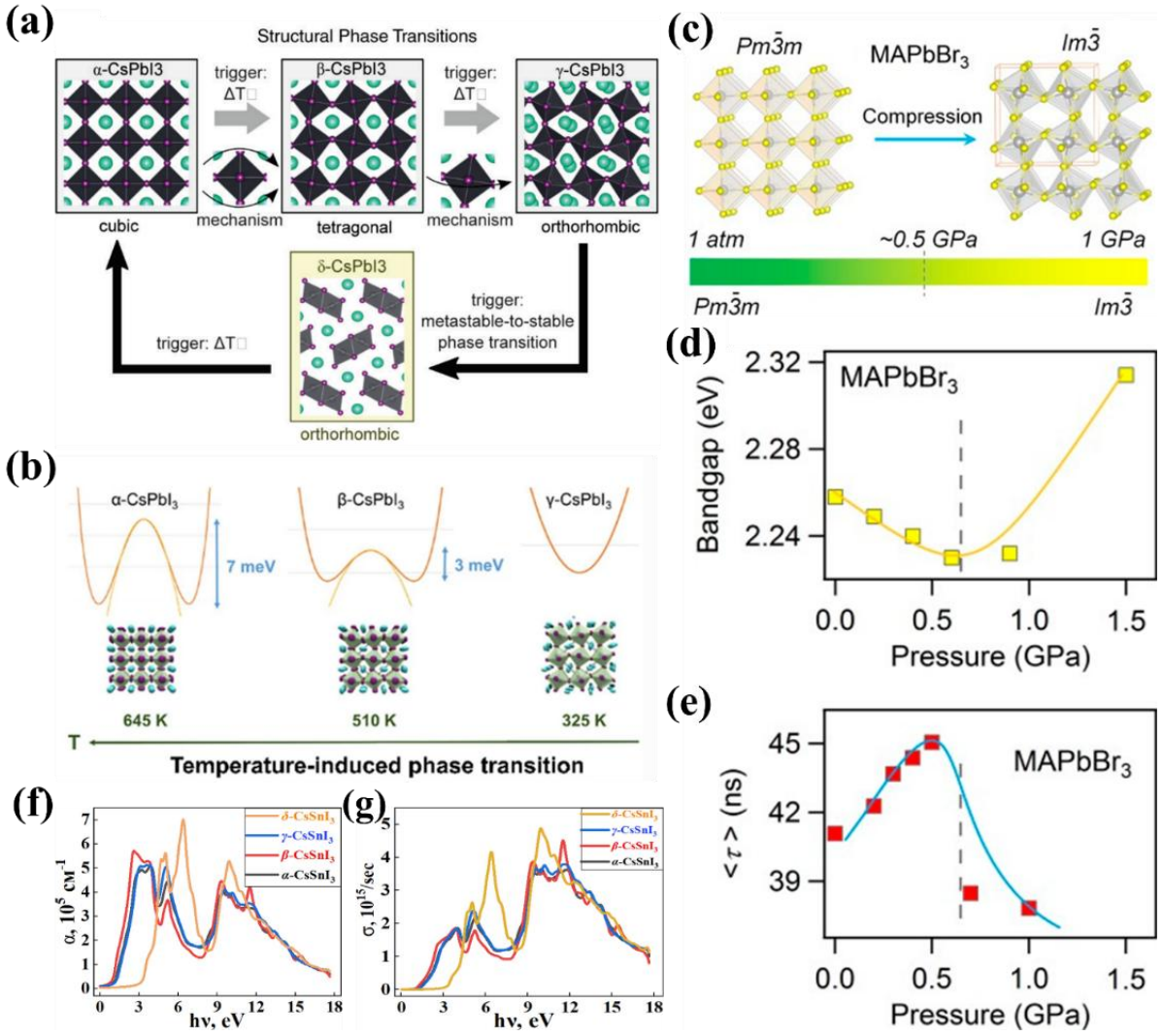

Fig. 7. (a) Variable-temperature phase transitions among the $CsPbI_3$ polytypes,[74] (b) Illustration of the variation of the bandgap with the phase transition of the $CsPbI_3$ crystal,[75] (c) Pb-Br inorganic frameworks of $MAPbBr_3$ for low-pressure $Pm\bar{3}m$ and high pressure $Im\bar{3}$ Phases. The high-pressure phase in $MAPbBr_3$ exhibits the characteristic elongation of the lead-halide octahedral, together with smaller lead–halide–lead bond angles. (d and e) Demonstration of the band-gap narrowing and carrier-lifetime prolongation in $MAPbBr_3$ at mild pressures, respectively,[76] (f) and (g) Calculated absorption coefficient and optical conductivity of α-, β-, γ-, and δ-phases of $CsSnI_3$ as a function of photon energy in the X direction.[77]

yield, charge carrier mobility, and carrier lifetime.[75] Similarly, Kong et. al.[76] investigated high-pressure-induced phase transitions in $MAPbBr_3$. They revealed through their research that $MAPbBr_3$ experiences a cubic-cubic phase transition from $Pm\bar{3}m$ to $Im\bar{3}$ at approximately 0.5 GPa, which is attributed to the distortion of the $PbBr_3$ polyhedron (Fig. 7c). They indicated that the narrowest band gap, around 2.230 eV (Fig. 7d), along with the longest carrier lifetime (Fig.7e), is also observed near the phase-transition pressure of approximately 0.5-0.6 GPa. Their results have clearly highlighted the effectiveness of using pressure to modulate crystal

structures, which results in a favorable enhancement of material properties. Additionally, the effect of phase changes on electronic and optical properties of three perovskite phases of $CsSnI_3$, as well as their non-perovskite structure, was studied by DD Nematov et.al [77]. They showed that the absorption (Fig. 7f) and photoconductivity (Fig. 7g) of the $CsSnI_3$ compound are enhanced in the infrared (IR) and visible light ranges as it transitions from the low-temperature phase to the high-temperature phase, while the stable yellow phase of $CsSnI_3$, known as the δ-phase, only absorbs short-wavelength light.

(c) Dimensionality

By leveraging the diverse structures and compositions of MHPs, the dimensionality of MHPs can be precisely adjusted, ranging from 3D to various low-dimensional forms such as quasi-2D, 2D, 1D, and zero-dimensional (0D) configurations. There are two types of low-dimensionalities, one is the “structure-level” and “material-level”.[78] The "structure-level" low-dimensional aspect highlights the different morphologies and typically refers to nanostructures like nanosheets, nanowires, and nanocrystals (NCs) (Fig. 8a). In contrast, the "material-level" low-dimensional aspect of perovskite focuses on the fundamental structure where the $[BX_6]^{4-}$ octahedra are interspersed with large dielectric spacer molecules, resulting in a bulk formation of atom-level 0D clusters, 1D quantum wires, or 2D quantum wells (QWs) (Fig. 8b). The crystalline perovskite nanostructures with reduced dimensionality show distinctive optoelectronic properties with quantum-confined effect compared with their bulk counterparts (Fig. 8c).[79] Due to this greater than that of their bulk forms. This is accompanied by a variation in the geometric size of perovskite nanostructures, which further alters the bandgap. As depicted in Fig. 8d, the photoluminescence emission wavelengths were systematically adjusted through the gradual decrease in the size of $FAPbI_3$ NCs.[80] Consequently, the calculated bandgap energy rose from 1.5 eV in bulk material to more than 1.7 eV for perovskite NCs with an edge length of approximately 8 nm (Fig. 8e). In addition to the hybrid perovskite NCs, inorganic perovskite NCs and quantum dots (QDs) also exhibit bandgap energies dependent on size or diameter, such as $CsPbI_3$ and $CsPbBr_3$.[81,82] This size effect can also be anticipated in 1D perovskite nanowires (NWs), where the diameter determines the bandgap energy and emission wavelength independent of the length. Furthermore, in 2D perovskites, the octahedral layers are situated between the organic spacers. These organic compounds provide extra functionality, such as a tunable quantum well structure that can be modified by varying the length and type of the organic chain. Fig. 8f presents the photoluminescence spectra of 2D

$BA_2(MA)_{n-1}Pb_nI_{3n+1}$ perovskites, which depend on the number of layers, demonstrating a significant wavelength tuning range from approximately 520 nm to 650 nm (~130 nm difference, corresponding to a shift of about ~0.47 eV).[83] A comparable layer-dependent pattern was observed in 2D perovskites composed of three cations that include both organic (PEA, MA) and inorganic (Cs) components (Fig. 8g), revealing a consistent decrease in bandgap energy as the number of layers increases, with an energy difference of up to ~0.6 eV between single unit-cell and five-unit-cell crystals.[84]

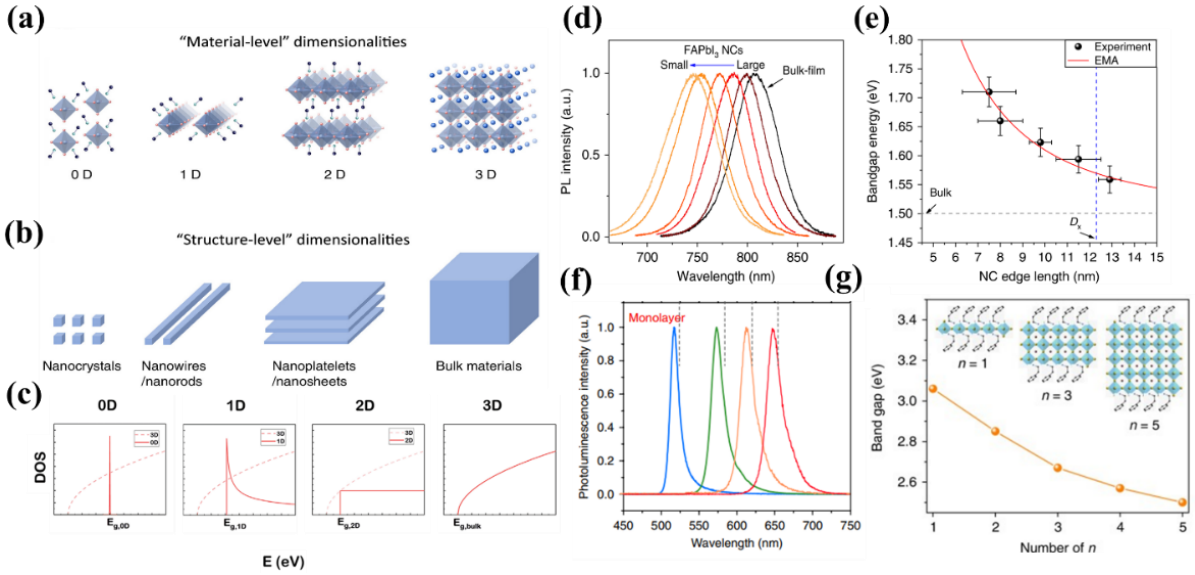

Fig. 8. (a) Schematic representation of "material-level" and (b) "structure-level" 3D bulk, 2D, 1D, and 0D perovskite materials,[79] and (c) is the corresponding density of states versus the energy Eg.[79] (d) Photoluminescence (PL) spectra of $FAPbI_3$ nano-crystals (NCs) with different sizes. (e) Bandgap energies versus the edge length of $FAPbI_3$ NCs.[80] (f) PL of exfoliated monolayers for 2D layered $BA_2(MA)_{n-1}PbnI_{3n+1}$ Ruddlesden-Popper perovskites of n=1 to 4 homologues[83] (g) The bandgap of $PEA_2A_{1.5}Pb_{2.5}Br_{8.5}$ (A = MA and Cs) perovskites with different numbers of layers.[84]

1.5.3. Mechanism of Li-Interaction with MHPs

The LIB utilizing MHPs ($MAPbBr_3$ and $MAPbI_3$) as an anode was first reported in 2015 by Xia *et al*.[85] The authors described good electrochemical performance for $MAPbBr_3$ with a first discharge capacity of 331.8 mAh/g at a current density of 200 mA/g, which is six times the maximum theoretical capacity (55.96 mAh/g) if it is assumed that one Li-ion could intercalate per formula unit. This significant difference in electrochemical performance suggests a conversion reaction or another effect that is at play, since six Li-ions per formula unit would otherwise be required.[86] Despite these impressive performance metrics, the key mechanism by

which Li is intercalated in MHPs remains unknown. Initially, two mechanisms were proposed for Li uptake in perovskites:

1. **Intercalation mechanism:** Vicente *et al*.[87] suggested that there is topotactic Li-ion insertion into perovskites without severe structural alterations, as shown in Fig. 9a. He shows through X-ray photon spectroscopy (XPS) analysis that no Li-Pb alloying reactions occur (Fig. 9b). However, it was unclear which species are reduced because of Li intercalation, given that the Pb and Br electronic structures remain mostly unchanged.
2. **Conversion mechanism:** In the same year, using electrochemical and powder X-ray diffraction (XRD) techniques, combined with DFT, Dawson *et al*.[86] proposed that both intercalation and conversion reaction occurs during the charge/discharge cycle. The authors indicated that for all three hybrid perovskites, $MAPbX_3$ (X=Cl, Br, I), the energy for conversion reactions is more favorable than the intercalation reactions.

In 2019, Vicente *et al*.[88] conducted another study to understand the Li uptake mechanism in $MAPbBr_3$ using *operando*-XRD analysis in conjunction with galvanostatic lithiation (discharge) and delithiation (charge) steps (Fig. 9c and d). The researchers identified three reaction stages (lithiated phase, conversion, and alloying) associated with varying Li-ion molar content. However, the mechanism of phase transition during the subsequent cycles was not established. In the case of all-inorganic halide perovskites, *ex-situ* XRD patterns of the $CsPbCl_3$ electrode reveal that the preferred mechanism for Li-ion storage in the initial discharge cycle is through conversion reactions rather than Li-intercalation.[89] As a result, the disputed and vague findings from the *ex-situ* characterizations obscure the understanding of the structural changes of halide perovskites throughout the lithiation and delithiation process. Recently, XH Wu et. al.[90] utilized *in-situ* XRD and electrochemical impedance spectroscopy (EIS), along with *ex-situ* characterizations to explore the intricate mechanisms of Li storage and release in $CsPbBr_3$, including the phase transition that occurs during the first three cycles. The findings indicate that at full discharge, $CsPbBr_3$ breaks down into CsBr, LiBr, Pb, and $Li_{22}Pb_5$ phases via intercalation-conversion-alloying reactions, followed by the regeneration of $CsPbBr_3$ during the charging process (Fig. 9e). However, several studies have reported different Li-ion transport mechanisms and SEI formation (shown in Table 2); the precise mechanistic pathways are still a bit of a mystery in this field. This uncertainty largely stems from the intricate structural changes that MHPs undergo during cycling, the diverse range of

perovskite compositions (such as lead-based, tin-based, and double perovskites), and the absence of systematic in situ characterization under realistic battery conditions. Therefore, this field of research requires further investigation.

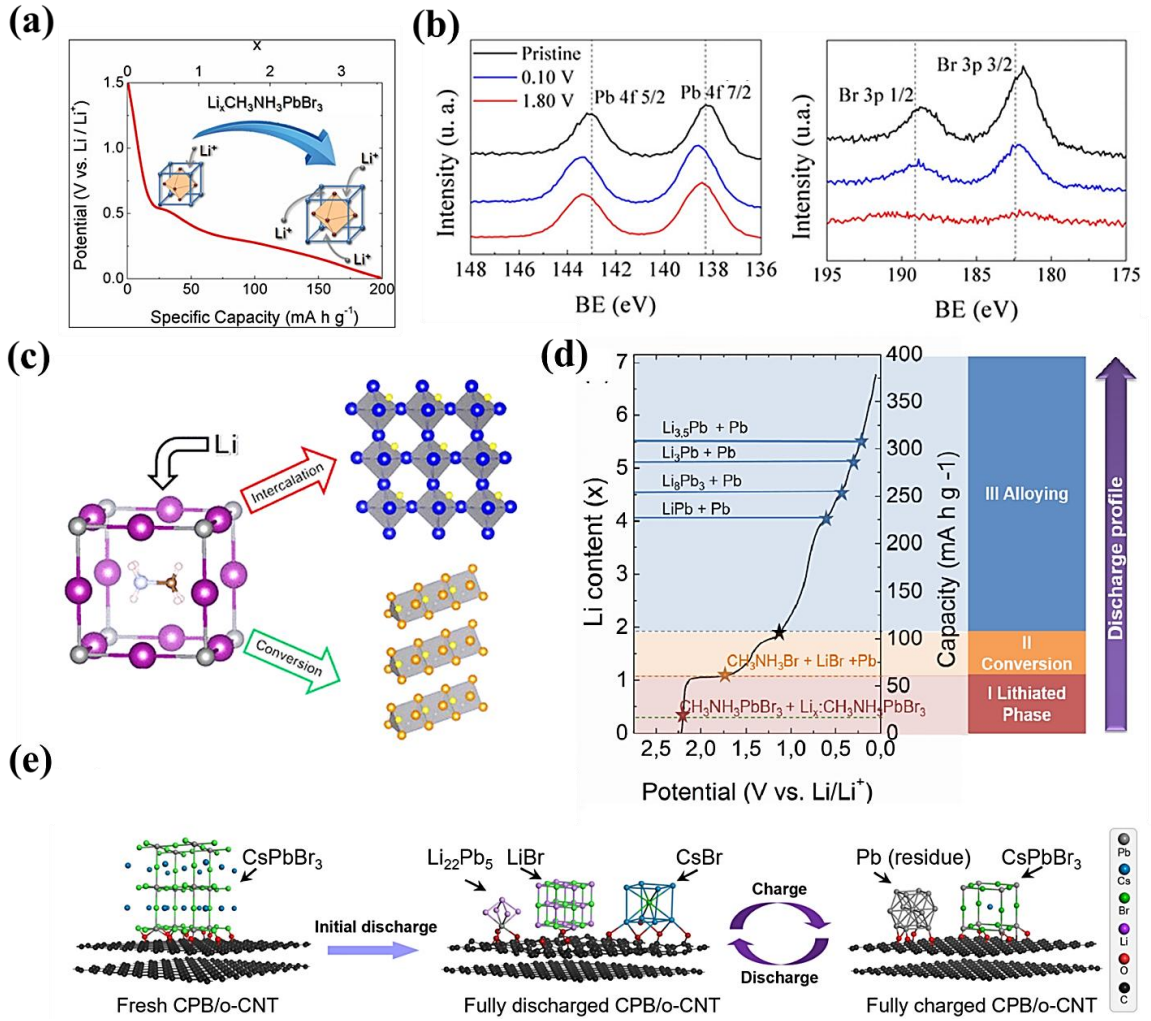

Fig. 9. (a) Crystal structure of organometal halide perovskite $MAPbBr_3$, indicating multiple Li-ion interactions. (b) Pb 4f and Br 3d core-level XPS signal of $MAPbBr_3$ anodes at different states: pristine, 0.10 V (discharge), and 1.80 V (subsequent charge),[87] (c) Schematic illustration of the conversion and intercalation mechanism occurring in organic-inorganic MHPs, (d) The recorded discharge profile, where each stage is highlighted in a different color: First, the pure material (red), and lithiated phase (red); second, the conversion stage (orange), and third, the alloying stage (blue),[88,89] (e) Schematic illustration of the structural evolution process of CPB/o-CNT composite upon cycling.[90]

Table 2. Li-transport mechanisms, SEI composition & evolution of different MHPs.

Perovskite material	Electrolyte	Li storage mechanism/ Proposed reaction	Initial SEI characteristics	SEI evolution	Ref
$CsPbCl_3$	1 M $LiBF_4$ in PVDF-HFP + $BMIMBF_4$ (1:3 w/w)	Conversion → 2Li + $CsPbCl_3$ → CsCl + 2LiCl + Pb; subsequent Li–Pb alloying (Li_xPb_y) during deeper discharge	Likely contains LiCl, CsCl, Li-Pb alloys, solid electrolyte matrix	*Ex-situ* XRD after 10 cycles: loss of $CsPbCl_3$ peaks; intensification of Pb + Li_xPb_y → conversion + alloying dominant	89
$CsPbBr_3$	1M $LiPF_6$ in EC:DEC: DMC (1:1:1) with 5% FEC	1. Intercalation→ conversion→ alloying $CsPbBr_3$ + 6.4 Li^+ + 6.4 e^- → CsBr + $Li_{22}Pb_5$+ 2LiBr (discharged) 2. Partial reformation of the $CsPbB_3$ on charge xCsBr + $Li_{22}Pb_5$ + 2xLiBr → $x$$CsPbBr_3$ + (22+2x)Li^+ + (22+2x)e^- + (5-x)Pb (residue) (charged)	Likely contains FEC-derived FEC-rich SEI, LiBr, CsBr, LiPb alloys, and Pb residue.	*Ex-situ* XRD and XPS after long-term cycling; Reduced content of $CsPbBr_3$ perovskite; pulverization → CsBr/Pb nanoparticles on CNTs	90
$CsPbI_3$	1M $LiPF_6$ in EC/ DMC (1:1)	Intercalation forming Li_xCsPbI_3 at higher V; deeper discharge yields conversion and Li-Pb alloying	Probably contains LiF, Li_xPF_y, $Li_xPF_yO_z$ from salt decomposition; Li-alkoxy species (CH_3OLi, $(C_2OLi)_2$) from EC/DMC reduction; possible Cs/Li iodides	SEI forms in the first cycle and stabilizes; Post-100-cycle XRD/SEM: δ-$CsPbI_3$ peaks retained.	91
$MAPbBr_3$ / $MAPbI_3$/MA $PbIBr_2$	1.0 M $LiPF_6$ in EC/ DEC (1:1) vol ratio)	Li intercalation followed by Pb(II) → Pb(0) reduction and conversion to LiX + Pb + Li_xPb alloys (LiPb, $Li_{2.6}Pb$, $Li_{4.4}Pb$, etc.), plus SEI formation (LiF, Li_2CO_3, organics); below ~0.6 V, alloying–dealloying dominates	LiF, Li_2CO_3, alkoxides; Pb/LixPb in SEI; possible LiI residues	Pb, Li-Pb alloys, and halide products may remain embedded in SEI after 10 cycles	92
$MANiCl_3$	1.0 M $LiPF_6$ in EC/ DMC (1:1) vol ratio)	Intercalation into $MANiCl_3$ lattice → Conversion to MACl + LiCl + metallic Ni → Alloying to Li–Ni alloys (Li_xNi_y) + MACl	SEI containing LiF, LiCl, and organic carbonate species	May form thicker SEI after cycling; increased R_{SEI}.	93

1.5.4. MHP-based anodes

The first use of 3D MHPs as anode materials was proposed by Xia *et al.* [85] in 2015, where hydrothermally synthesized $MAPbBr_3$ and $MAPbI_3$ microcrystals displayed a first discharge capacity of nearly 330 mAh/g and 50 mAh/g at 200 mA/g current density (Fig. 10a). Moreover, the cycle stability of $MAPbBr_3$ shows prominent improvement as compared to $MAPbI_3$ (Fig. 10b). While the specific reasons for the enhanced performance of $MAPbBr_3$-based batteries

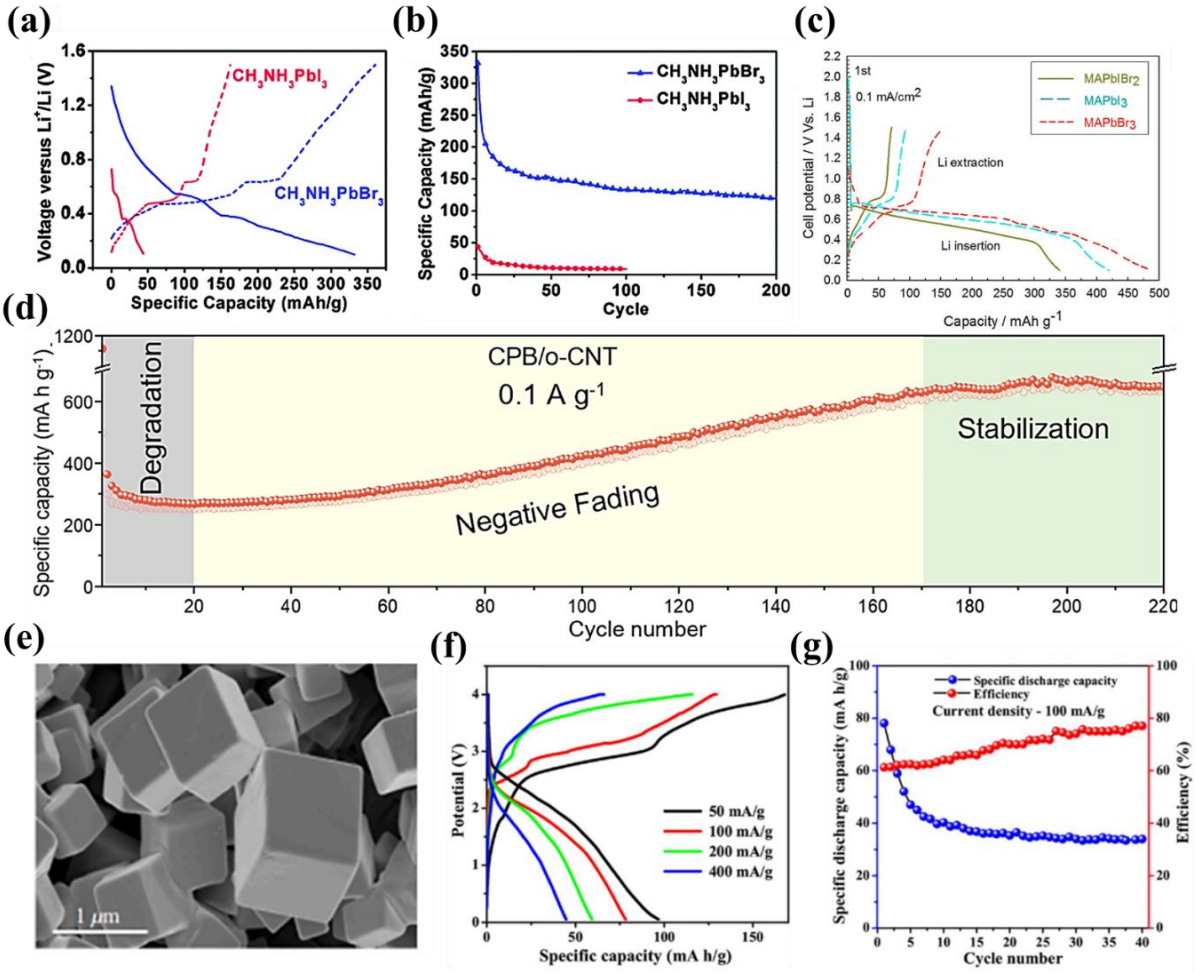

Fig. 10. Electrochemical properties of the LIBs based of $MAPbBr_3$ and $MAPbI_3$: (a) charge/discharge curves, (b) cycle stability,[85] (c) charge/discharge curves of $MAPbI_3$, $MAPbIBr_2$, and $MAPbBr_3$,[92] (d) The cycling performance of CPB/o-CNT electrode at 0.1 A $g^{-}1$ divided into three regions,[90] (e) SEM image of cubic $CsPbCl_3$. $CsPbCl_3$-graphite-based dual-ion batteries (f) Galvanostatic CD curves at various current densities and (g) Discharge capacity retention over 40 CD cycles at a current rate of 100 mA/g.[89]

remain unclear, this study suggests that halide perovskites hold promising potential for Li-ion storage applications. Several years later, research also indicates that the charge/discharge capacity can be enhanced when I- is replaced with Br ($MAPbBr_3$), as illustrated in Fig. 10c.[92] However, an incomplete substitution of Br- ($MAPbIBr_2$) leads to a decrease in

charge/discharge capacity, as the lattice parameter shifts from tetragonal $MAPbI_3$ to cubic $MAPbBr_3$. This suggests that perovskites with varying halogens exhibit different specific capacities, primarily due to two factors: (1) the influence of halogens on the crystal structures, as we covered in part 3.1, and (2) the competition between the lower atomic mass of Br- and the larger lattice parameter of I-. The effect of crystal morphology on the electrochemical performance of $MAPbBr_3$ was investigated by Q. Wang *et al*.[94] In the study, they compared five different microcrystal sizes (~2.9 mm, ~2.4 mm, ~1.9 mm, ~1.5 mm, and ~1.2 mm) and concluded that 1.2 mm-sized $MAPbBr_3$ composite electrodes exhibit unexpectedly high cycling stability for more than 1000 cycles when tested as LIB anode compared to other sizes. As compared to organometallic halide perovskites, all-inorganic halide perovskites showed better stability, ultrahigh photoluminescence quantum yield, etc. In this regard, Jiang *et al*.[95] proposed all inorganic $CsPbBr_3$ as an active material for the LIB anode in 2017 with a first charging capacity of 94.8 mAh/g and a cyclic life of 32 rounds at 60 $\mu A/cm^2$. Moreover, XH Wu et. al.[90] displays "negative fading" effect and a significant increase in capacity in $CsPbBr_3$@CNT based electrodes. This electrode delivered a specific capacity of 630 mAh/g at 0.1 A/g after 200 cycles (Fig. 10d). In addition to bromide, cubic $CsPbCl_3$ (Fig. 10e) has been developed as an anode for LIB and dual-ion batteries.

The findings indicate that the half and 275.2 mAh/g at varying current densities of 50, 100, 200, and 250 mAh/g, respectively (Fig. 10f), along with an average Coulombic efficiency of 88%. Moreover, the combination of a 3D perovskite anode with a graphitic cathode provided insights into dual-ion batteries operating within a voltage range of 0–4.0 V, averaging 2.53 V, as illustrated in Fig. 10g.[89]

Table 3. Summary of different 3D MHPs-based LIBs and their performance.

Perovskite material	**Counter electrode**	**Electrolyte**	**Potential range in V (vs. Li/Li^+)**	**Current density**	**1st cycle capacity (mAh/g)**	**Stable capacity after 'n' cycles (mAh g^{-1})**	**Ref.**
$CsPbCl_3$	$LiFePO_4$	1 M $LiBF_4$ in PVDF-HFP + $BMIMBF_4$ (1:3 w/w)	3.6–0.01	50 mA/g	612	~300 (70 cycles)	[89]
$CsPbBr_3$@CNTs	Li-metal disks	1.0 M $LiPF_6$ in EC/ DMC (1:1 vol ratio)	0.001-3.0	100 mA/g	644.6	~470.2 (200 cycles)	[96]
$CsPbBr_3$@CNTs	Li	1.0 M $LiPF_6$ in EC/ DMC/ EMC (1:1:1 vol ratio)	0.2-3 V	1 A/g	629	~376 after (900 cycles)	[96]
$CsPbI_3$	Li-metal foil	1.0 M $LiPF_6$ in a EC/ DMC (1:1 vol ratio)	0.1–3	40 mA/g	151	~235 (100 cycles)	[91]
$MAPbI_3$	Li-metal foil	$LiPF_6$ in EC/DMC (1:1 vol ratio)	0.01–2.5	100 mA/g	476	~202 (50 cycles)	[97]
$MAPbBr_3$	Li-metal foil	1.0 M $LiPF_6$ EC)/ DMC	0.01–2.5	300 mA/g	158.2	~120.1 (200 cycles)	[94]
$MAPbBr_3$	Li-metal	$LiPF_6$ in EC/EMC/ DMC(1:1:1 vol ratio)	0.2–1.4	200 mA/g	331.8	~121 (200 cycles)	[85]

Li-salt and solvent abbreviations in the electrolytes reported:

$LiPF_6$ = Lithium hexafluorophosphate, $LiBF_6$ = Lithium tetrafluoroborate, LiTFSI = Lithium bis(trifluoromethanesulfonyl)imide, LiCl = Lithium chloride, EC = ethylene carbonate; DMC = dimethyl carbonate; DEC = diethyl carbonate; EMC = ethyl methyl carbonate; PC = propylene carbonate; DOL = 1,3-dioxolane; DME = dimethoxyethane.

1.5.5. MHPs based ASEI

The major issue with LMBs is the self-derived unstable SEI, which possesses low Li-ion conductivity, low mechanical modulus, and inhomogeneous composition, which makes it difficult to achieve smooth and stable deposition/stripping of LMA.[98] Due to an inhomogeneous SEI, a non-uniform Li deposition will result, which facilitates the formation of Li dendrites. Li dendrites are capable of piercing low mechanical modulus SEI, leading to the formation of new SEIs derived from Li-metal reactions with electrolytes. During Li stripping, Li dendrites are likely to isolate from the Li bulk and turn into "dead'' Li, resulting in low Coulombic efficiency. After repeated cycling, the dendrites may grow to several hundred microns and penetrate the separators, causing short circuits and safety hazards.[99] In this regard, researchers are exploring various strategies for inhibiting dendrite growth: (a) Li-alloy anodes,[100] (b) solid-state electrolyte,[101] (c) structured anodes,[102] (d) ASEI,[103] (e) electrolyte additives,[104] and (f) interface modifications.[105] Among them, one of the most effective approaches to inhibit dendrite problems has been reported to be regulating Li ion distribution via the application of an artificial protective layer on the electrode surface, which reduces current density and strengthens the electrode/electrolyte interface stability.[106] So far, a variety of protective materials, including inorganics, polymers, and hybrids, have been applied to LMAs through various deposition methods, such as solid gas reactions, atomic layer deposition, or wet chemical emulsion coating.[107,39,108]

Choosing the materials for ASEI coating depends on the preparation conditions of thin films on LMAs, as well as the properties of the materials, such as stability against electrolytes, electron insulation, high Li-ion conduction, and flexibility confirm the changes in the volume of the LMA.[106] Currently used materials for SEI are capable of effectively separating LMAs from electrolytes and preventing spontaneous side reactions. However, structural stability and high ion conductivity are incompatible, which makes Li plating/stripping tough, further restricting LMB capacity and long-term performance. It is therefore highly desirable to develop ASEI materials that have good structural stability and Li-ion conductivity.[109] Due to its adjustable 3D framework structure and bandgap, MHPs can achieve Li-ion conduction and electronic insulation, which is expected to become a promising candidate for constructing a high-performance SEI layer. In 2020, an interfacial layer composed of solution-processed $MASnCl_3$ and $MAPbCl_3$ perovskites was developed by Yi-Chen *et al.*[110] as a new type of interfacial layer for the LMAs through a solid-state transfer process. They demonstrated

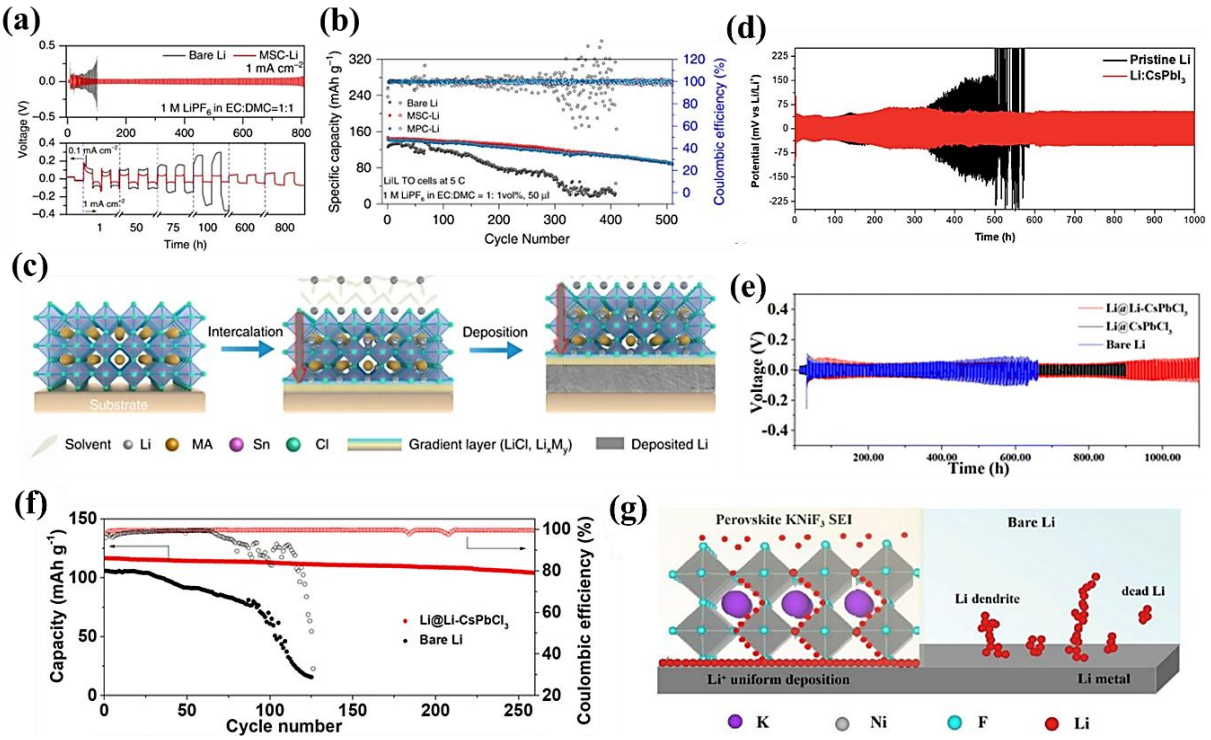

Fig. 11. (a) Galvanostatic voltage curves (top) of bare Li and MSC-Li tested with a current density of 1 mA/cm^2 for 1 mAh/cm^2, and the enlarged voltage curves during different periods (bottom). (b) Galvanostatic cycling performances of cells using LTO as cathode and bare Li, MSC-Li, or MPC-Li as anode. (c) Schematic illustration of the mechanism of Li-ions intercalation into the perovskite lattice, the formation of the perovskite-alloy gradient Li-ion conductor, and the deposition process.[110] (d) Voltage profiles of pristine Li and Li: $CsPbI_3$ symmetric cells measured at a current density of 1 mA/cm^2 and a discharge capacity of 1 mAh/ cm^2.[111] (e) Voltage-time curves of Li/Li and Li@Li-$CsPbCl_3$/Li@Li-$CsPbCl_3$ symmetric cells with an areal capacity of 1 mAh/cm^2 at a current density of 1 mA/cm^2. (f) Long-term cycling stabilities of Li/$LiFePO_4$ cells with bare Li and Li@ Li@Li–$CsPbCl_3$ anodes at a current density of 3C. [36] (g) Schematic illustration of Li plating on $KNiF_3$ perovskite SEI through the octahedral structure and on bare Li.[109]

through galvanostatic Li plating and stripping that the MSC-Li cell can be cycled for more than 800 h, much longer than the 100 h cycling life of the cell using bare Li (Fig. 11a). They also evaluated the electrochemical performance of $Li_4Ti_5O_{12}$ (LTO)/perovskite-coated LMBs at a high rate of 5C to demonstrate the efficiency of perovskite protection in LMBs. It was shown that the bare LMAs exhibit a drastic capacity decay, with a capacity of 28.3 mAh/g at the 400th cycle. In contrast, the cells using $MASnCl_3$ and $MAPbCl_3$ coated Li-anode show stable cycling for more than 500 cycles with a low capacity decay rate of 0.07 % per cycle (Fig. 11b). It was concluded that the metal chloride perovskite protection layer can ensure stable cycling of LMBs under strict conditions. Furthermore, based on DFT calculations, the researchers proposed a Li-ion transport gradient layer model that illustrated the shielding mechanism for dense deposition of Li-metal using perovskite thin films, shown in Fig. 11c.

Step 1. Only Li-ions absorption within the perovskite framework, leaving solvent molecules outside the perovskite framework.

Step 2. Intercalation and migration of Li-ions into the highly symmetric perovskite framework

Step 3. Electrochemical conversion reaction at the interface of the perovskite layer and the substrate

Step 4. Formation of both the insulating LiCl layer and the Li–M alloy layer. A Li-M layer will facilitate homogeneous Li deposition. Nevertheless, the generated LiCl can insulate electrons, preventing the perovskite from further conversion reactions, ensuring that the perovskite remains stable in its top state.

In the same year, Kaisar *et al*.[111] fabricated δ-$CsPbI_3$ as an electrochemical intercalation layer through an inexpensive and facile spray-coating method that stabilizes Li electrodes for Li-metal batteries. DFT calculations confirmed the Li-ion intercalation into the δ-$CsPbI_3$ framework, forming Li: $CsPbI_3$. Electrochemical testing of a Li: $CsPbI_3$ symmetric cell revealed dendrite-free plating after 1000 h at a current density of 1 mA/cm^2 and discharge capacity of 1 mAh/cm^2 (Fig. 11d). In this new and simple method, derogatory dendrites are avoided, thereby enabling the preparation of LMAs for practical application in high-density LMBs. Recently, Liu et. al.[112] developed Li-doped $CsPbCl_3$ ASEI. They demonstrated that Li-$CsPbCl_3$ not only successfully inhibits the formation of Li dendrites but also promotes the movement of Li-ions at the interface and encourages the ultra-dense and even deposition of Li, creating a beneficial setting for stable Li electroplating/stripping and greatly enhancing the electrochemical performance of LMBs (Fig. 11e, f). However, hybrid perovskites such as $MAPbCl_3$ and $MASnCl_3$ are prone to decomposition when exposed to photo-, thermal-, or moisture-stresses.[113,114] Furthermore, the cubic phase of $CsPbI_3$ is thermodynamically unstable at room temperature, which may result in a blocking of Li-ion transfer channels. In addition to that, lead-based perovskites are highly toxic, which makes them unsuitable for LMBs. Therefore, perovskite materials that are non-toxic and have a high moisture- and thermal stability would be better suited to Li-metal SEI. In this regard, Y. Zhang *et al*.[109] developed air-stable fluoride perovskite ($KNiF_3$), which is applied as an SEI layer to induce uniform Li deposition for an air-stable and dendrite-free LMA. In their study, they demonstrated that symmetric cells protected by $KNiF_3$ SEI maintain high cycling stability over a period of 3000 hours at a capacity of 4 mAh/cm^2. When coupled with commercial $LiFePO_4$ cathodes (LFP,

13.3 mg cm^{-2}), LFP||Li-$KNiF_3$ batteries show promoted cycling stability and rate capability, much better than the bare Li. Even though MHPs are capable of improving cycling performance, rate capability, and stability. Moreover, they also reveal the protection mechanism of the perovskite SEI through DFT calculation. They demonstrated that Li-ion migrated along the octahedral structure of the perovskite while maintaining the 3D cubic framework without decomposition or phase transition (Fig. 11g).

1.6. Thesis Aim and Objective

The main goal of this thesis is to come up with and assess innovative strategies aimed at boosting the electrochemical performance and interfacial stability of LIBs. This is done by using cesium lead chloride ($CsPbCl_3$), as both an active anode material and a protective coating for anode materials. With the increasing demand for batteries that offer high energy density and long life, traditional anode materials like graphite and Li-metal have some serious drawbacks, such as low theoretical capacity, dendritic growth, and unstable SEI formation. This research aims to tackle these issues by investigating how $CsPbCl_3$ can enhance anode performance and reduce degradation at the electrode/electrolyte interfaces. The first goal of the thesis is to explore the electrochemical behavior of $CsPbCl_3$ when used as an active anode material in Li half-cell setups. To do this, carbonate-based liquid electrolyte systems have been tested. This helped us understand how the composition of the electrolyte affects capacity, cycling stability, and interfacial reactions. The aim is to clarify the Li-ion storage mechanism in $CsPbCl_3$ through post-cycling analyses like XPS and XRD, which will help identify key processes such as Li-ion intercalation, conversion reactions, and potential alloy formation. The second goal is to use $CsPbCl_3$ as a protective coating for Li-metal anodes. While Li-metal has an impressive theoretical capacity, it suffers from issues like dendritic growth and ongoing SEI reformation, which can jeopardize safety and lifespan. By applying a $CsPbCl_3$ layer using a straightforward drop-casting method, this research aims to assess its effectiveness in stabilizing the Li surface, reducing dendrite formation, and improving Coulombic efficiency.

The final aim here is to apply the $CsPbCl_3$ coating technique to graphite as well as Si anodes to find out whether this coating can enhance interfacial properties, control the formation of the and boost the long-term cycling performance of half-cells. By tackling these goals, this thesis aims to deepen our understanding of MHPs as effective materials for next-generation battery systems, laying the groundwork for their use in practical, high-performance LIB designs.

Chapter 2
Materials and methods

This chapter discusses the list of chemicals, the preparation method of perovskite material and the battery components, and the fundamental ideas behind each measurement, and the characterization techniques to analyze the performance of our materials in this dissertation.

2.1. List of chemicals

Cesium chloride (CsCl, Sigma-Aldrich, 99.9%), lead chloride ($PbCl_2$, Sigma-Aldrich, 98%), sodium dodecylsulfate (SDS, Sigma-Aldrich, 99.5%), Li bis(fluorosulfonyl)-imide (LiFSI, Solvionic, 99.9%), and Li iron phosphate ($LiFePO_4$/C, LFP, Targray, SLFP02002) were used as received, tetrahydrofuran (THF, Honeywell, ≥ 99.9%) was dried using 4 Å molecular sieves for a minimum of 5 days. Subsequently, it was refluxed overnight with a sodium-potassium (Na/K) alloy (approximately 1 mL/L) and then purified through fractional distillation. The final water content of the distilled solvent was confirmed to be below 1 ppm, as determined by Karl Fischer titration, fluoroethylene carbonate (FEC, Alfa Aesar, 98%), anhydrous diethyl carbonate (DEC, Sigma-Aldrich, 99%), polyvinylidene fluoride (PVdF, Sigma-Aldrich), N-methyl-2-pyrrolidone (NMP, Merck, ≥ 99.7%), dimethyl sulfoxide (DMSO, Merck, ≥ 99.7%), toluene (Merck, ≥ 99.5%), Li bis(trifluoromethanesulfonyl)imide (LiTFSI) in 1,3-dioxolane (DOL): dimethyl ether (DME) in (1:1), super P were used without any further treatment. Graphite electrodes (Sigma-Aldrich, active material loading 6.3 mg/cm^2, 15-20 μm (active material characteristic), Si-anodes (CIC energiGUNE)

2.2. Preparation of $CsPbCl_3$

Preparation methods of MHPs, alongside the chemical composition, are one of the key factors influencing the physicochemical properties of the title materials. To date, numerous techniques for obtaining MHPs have been applied. In this study, two synthesis approaches have been used to synthesize the $CsPbCl_3$ perovskite: (a) Mechanochemical and (b) solution synthesis. Both methods offer distinct advantages for creating MHPs. Mechanochemical synthesis, a solvent-free method, excels in speed and environmental friendliness, while solution-based methods offer better control over crystal size, morphology, and stoichiometry.

2.2.1. Mechanochemical approach

Equimolar amounts of CsCl and $PbCl_2$ were used for the mechanosynthesis of the desired product via planetary ball milling. The precursors were accurately weighed and initially homogenized by hand grinding using a mortar and pestle. The resulting uniform mixture was transferred into a 50 mL zirconia jar containing eight zirconia balls (10 mm diameter) with a ball-to-powder ratio of 10:1. The jar was sealed under an inert atmosphere inside a glove box to prevent any moisture or air exposure. Subsequently, the sealed jar was placed in a planetary ball mill and subjected to solid-state milling at a constant rotational speed of 600 rpm for 4.5

hours at room temperature. After milling, the synthesized powder was collected and analyzed using various characterization techniques.

2.2.2. Solution-based approach

$CsPbCl_3$ perovskite was synthesized according to a previously reported method.[115] Equimolar amounts of CsCl, $PbCl_2$, and SDS powder were stirred in DMSO at room temperature for 1.5 h. After complete dissolution, the precursor solution was injected into toluene antisolvent under vigorous stirring. A white colloidal solution was formed. After stirring for 2 minutes, the resulting solution was centrifuged at 8000 rpm for 10 minutes. The supernatant was discarded, and the $CsPbCl_3$ precipitate was dispersed in toluene. Two more cycles of washing were carried out under the same centrifugation conditions. Finally, the white $CsPbCl_3$ powder was dried overnight in a vacuum oven at 80° °C. The obtained perovskite was subsequently characterized.

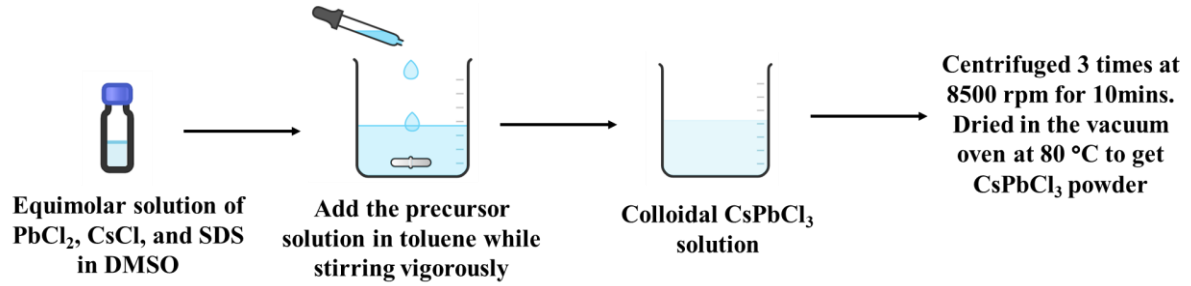

Fig. 12. Schematic illustration of the synthesis of $CsPbCl_3$ following a solution-based approach.

2.3. Synthesis and Assembly of Battery Materials

2.3.1. Fabrication of $CsPbCl_3$ electrodes

To fabricate the working electrode (WE), a homogeneous slurry was prepared by mixing mechanochemically synthesized $CsPbCl_3$, conductive carbon black (Super P), and PVDF in a weight ratio of 60:30:10 and 70:20:10, using N-methyl-2-pyrrolidone (NMP) as the solvent. The mixing was carried out inside a glove box (with H_2O and O_2 levels < 1 ppm) using a mortar and pestle for approximately 20 minutes. The resulting slurry was then coated onto a copper foil using the doctor blade technique with a blade gap of 250 µm and subsequently dried at 100 °C overnight under vacuum. Circular electrode discs, 11 mm in diameter, were punched out and used as working electrodes for structural characterization and electrochemical analysis. The prepared WE were stored in an argon-filled glovebox to prevent moisture and air exposure. The electrodes with 60:30:10 composition contained an active material loading of ~ 1 mg/cm^2 and 70:20:10 composition contained an active material loading of ~1.3 mg/cm^2

2.3.2. Fabrication of LFP cathodes

LFP cathodes with a mass loading of approximately 7.5 mg/cm^2 of active material. LFP cathodes were prepared using a planetary ball mill equipped with a 12 mL stainless steel container and five stainless steel balls (16 mm in diameter). A mixture of LFP, conductive carbon black (C65), and polyvinylidene fluoride (PVdF) in a weight ratio of 90:5:5 was milled at 300 rpm for 30 minutes in the presence of NMP as the solvent to obtain a homogeneous slurry. The resulting slurry was uniformly coated onto a double carbon-coated aluminium foil using a doctor blade set with a 200 µm gap. The coated electrodes were subsequently dried under vacuum at 100 °C overnight. After drying, the cathode films were punched into 10 mm diameter disks. The disks were then compressed at a pressure of 2 tons/cm² to ensure uniformity. Finally, the prepared cathodes were stored in an argon-filled glovebox to prevent exposure to moisture and air.

2.3.3. Fabrication of $CsPbCl_3$ protected electrodes

There are various techniques to develop protective coatings on Li-metal and graphite electrodes. In this report, we employed $CsPbCl_3$ as a protective coating by using a simple drop-casting method. Before the coating process, Li-metal disks with a thickness of 500µm were punched out to a diameter of 12 mm and mechanically polished by using a polystyrene weighing vessel. The coating dispersion was prepared by grinding a fixed amount (20 mg) of $CsPbCl_3$ perovskite in a mortar and pestle for 5-8 minutes to obtain a fine powder. The ground

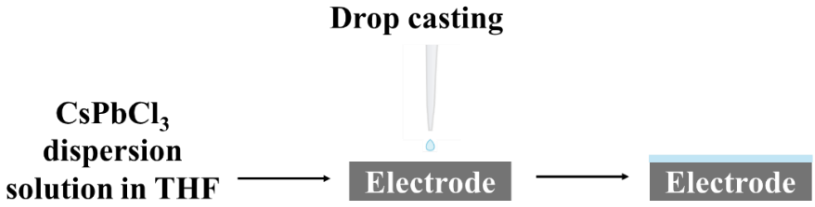

Fig. 13. Schematic illustration of the fabrication of $CsPbCl_3$ protective coating on Li-metal via the drop casting technique.

perovskite was then dispersed in 1.5 mL of anhydrous tetrahydrofuran (THF), and the resulting mixture was stirred vigorously for 24 hours to achieve a homogeneous dispersion. All procedures were conducted in an inert atmosphere within an argon-filled glovebox (MBraun Unilab, with H_2O and O_2 levels < 1 ppm). The protective coating was applied using a drop-casting technique, where 37.5 µL/cm^2 of the dispersion was deposited onto the polished Li-metal surface in four successive layers to achieve a total loading of 2 mg/cm^2. The same procedure is followed to coat the graphite electrodes.

2.3.4. Coin cell assembly

In this study, CR2450 coin cells were assembled in an argon-filled glovebox ($O_2/H_2O < 1$ ppm) to evaluate the electrochemical performance of halide perovskite-based anodes. The assembly process was carried out as follows: The negative casing (stainless steel) was placed on a clean surface, and a stainless steel spacer was inserted at the base. A Li-metal foil (13 mm in diameter) was carefully placed on top of the spacer, serving as the counter and reference electrode. Next, a Celgard 2320 separator (PP/PE/PP, 16 μm thickness) was laid over the Li-metal foil. Approximately 15 μL of electrolyte was added to ensure full wetting of the separator. The working electrode (11 mm diameter), comprising the halide perovskite-based active material/coated graphite, was then positioned directly above the separator. Another 15 μL of electrolyte was added to fully soak the interface between the working electrode and separator. A second stainless steel spacer and a spring were placed on top of the electrode to maintain uniform pressure during cycling. Finally, the positive casing (coin cell cap) was placed over the stack, and the cell was sealed using a hydraulic crimping machine. The cells were tested in 1 M LiFSI in FEC: DEC in a 1:2 volume ratio electrolyte system.

2.3.5. Pouch cell assembly

All electrochemical tests for $CsPbCl_3$-based ASEIs on Li and graphite electrodes were conducted in pouch cell format using a VMP3 Biologic potentiostat/galvanostat. For Li||Li symmetric cells with Cu contacts, two Li electrodes (12 mm in diameter) were stacked with a pressed Celgard 2320 separator (PP/PE/PP, 16 μm thickness), yielding an electrochemically active area of 0.502 cm^2 to minimize edge effects.[116] A similar assembly procedure was followed for Li||Cu asymmetric cells. Full-cell configurations were evaluated by pairing both bare and $CsPbCl_3$-coated Li anodes with LFP cathodes. These Li||LFP full cells were assembled using an unpressed Celgard 2320 separator and Al/Cu current collectors. Similarly, graphite||Li half-cells using both coated and uncoated graphite anodes were assembled using the same approach. Electrolyte volumes were fixed at 20 μL for Li||Li and Li||Cu cells, and 30 μL for Li||LFP, graphite||Li, and Si||Li cells. All cells employed 1 M LiFSI in FEC: DEC (1:2 by volume) as the electrolyte. Furthermore, the effectiveness of the coating was analysed in Li||Li and Li||LFP cell configuration with conventional electrolyte LP40.

2.4. Structural characterization

2.4.1. Scanning Electron Microscopy (SEM)

In this study, SEM, Supra 35VP, Carl Zeiss, equipped with an energy-dispersive X-ray spectrometer (INCA Energy 400, Oxford Instruments, UK), was utilized to investigate the thickness, morphology, and microstructure of the MHP-based anodes and ASEI on Li-metal. Sample preparation was conducted in an argon-filled glovebox to prevent atmospheric exposure, and the samples were transferred to the SEM chamber using a custom-designed vacuum transfer holder. The holder was opened only under reduced pressure within the SEM chamber to maintain the integrity of the samples. Moreover, the thickness of the protective layer was determined using cross-sectional SEM. To preserve the structural integrity of the coating, the sample was frozen by immersion in liquid nitrogen while enclosed in a sealed pouch bag.

2.4.2. X-ray Diffraction (XRD)

In this study, XRD was acquired on a X'Pert PRO diffractometer (Malvern Panalytical) with Cu Kα radiation (λ= 1.541874 Å). The powder as well as electrode samples were prepared on a zero-background Si holder and measured in the 2θ range from 5° to 80° with a step size of 0.008° per 800 s by using a fully opened Pixcel detector. Moreover, the samples for the *ex-situ* XRD measurements were prepared on a Si wafer and covered with Kapton foil in the glovebox.

2.4.3. X-ray Photoelectron Spectroscopy (XPS)

XPS was conducted using VersaProbe III AD (Physical Electronics, Chanhassen, U.S.A.) with a monochromated Al-Kα1 X-ray (1486.7 eV) excitation source. The spectra were acquired from an area of 1 mm² using a 200 µm spot size. The perovskite powder and electrodes were placed on a non-conductive double-sided tape in “floating” conditions. High-resolution spectra were measured at 69 eV pass energy and steps of 0.05 eV. Charge neutralization was employed, and the energy scale of the XPS spectra was calibrated by setting the C 1*s* peak of carbon to a binding energy of 284.8 eV. The spectra were analyzed using UIVAC-PHI Multipack software, with a binding energy error of ± 0.65 eV for all peak fits. A smart background was applied to all the spectra.

2.5. Electrochemical characterization

2.5.1 Galvanostatic cycling

To investigate the Li storage performance of the $CsPbCl_3$ anode, under coin cell type was used. The coin cells were rested for 6 hours and then cycled in the voltage range of 0.05 V to 2 V *vs.* Li^0/Li^+. Three formation cycles were conducted at 10A/g current density. The long-term cycling of these electrodes was performed at 50 A/g current density. To examine the efficiency of $CsPbCl_3$-based protective coating on Li-metal, galvanostatic stripping/plating tests were carried out on Li||Li symmetric cells incorporating either bare or coated Li electrodes. The tests were conducted at a constant current density of 1 mA/cm^2, 2 mA/cm^2, and 4 mA/cm^2 with a plating capacity of 1 mAh/cm^2, 2 mAh/cm^2, and 4 mAh/cm^2

Coulombic efficiency (CE) measurements for Li||Cu cells were performed following a previously reported protocol.[116] Using both bare and coated Cu electrodes. The procedure began with a single preconditioning cycle involving Li plating and stripping at a capacity of 4 mAh/cm^2 and a current density of 0.4 mA/cm^2. Subsequently, a Li reservoir was formed by plating Li onto the Cu electrode at the same current density and capacity. This was followed by 10 plating/stripping cycles with an areal capacity of 0.5 mAh/cm^2, maintaining the current density at 0.4 mA/cm^2. Finally, the remaining Li was fully stripped from the Cu electrode at 4 mAh/cm^2 and 0.4 mA/cm^2, with the upper voltage limit set to 1 V. The CE was calculated by comparing the Li capacity deposited during the reservoir formation with the capacity recovered during the final stripping step. Additionally, a modified version of the protocol was also employed, wherein three preconditioning cycles were performed instead of one to study the impact of initial cycling on CE. The full cells with LFP cathodes were tested in a potential range between 2.5 V and 3.6 V *vs.* Li^0/Li^+ with three formation cycles at C/10 and 1C for the following cycles. The effectiveness of the coating on the graphite and Si electrodes was tested in a half-cell system in a potential range between 0.01 V-2 V and 0.01-1V *vs.* Li^0/Li^+, respectively. Three formation cycles at C/10 were performed before the following cycles at 1C.

2.5.2. Cyclic Voltammetry (CV)

CV on bare Li||LFP and $CsPbCl_3$ coated Li||LFP cells was performed at 0.1 mV/sec scan rate between the voltage range of 2.5 V to 3.6 V.

2.5.3. Electrochemical Impedance Spectroscopy (EIS)

(a) Li-transference number study: Three different approaches have been employed to determine the transference number for both bare Li and coated Li-cells: Bruce-Vincent polarisation method, low frequency EIS measurement of pristine cells @OCV, and first spectrum *operando* EIS measurement. From each of these methods, the electrolyte resistance (R_{el}) and Warburg resistance (R_W) were obtained. The former was determined as the high-frequency resistive intercept from the impedance spectra. The latter was determined as the low-frequency resistive intercept in the PEIS@OCV measurements or calculated as the difference between the sum of the electrolyte and SEI resistances and the total resistance calculated from the overpotential and applied current.

For bare Li cells, the transference number was 0.10 ± 0.03, and for the coated Li cell, 0.09 ± 0.02.

(b) *Operando* electrochemical impedance spectroscopy: In *operando* impedance spectroscopy measurements (OEIS), there is no waiting period to allow the cell to equilibrate between changes in its state of charge and the acquisition of impedance spectra. Instead, the impedance is recorded continuously while the cell is being cycled. During this process, a small-amplitude AC signal used for impedance measurement is superimposed onto a DC signal that drives the electrochemical cycling of the cell. To ensure the accuracy and stability of the measurements, multiple impedance spectra are typically recorded in succession at each potential step. However, it is important to note that the spectra collected during rapid changes in potential, such as during the onset or end of voltage plateaus, may be less reliable due to the non-steady-state conditions during these transition periods. In this study, OEIS was utilized to evaluate the interfacial and diffusion resistance of both bare and coated Li electrodes while cycling the cell. For these experiments, Li||Li symmetric cells were assembled and allowed to stabilize for 24 h while measuring the EIS at OCV. The OCV EIS spectra were recorded from 1 MHz to 1 mHz, using a sinusoidal potential amplitude of 10 mV (root mean square, rms). OEIS was carried out at a current density of 1 mA/cm^2 and with an areal capacity of 1.0 mAh cm^{-2}. The alternating current amplitude was 100 µA/cm^{2,} and the frequency range was between 1 MHz and 20 mHz. Each cell was cycled for a total of 20 cycles under these standard cycling conditions.

Chapter 3
Results and discussion

This chapter presents the key findings of the dissertation, focusing on the use of $CsPbCl_3$ as both an active anode material and a protective interfacial coating in Li-based batteries.

In the first section, $CsPbCl_3$ was investigated as an anode material in Li||$CsPbCl_3$ half-cells using two electrolyte systems. XPS and XRD analyses revealed a multi-step Li storage mechanism involving Li^+ insertion, conversion, and alloying.

The second section explored $CsPbCl_3$ as a protective coating for Li-metal anodes. Coated Li electrodes were tested in symmetric (Li||Li), asymmetric (Li||Cu), and full (Li||LFP) cells. The coating improved cycling stability, reduced overpotential, and promoted uniform Li deposition, as confirmed by post-cycling XPS.

Finally, the same coating approach was applied to graphite and Si anodes. The $CsPbCl_3$ layer enhanced electrochemical performance and stability in the half-cells, likely by regulating SEI formation and mitigating structural degradation.

A part of this chapter has been accepted for publication in the Chemistry of Materials Journal: Juhi Juhi, Mariana Vargas Ordaz, Sara Drvarič Talian, Elena Tchernychova, Wladyslaw Wieczorek, Janusz Lewiński, Robert Dominko. "Cesium Lead Chloride as Artificial Solid Electrolyte Interface for Enhanced Anode Protection in Lithium metal Batteries". DOI: 10.1021/acs.chemmater.5c01666

3.1. $CsPbCl_3$-based anodes for Li batteries

3.1.1. Optimization of mechanochemically synthesized $CsPbCl_3$ perovskite powder

The structural, elemental, and morphological optimization of the mechanochemically synthesized $CsPbCl_3$ perovskite powder was conducted using XRD, XPS, and SEM, with the corresponding results presented in Figs. 14, 15, and 16. The XRD pattern of the $CsPbCl_3$ sample exhibited sharp and well-defined peaks, indicating high crystallinity of the perovskite powder. Moreover, the detailed analysis of the diffraction pattern confirmed the formation of the tetragonal perovskite phase as a major phase and the orthorhombic minor phase.

The crystal structure and phase purity of the sample were further confirmed through phase

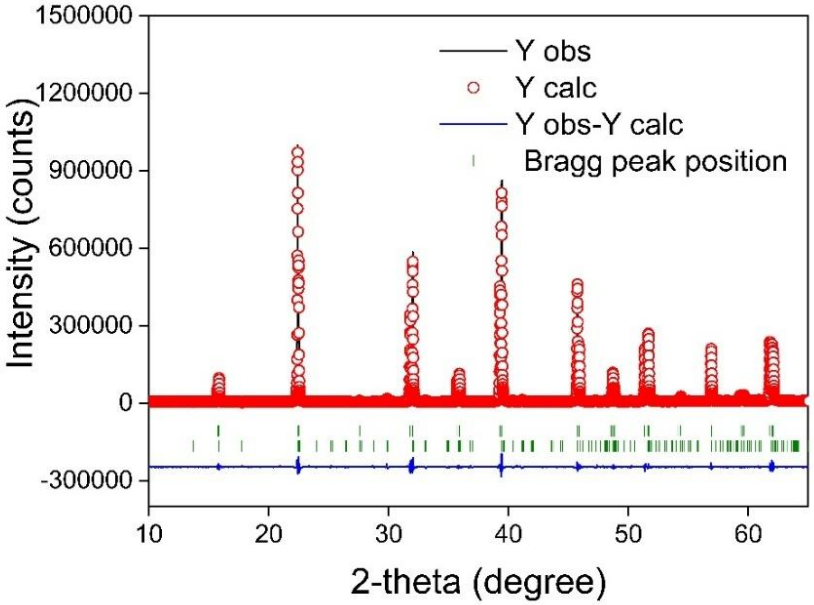

Fig. 14. XRD pattern (solid black line, Yobs) for $CsPbCl_3$ powder. Phase identification analysis (red dotted line, Ycalc) using the profile fitting FullProf Suite program. The horizontal (blue solid line) represents the residual, and the vertical lines (green solid lines) are the Bragg positions.

identification using the FullProf Suite. Structural refinement was carried out using the *P4mm* space group for the tetragonal phase and *Pnma* for the orthorhombic phase. The computed values of the lattice parameters for both phases are given in Table 4. To have a better understanding of the chemical composition and chemical state of each element in the perovskite, XPS measurements were conducted. The characteristic cesium (Cs), chlorine (Cl), and lead (Pb) peaks are presented in Fig. 15. Two peaks centered at 738.08 and 724.03 eV are the $3d_{3/2}$ and $3d_{5/2}$ bands of Cs, respectively. The Pb $4f_{5/2}$ and Pb $4f_{7/2}$ peaks are respectively located at 142.91 and 138.05 eV.

Table 4. Lattice parameters of mechanochemically synthesized $CsPbCl_3$ perovskite

Lattice parameters (Å)	Tetragonal (P4mm)	Orthorhombic (Pnma)
a	5.589207	7.861912
b	5.589207	11.178487
c	5.626069	7.926983

The Cl $2p_{3/2}$ and Cl $2p_{1/3}$ peaks are centered at 199.21 and 197.60 eV, respectively. The displayed characteristic binding energies (BEs) for Cs, Pb, and Cl are in good agreement with previously reported values for $CsPbCl_3$ perovskite.[117]

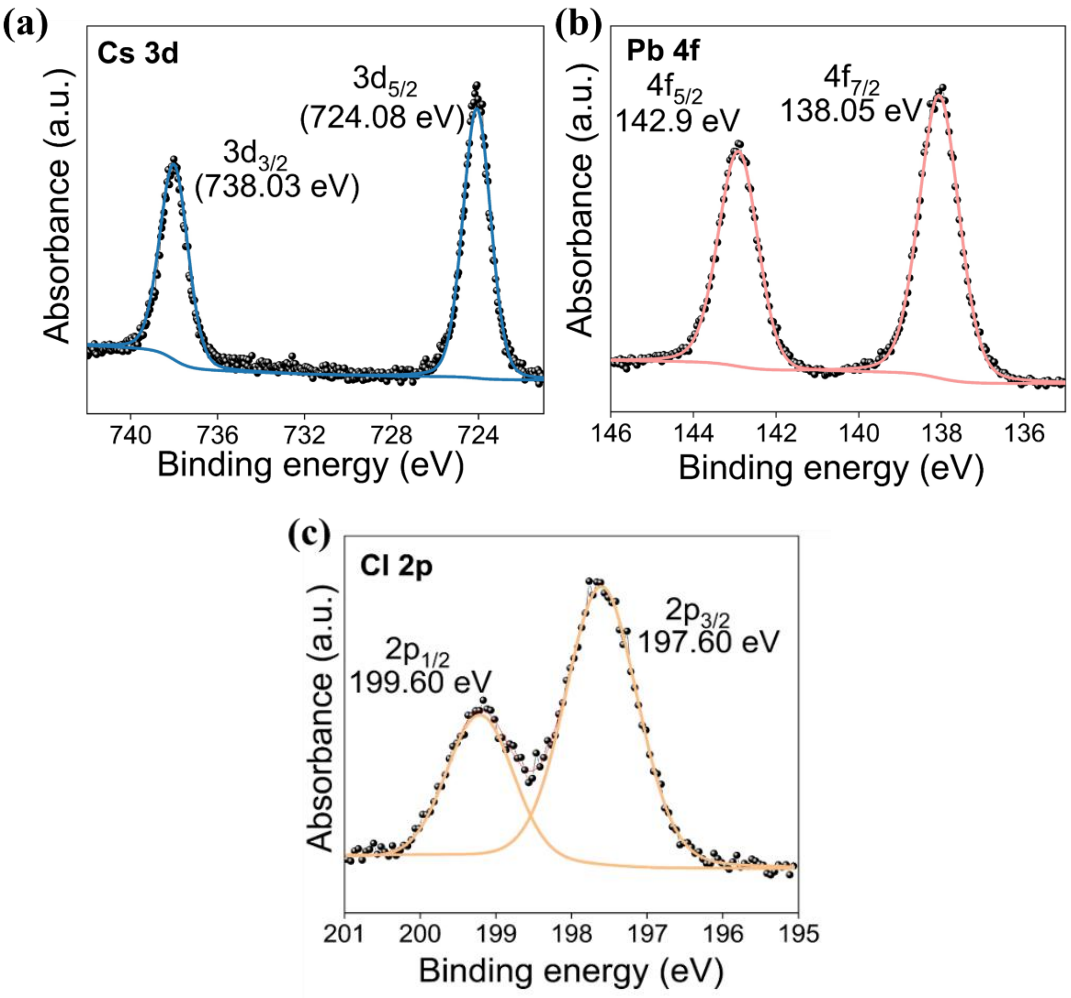

Fig. 15. XPS spectrum of the $CsPbCl_3$ powder (a) Cs 3d, (b) Pb 4f, and (c) Cl 2p peak positions.

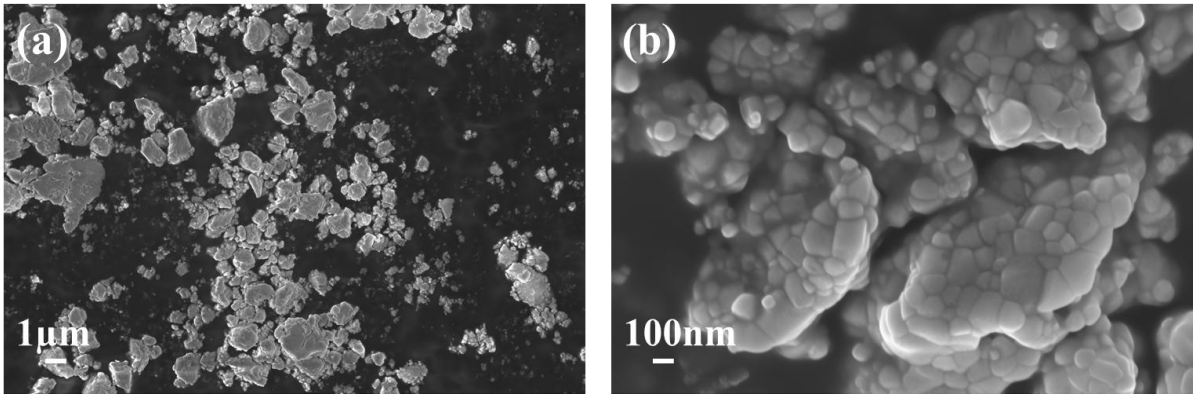

Fig. 16. SEM images of $CsPbCl_3$ powder (a) 10 Kx and (b) 100 Kx magnification.

SEM combined with EDX was performed on $CsPbCl_3$ powder at two different magnifications, as shown in Figs. 16 and 17. The SEM images reveal that the perovskite powder consists of agglomerated particles with irregular shapes (Fig. 16) and a broad size distribution ranging from a few hundred nanometers up to a few micrometers (Fig. 17a).

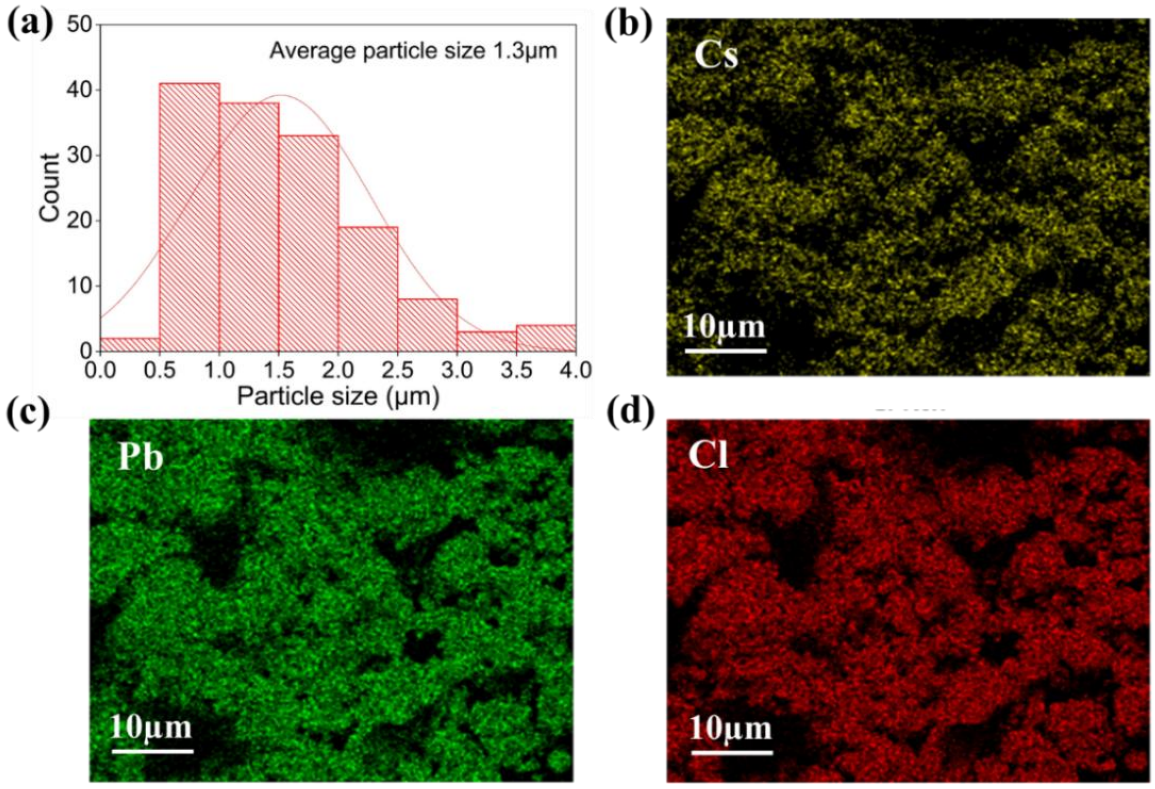

Fig. 17. (a) Average particle size and (b-d) EDX elemental mapping of Cs, Pb, and Cl of $CsPbCl_3$ perovskite powder.

From the highly magnified SEM image (Fig. 16b), it is evident that the large particles are composed of smaller crystallites. These smaller crystallites exhibit well-defined grain boundaries, a characteristic feature of crystalline $CsPbCl_3$. Moreover, EDX mapping (Fig. 17 b-

c) confirmed the homogeneous distribution of Cl, Cs, and Pb elements within the $CsPbCl_3$ powder.

3.1.2. Optimization of $CsPbCl_3$ based anodes

The XRD (Fig. 18a) of the fabricated $CsPbCl_3$ electrode shows that the characteristic reflections remain unchanged compared to the pristine $CsPbCl_3$ powder, indicating that the crystalline structure is preserved after electrode preparation. Fig. 18 (b) and (c) present the SEM images of the $CsPbCl_3$-based electrode. In Fig. 18b, a fairly uniform distribution of cubic-shaped

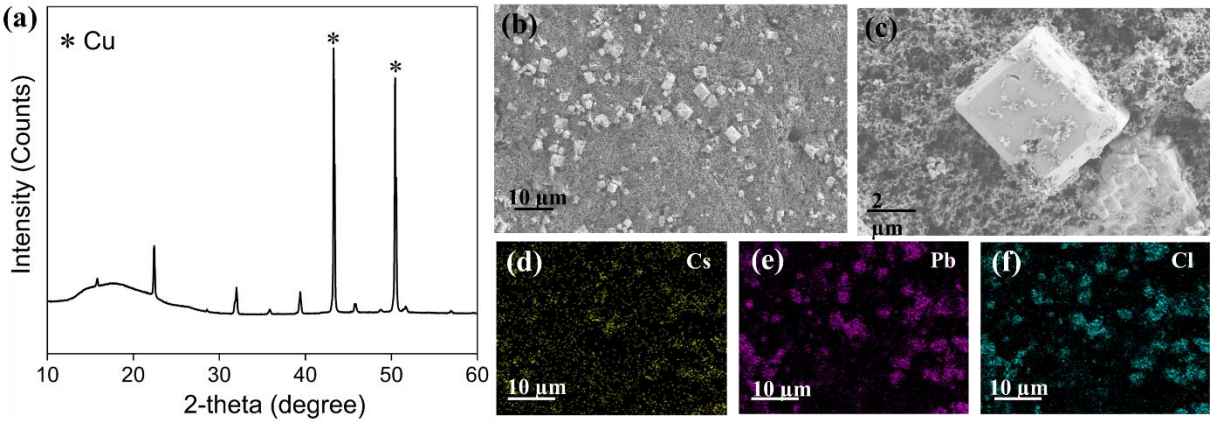

Fig. 18. (a) XRD pattern and SEM images (b) 1.6 Kx and (c) 20 Kx magnification, and (d-f) EDX elemental mapping of Cs, Pb, and Cl of $CsPbCl_3$ anode.

$CsPbCl_3$ particles is spread across the surface of the electrode. These particles maintain their unique cubic shape (typical of the crystalline perovskite phase), even though they are embedded in a porous and textured matrix made up of PVDF and carbon black. The enlarged SEM image (Fig. 18c) clearly shows that the defined cubic perovskite particles. It is interesting to note that in contrast to the pristine $CsPbCl_3$ powder (Fig. 16), where the individual particles showed irregular agglomerated shapes formed by nanocrystallites, the electrode features more distinct, isolated cubic crystals. This can hint that the electrode formulation and the film-casting process, may have recrystallized the particles during drying at elevated temperature (100° C, under vacuum). From the EDX mapping (Fig. 18d- f), it can be seen that the Cs, Pb, and Cl elements are distributed throughout the electrode surface.

To gain deeper insight into the chemical composition and oxidation states of the elements present in the $CsPbCl_3$-based electrode, XPS analysis was performed. The survey XPS spectrum is shown in Fig. 19a, confirming the presence of all the constituent elements of $CsPbCl_3$, along with an additional fluorine (F) signal attributed to the PVDF binder used in the

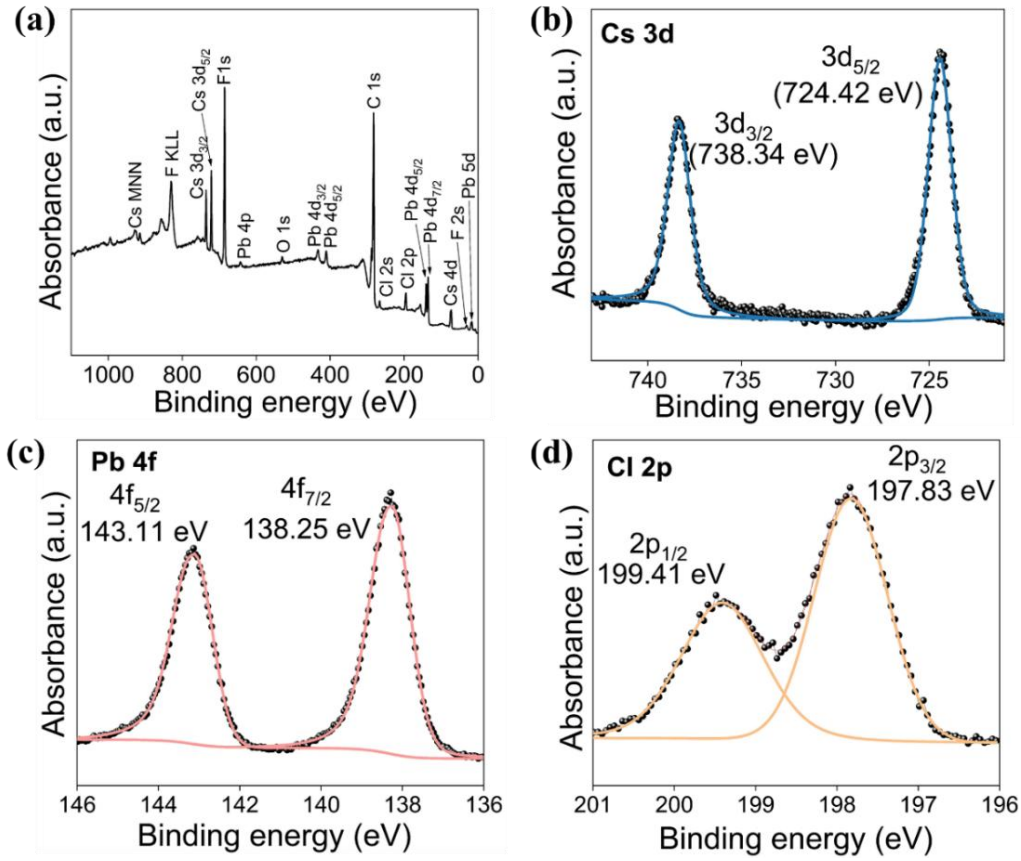

Fig. 19. (a) Survey XPS spectrum of $CsPbCl_3$ powder and, XPS spectrum of the $CsPbCl_3$ powder (a) Cs 3d, (b) Pb 4f, and (c) Cl 2p peak positions.

electrode formulation. High-resolution XPS spectrum of the individual elements are presented in Fig. 19b-d. The Cs 3d spectrum exhibits two distinct peaks located at BEs of 738.34 eV and 724.42 eV, corresponding to the Cs $3d_{3/2}$ and Cs $3d_{5/2}$ spin-orbit components, respectively. The Pb 4f region displays two prominent peaks at 143.11 eV and 138.25 eV, attributed to Pb $4f_{5/2}$ and Pb $4f_{4/2}$, respectively. Similarly, the Cl 2p spectrum reveals peaks at 199.42 eV (Cl $2p_{1/2}$) and 197.83 eV (Cl $2p_{3/2}$).

The BEs observed for Cs, Pb, and Cl are in agreement with those measured for the pristine $CsPbCl_3$ powder, as shown in Fig. 15, indicating that the chemical states of these elements remain unchanged during the electrode fabrication process.

3.1.3. Electrochemical performance of $CsPbCl_3$||Li half cells

To evaluate the electrochemical performance of $CsPbCl_3$ as an anode material, Li||$CsPbCl_3$ half-cells were assembled using two different electrode compositions, namely 60:30:10 and 70:20:10 (active material: carbon black: PVDF binder). Both cell configurations were subjected to three galvanostatic formation cycles at a current density of 10 mA/g within the voltage

window of 0.05–2.0 V in 1 M LiFSI in FEC: DEC (1:2). The initial specific discharge capacity of the 60:30:10 electrode reached ~ 600 mAh/g, which was higher than that obtained for the 70:20:10 electrode (Fig. S1). Based on this result, the 60:30:10 composition was selected for subsequent experiments. Furthermore, the potential profile of the first discharge revealed a characteristic three-step Li-ion storage process, as evidenced by the distinct voltage plateaus (Fig. 20a). To further elucidate the underlying phase evolution, *ex-situ* XRD was performed at selected states of discharge (2 V, 1 V, and 0.05 V; Fig. 20b).

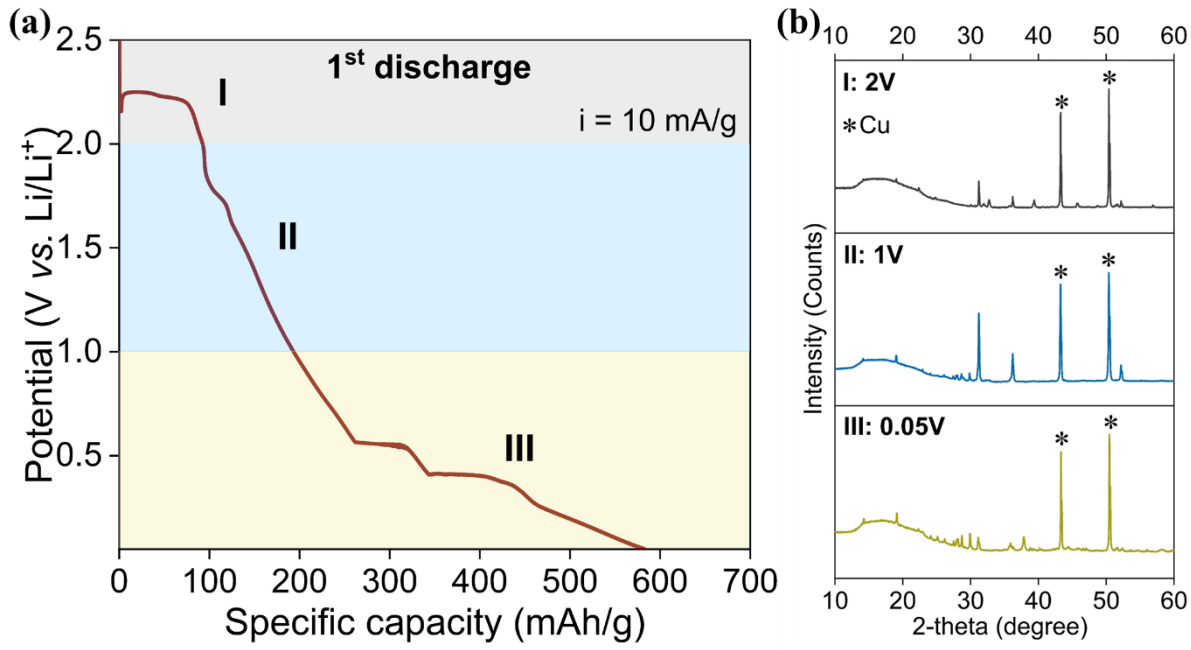

Fig. 20. (a) 1st cycle discharge curve and (b) *ex-situ* XRD pattern at different voltages of $CsPbCl_3$ anode.

At 2V (region I), the perovskite begins to decompose, and new reflections corresponding to metallic Pb and very weak LiCl reflections are already starting to appear, along with the traces of the pristine $CsPbCl_3$. Moreover, the peaks related to $CsLi_2Cl_3$ salt can also be observed. When discharged to 1 V (region II), the perovskite reflections disappear completely, confirming the full breakdown of $CsPbCl_3$. At this stage, the metallic Pb peaks become more intense, indicating the growth of crystalline metallic Pb, while $CsLi_2Cl_3$ remains present. On further discharge to 0.05 V (region III), the metallic Pb reflections start to shrink, which is due to consumption of Pb through alloying with Li, resulting in new Li-Pb intermetallics (LiPb, $Li_{22}Pb_5$ or Li_8Pb_3) peaks. Minor residual $CsLi_2Cl_3$ can still be detected. Overall, phase assignments at 2 V → 1 V → 0.05 V show conversion–alloying mechanism: perovskite conversion to Pb + salts + LiCl, then Pb alloying with Li.

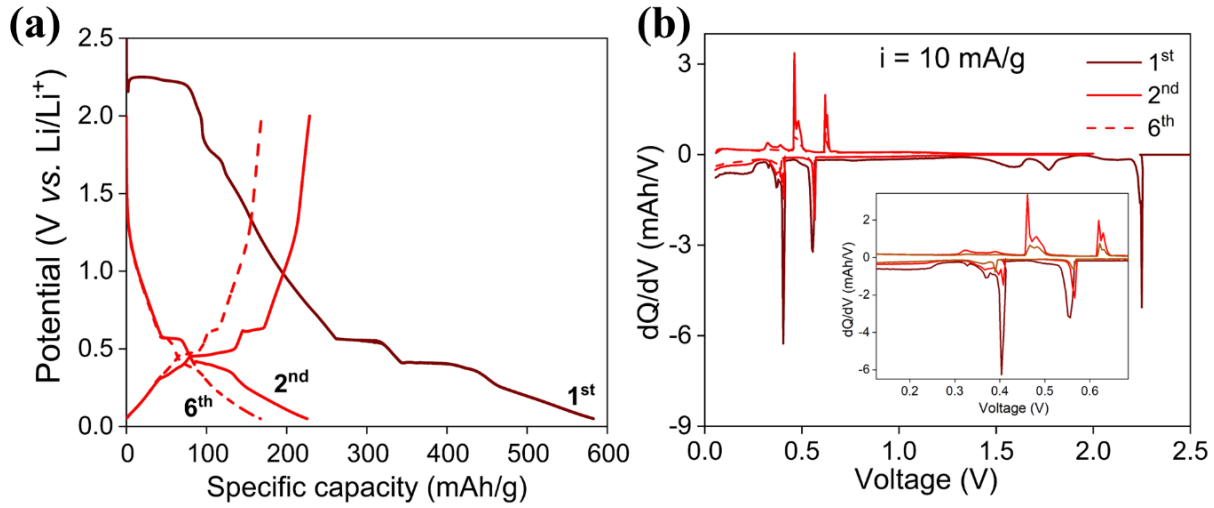

Fig. 21. Charge discharge profiles of $CsPbCl_3$ electrode and (b) their corresponding differential curves.

After the first discharge, the reversible capacity of $CsPbCl_3$ decreases significantly (Fig. 21a), which can be directly correlated with the conversion-alloying mechanism observed in the XRD studies. During the initial discharge, the multistep decomposition process involved large structural changes and the formation of by-products like LiCl and $CsLi_2Cl_3$, which do not contribute to capacity in subsequent cycles. As a result, the subsequent discharges (2^{nd} and 6^{th} cycles) show much lower capacity compared to the 1^{st} discharge cycle. The differential capacity (dQ/dV) plots further support this behavior, while the 1^{st} cycle exhibits distinct peaks corresponding to the conversion and alloying steps; these features become less intense and broader in later cycles (Fig. 21b).

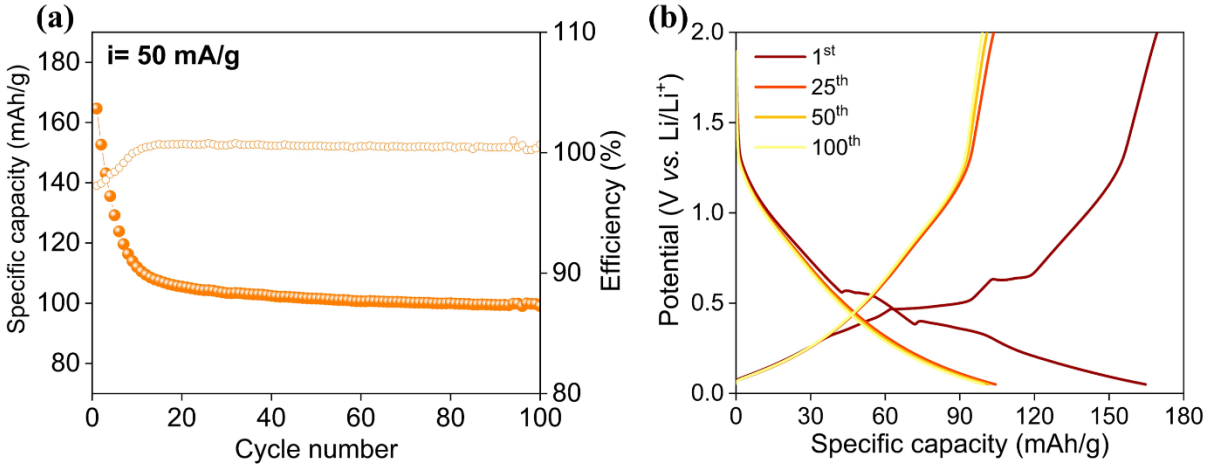

Fig. 22. (a) Related capacity retention and CE during prolonged cycling, up to 100 cycles at 50 mAh/g of $CsPbCl_3$||Li half cells (b) with corresponding galvanostatic charge/discharge profiles.

Fig. 22 shows the long-term performance of $CsPbCl_3$||Li half-cells in over 100 cycles at a constant current density of 50 mA/g. It can be observed that initially, the cell showed a capacity

of ~ 160 mAh/g. However, the cell experiences a quick drop in capacity during the early cycles, eventually stabilizing at about 110 mAh/g. After the stabilization of SEI, the system maintains its capacity at around 110 mAh/g throughout the cycling process. The rate capability of the $CsPbCl_3$ electrode was also evaluated by cycling at progressively increasing current densities from 10 to 200 mA/g (Fig. 23a). At the lowest current of 10 mAh/g, the electrode delivered an initial capacity close to 180 mAh/g, which gradually decreased with higher rates. Importantly, when the current density was reduced back to 10 mAh/g, the electrode recovered most of its capacity (~110 mAh/g), indicating reasonable structural reversibility and tolerance to fast cycling conditions.

The corresponding charge-discharge curves (Fig. 23b) show the expected polarization increase with higher current densities. These results suggest that while the conversion-alloying reaction in $CsPbCl_3$ is sensitive to current density, the electrode shows partial recovery of capacity when returned to lower current conditions.

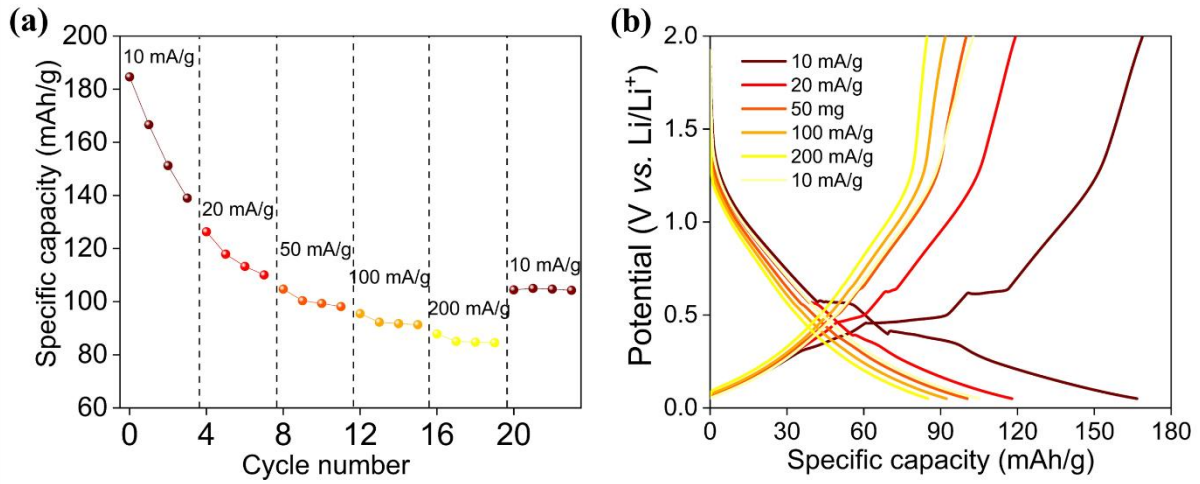

Fig. 23. (a) Rate capability and (b) corresponding charge-discharge profiles of $CsPbCl_3$||Li half cells at different current densities.

3.1.4. Structural Evolution of $CsPbCl_3$

To gain further insight into the long-term structural evolution of $CsPbCl_3$ during cycling, *ex-situ* XRD and XPS measurements were performed after 30 cycles. The combined results clearly demonstrate the conversion of $CsPbCl_3$ during cycling (Fig. 24). Before cycling, the Pb 4f spectrum shows only the sharp doublet characteristic of Pb^{2+} in the well-ordered perovskite lattice. After the first discharge, as discussed previously, XRD revealed the disappearance of $CsPbCl_3$ reflections and the appearance of minor $CsLi_2Cl_3$, along with Pb^0 and Li_xPb_y alloy phases. In agreement, XPS shows the growth of a new low BE Pb 4f doublet corresponding to metallic Pb^0/Li_xPb_y alloys, while the original Pb^{2+} doublet becomes broader.

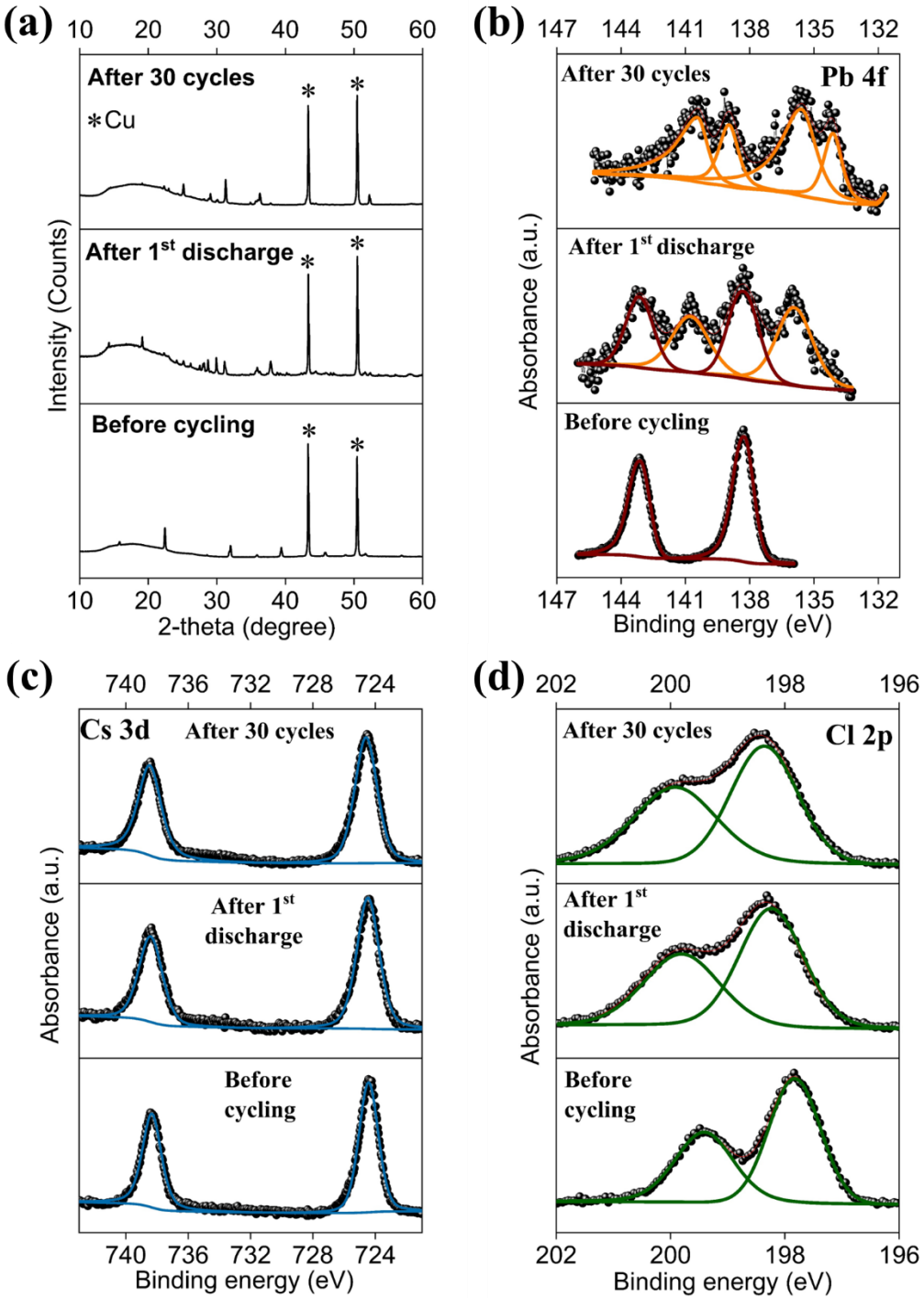

Fig. 24. (a) *Ex-situ* XRD pattern and (b-d) *ex-situ* XPS of $CsPbCl_3$ anode before cycling, after 1st discharge, and after 30 cycles.

By the 30th cycle XRD (Fig. 24a) shows the almost loss of crystalline $CsLi_2Cl_3$, leaving mainly Pb^0 and stable Li_xPb_y alloys, and the XPS (Fig. 24b) likewise shows a spectrum dominated by the metallic/alloyed Pb component. Furthermore, no detectable BE shift in Cs 3d is observed (Fig. 24c), which suggests that Cs largely remains in the monovalent state even after 30 cycles. Although $CsPbCl_3$ is consumed after the first discharge, Cs is redistributed into secondary

phases such as $CsLi_2Cl_3$ or amorphous CsCl, where the chemical environment of Cs^+ does not shift significantly compared to the perovskite. In contrast, the Cl 2p BE (Fig. 24d) peaks exhibited a shift toward higher BE after the first discharge, which remained consistent after 30 cycles. This shift suggests significant interfacial interactions between decomposition products ($CsLi_2Cl_3$, LiCl) and the organic components of the electrolyte (FEC: DEC). Together, these results can show that the perovskite undergoes an irreversible conversion reaction on the first discharge, forming transient Cs-Li-Cl phases and metallic Pb, and with extended cycling, the

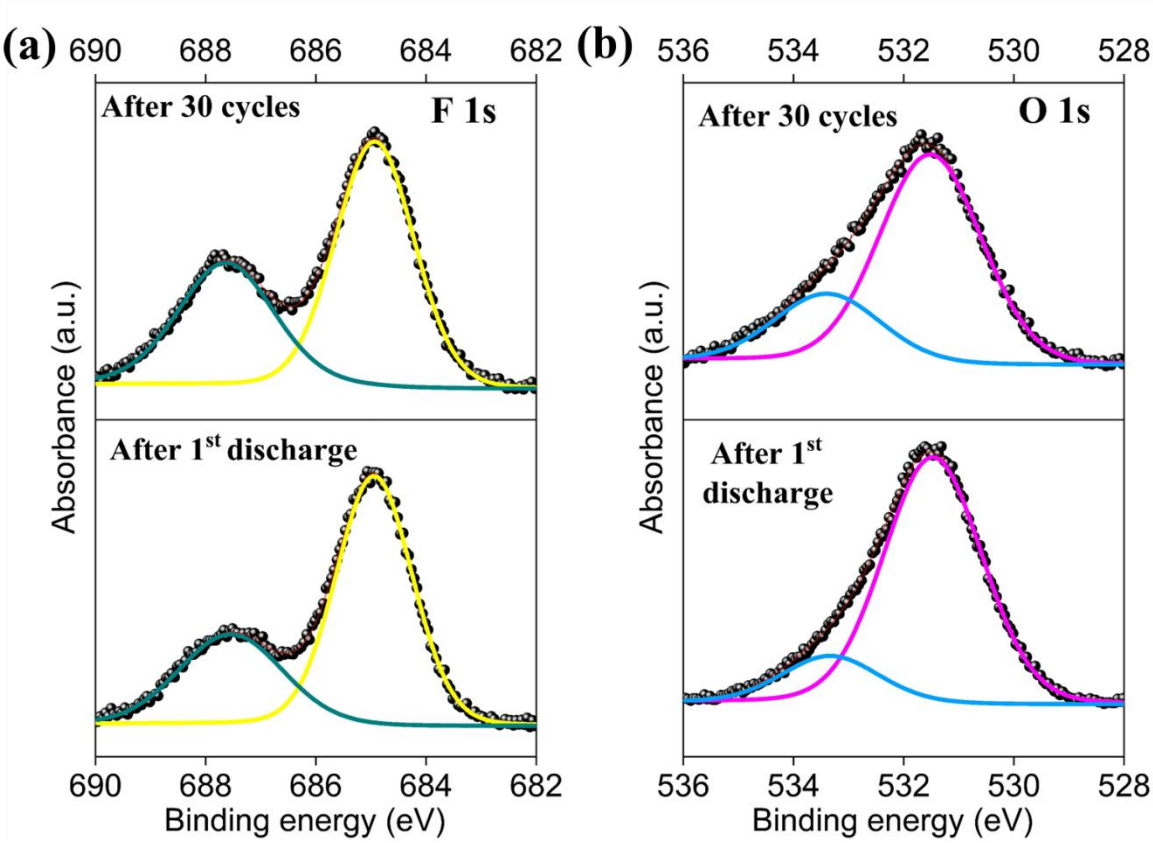

Fig. 25. *Ex-situ* XPS of $CsPbCl_3$ after 1st discharge and 30 cycles (a) F 1s and (b) O 1s

system stabilizes into a mixture of Pb metal and Li_xPb_y alloys. The F 1s and O 1s spectra (Fig. 25) give useful hints about how the electrolyte contributes to the surface chemistry during cycling. In the F 1s region (Fig. 25a), a strong contribution near ~ 685 eV appears after the 1st discharge and remains after extended cycling, which is commonly linked to LiF. A higher BE feature is also present, likely related to organic fluorides. With further cycling, the LiF signal seems to remain dominant while the higher BE component persists. The O 1s spectra (Fig. 25b) show peaks at 531.5 eV and 533.6 eV, corresponding to carbonyl (–C=O) and alkoxy (–C–O) groups, respectively. After 30 cycles, this higher BE component becomes more pronounced, pointing to an accumulation of oxygen-containing products. Taken together, these results

suggest that the electrode surface gradually develops a mixed SEI that is both fluorine- and oxygen-rich, likely containing LiF and organic/polymeric residues, although the exact composition is complex and may evolve with further cycling, therefore requires further testing. Moreover, the morphological changes are shown in Fig. S2 and Fig. S3

3.1.5. Conclusion and Future Perspectives

In this study, $CsPbCl_3$ was investigated as a conversion-alloying anode material for LIBs. Electrochemical, XRD, and XPS analyses consistently showed that $CsPbCl_3$ undergoes an irreversible conversion during the first discharge, producing metallic Pb, Li-Pb alloys, and Cs/Cl-containing salts. After extended cycling, the electrochemical activity was mainly governed by reversible Pb alloying/dealloying, while the inactive salts and continuous SEI growth contributed to capacity fading and reduced stability.

Looking ahead, the results highlight both the promise and the challenges of halide perovskites as anode materials. Future improvements may involve nanostructuring of the perovskite material or compositing with carbon and PVDF to accommodate volume changes and improve conductivity, as well as electrolyte engineering to limit excessive decomposition and stabilize the SEI. The interaction between the electrolyte salt and the perovskite should also be studied to gain a deeper understanding of the SEI composition and evolution over time. While $CsPbCl_3$ in its current form faces limitations for capacity decay after 1^{st} discharge, this work provides a valuable mechanistic view and provides insights for further development of halide-based anode materials.

3.2. $CsPbCl_3$-based ASEI for Li-anode protection

3.2.1. Optimization of $CsPbCl_3$ perovskite powder synthesized via solution-based method

The structural, elemental, and morphological characteristics of the synthesized $CsPbCl_3$ perovskite powder were systematically investigated using XRD, XPS, and SEM. The XRD pattern (Fig. 26) exhibited sharp and well-defined diffraction peaks, indicating high crystallinity of the sample. Detailed analysis confirmed the formation of a pure tetragonal perovskite phase with no detectable secondary phases or impurities. Phase purity and crystal structure were further validated through full-profile Rietveld refinement using the P4mm space group. The calculated lattice parameters for the $CsPbCl_3$ structure are a = 5.596 Å, b = 5.596 Å, and c =

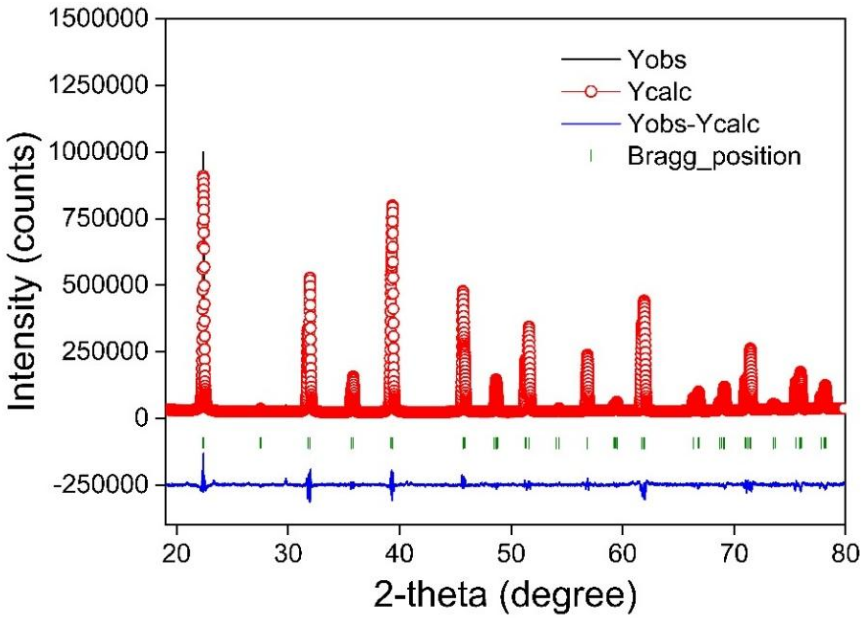

Fig. 26. XRD pattern (solid black line, Yobs) for $CsPbCl_3$ powder. Refinement analysis (red dotted line, Ycalc) by the Rietveld method using the profile fitting FullProf Suite program. The horizontal (blue solid line) represents the residual, and the vertical lines (green solid lines) are the Bragg positions.

5.630 Å. To analyse the chemical composition of the material, XPS was performed (Fig. 27). The survey and high-resolution spectra confirmed the presence of the key elements Cs, Pb, and Cl with characteristic BEs consistent with literature values for $CsPbCl_3$ perovskite.[115] Additionally, trace amounts of sodium (Na), oxygen (O), and residual sulfur (S) were detected, likely originating from the precursors. Morphological analysis using SEM-EDX (Fig. 28) revealed the formation of well-defined, uniformly distributed cubic-shaped $CsPbCl_3$ crystals, with an average particle size of approximately 170 nm.

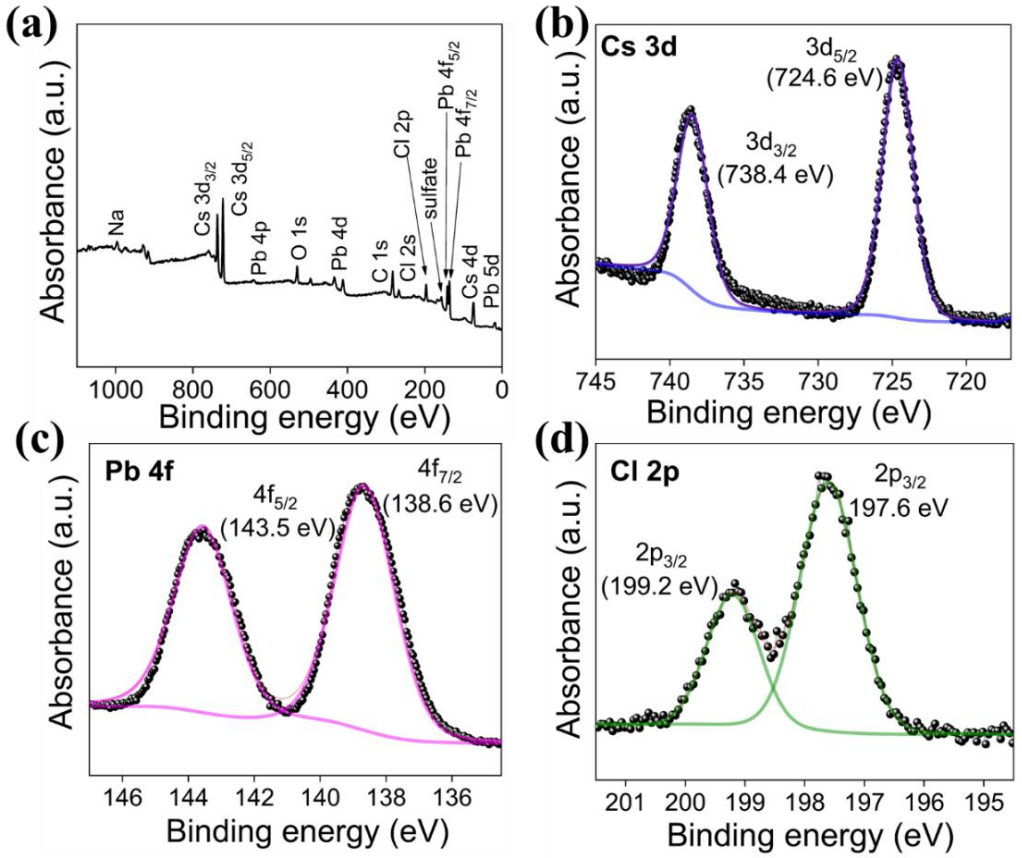

Fig. 27. (a) Survey XPS spectra and high-resolution XPS spectra of the $CsPbCl_3$ powder (a) Cs 3d, (b) Pb 4f, and (c) Cl 2p peak positions.

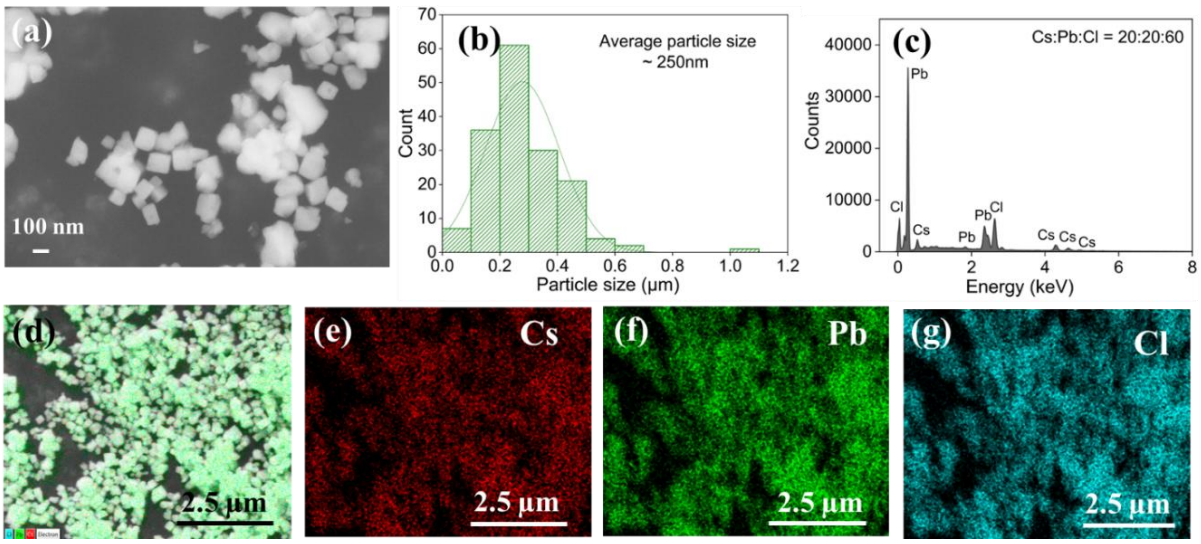

Fig. 28. (a) SEM images of $CsPbCl_3$ powder, (b) average particle size (c) EDX spectra of $CsPbCl_3$ powder. (d-g) EDX elemental mapping of Cs, Pb, and Cl of single halide $CsPbCl_3$ perovskite.

3.2.2. Structural, elemental, and morphological optimization of $CsPbCl_3$-based ASEI

The optimal $CsPbCl_3$ perovskite loading for surface coating was determined by conducting the galvanostatic cycling test using Li||Li symmetric cells, as shown in Fig. 29. Coatings with three different areal loadings, 1 mg/cm^2, 2 mg/cm^2, and 4 mg/cm^2, were evaluated. Among these, the 2 mg/cm^2 loading exhibited the lowest overpotentials, which were maintained for 200 hours of extended cycling as compared to the other two loadings.

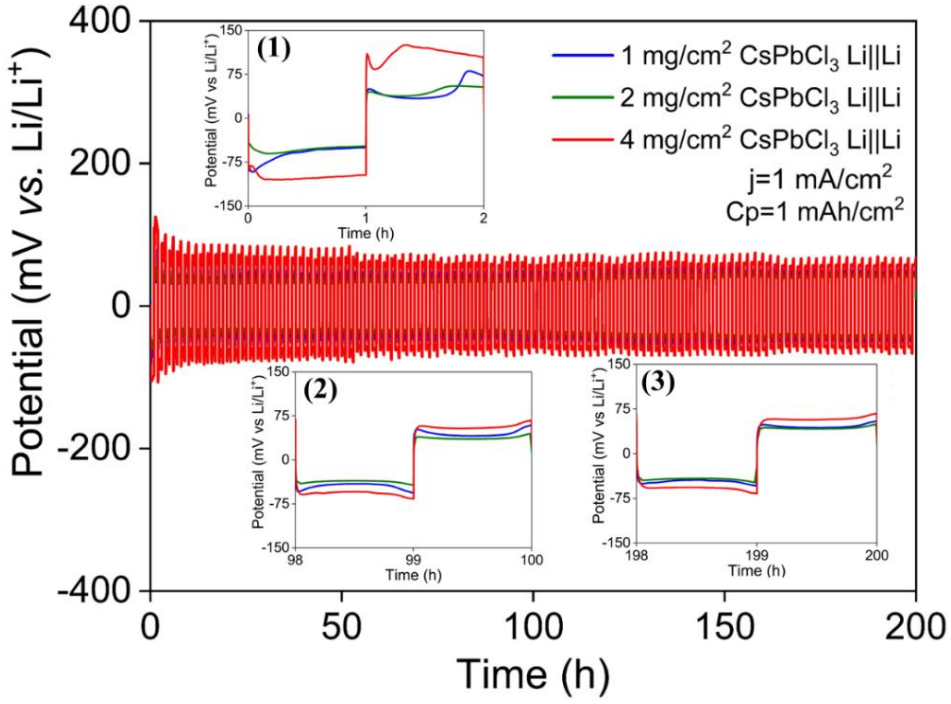

Fig. 29. Optimization of $CsPbCl_3$ perovskite content evaluated by galvanostatic cycling in Li||Li symmetric cell.

Based on these results, a $CsPbCl_3$ loading of 2 mg/cm^2 was selected for subsequent electrochemical testing. The morphology of pristine and $CsPbCl_3$-coated Li was analysed by SEM (Fig. 30). The surface image of the coated Li-metal shows a uniform distribution of $CsPbCl_3$ cubes across the Li-metal surface (Fig. 30 b-c). The thickness of the protective layer was determined to be 5 μm (Fig. 30d). Moreover, EDX mapping (Fig. 30e-g) confirmed the homogeneous distribution of Cl, Cs, and Pb elements within the $CsPbCl_3$ coating on the Li-metal surface.

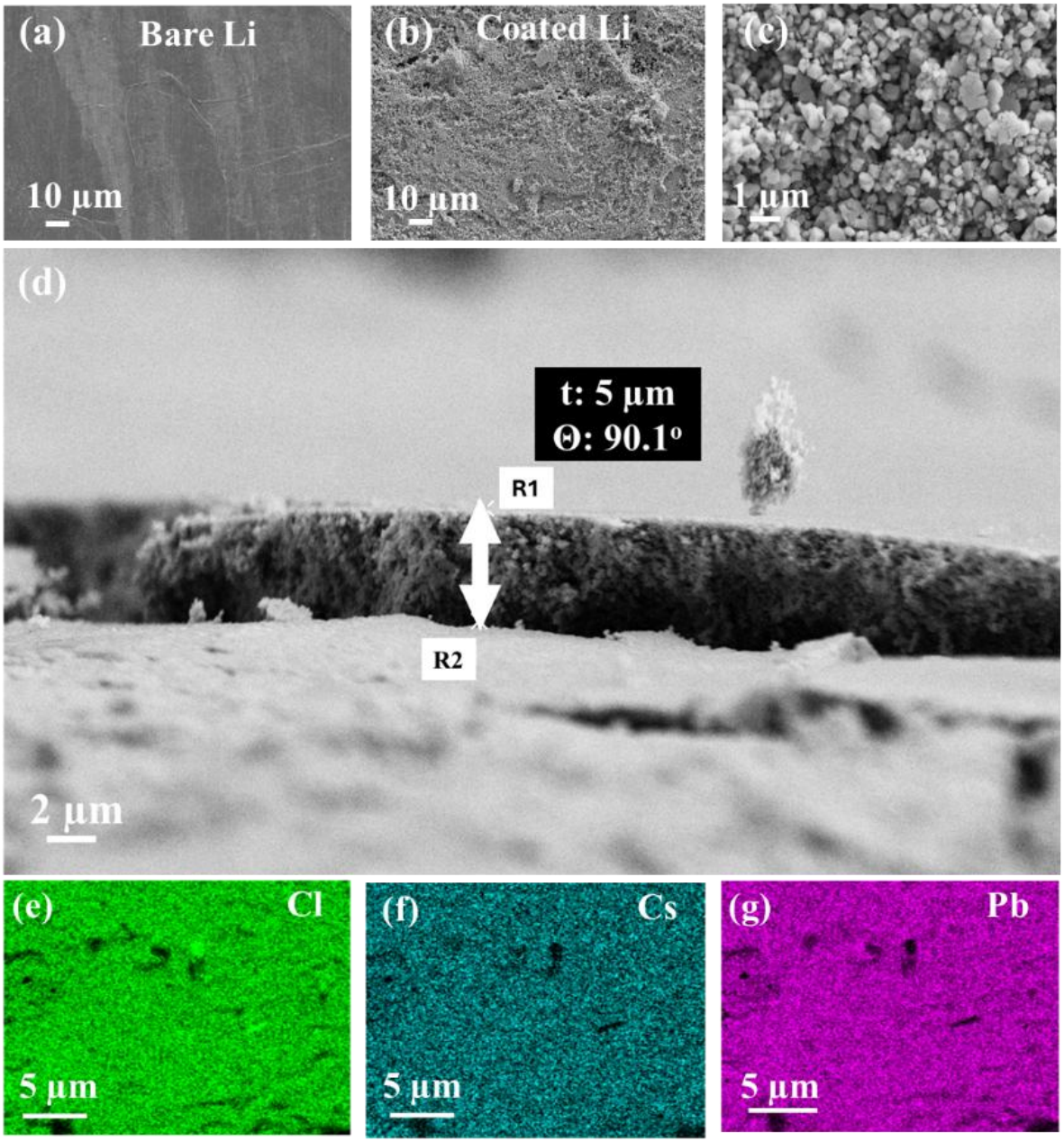

Fig. 30. SEM images of (a) bare Li-metal, (b) and (c) coated Li-metal with 2 mg cm^{-2} $CsPbCl_3$ (d) cross section of coating applied on Li-metal. (d) EDX mapping of coated Li showing the elemental distribution of (e) Cl, (f) Cs, and (g) Pb.

To have a better understanding of the chemical composition and chemical state of each element in the perovskite coating on Li-metal, XPS measurements were conducted. The survey XPS spectrum is given in Fig. 31a. Coating chemistry is identical to powder $CsPbCl_3$, with the constituent Cs, Pb, Cl, S, Na, and O elements present. S, Na, and O peaks come from SDS (used during the $CsPbCl_3$ synthesis). The XPS BEs of the characteristic Cs, Pb, and Cl peaks of coated Li are presented in Fig. 31b-d. Two peaks centered at 738.2 and 724.3 eV are the $3d_{3/2}$ and $3d_{5/2}$ bands of Cs, respectively. The Pb $4f_{5/2}$ and Pb $4f_{7/2}$ peaks are respectively located at 143.1 and

138.2 eV. The Cl $2p_{3/2}$ and Cl $2p_{1/3}$ peaks are centered at 199.5 and 197.8 eV, respectively. These binding energies are consistent with those of pristine $CsPbCl_3$ powder (Fig. 27), indicating that no significant chemical changes occurred during the coating process.

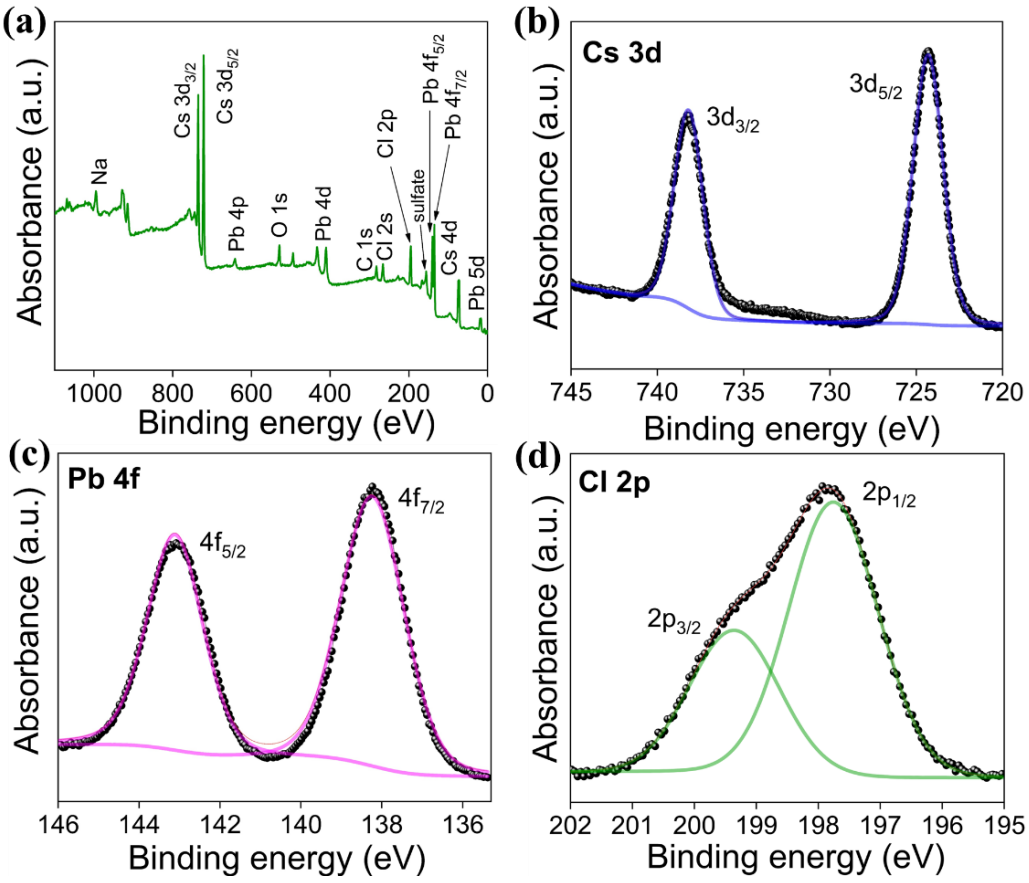

Fig. 31. (a) Survey XPS spectra and high-resolution XPS spectra of the $CsPbCl_3$-coated Li (b) Cs 3d, (c) Pb 4f, and (d) Cl 2p peak positions.

3.2.3. Electrochemical characterization of Li||Li symmetric cells

To evaluate the electrochemical performance of Li-metal electrodes and assess the protective effect of $CsPbCl_3$ coatings in stabilizing the LMA, Li||Li symmetric cells were assembled and tested. Ionic conductivity of the electrolyte was determined to be 4 mS/cm at 25°C by comparison of resistive intercept values with LP40 electrolyte cells, which have a known conductivity of 8 mS/cm at the same temperature. Transference numbers for both bare Li and coated Li cells were determined with three different approaches (Fig. 32), using the equation given below:

$$t = \frac{R_{el}}{R_{el} + R_W} \tag{3}$$

The values for both cells were similar, 0.10 ± 0.03 and 0.09 ± 0.02, respectively, which supports the hypothesis that the coating is porous and conduction happens through electrolyte filling in the pores.

Afterwards, the electrodes underwent continuous plating and stripping with an areal capacity of 1 mAh/cm^2 and a current density of 1 mA/cm^2 per charge/discharge cycle. Following cell

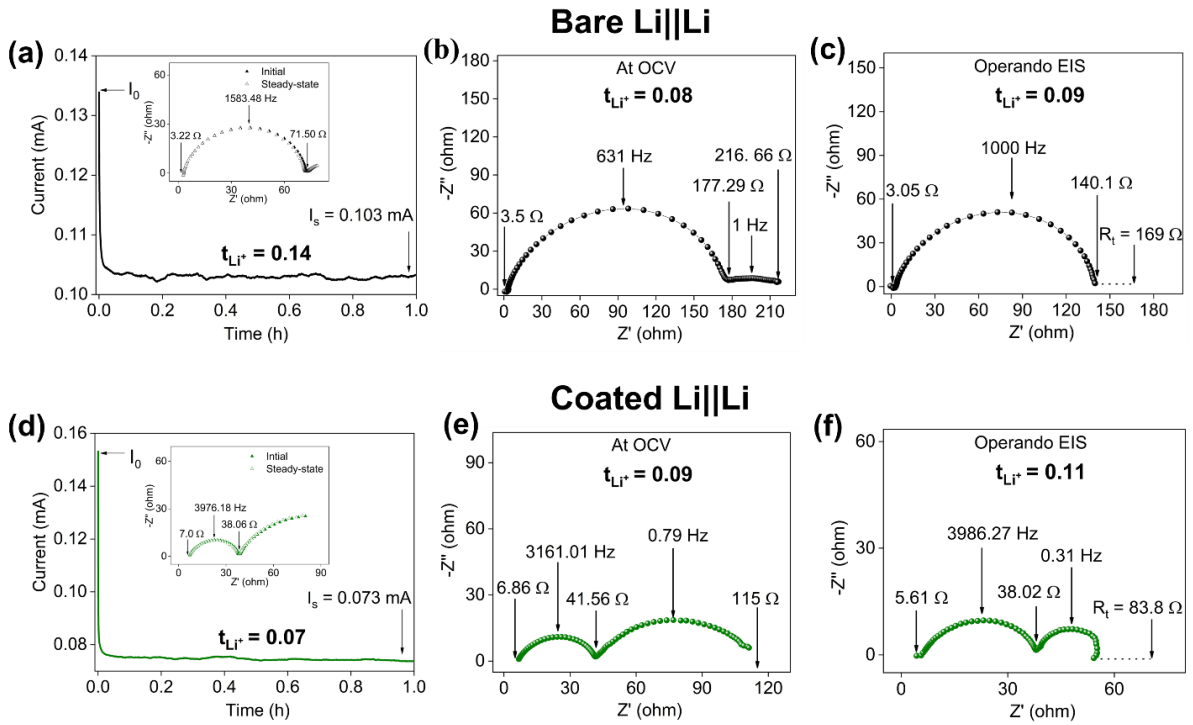

Fig. 32. Transference number determination for bare Li cells (a-c) and coated Li cells (d-f) using the polarisation method, low frequency measurement at open circuit voltage (OCV) and *operando* EIS (left to right).

assembly, the electrodes underwent continuous plating and stripping with an areal capacity of 1 mAh/cm^2 and a current density of 1 mA/cm^2 per charge/discharge cycle (Fig. 33). This approach enabled the monitoring of overpotential variations during cycling, offering insights into mass transport phenomena at the electrolyte/Li-metal interface and facilitating the evaluation of the coating stability.[118] The cell tested with bare Li-metal exhibited an initial overpotential of 140 mV. In contrast, the coated Li cell showed an overpotential of 60 mV. This difference in overpotential is influenced by the initial interfacial resistance, as confirmed by the EIS measurements at OCV presented in Fig. 34. The EIS results indicate that the total resistance

(Rtotal) of the bare Li electrode is significantly higher (~217 Ω), resulting in a larger initial overpotential (~109 mV). In contrast, coated Li exhibited lower impedance (~115 Ω), corresponding to ~58 mV of overpotential. As is evident, most of the difference in total resistance comes from the change in SEI resistance value (174 Ω for bare vs. 35 Ω for coated), while diffusional resistance remains in similar orders of magnitude (50 Ω bare vs. 65 Ω coated). This suggests that the reduced overpotential observed can be attributed to lower interfacial resistance provided by the coating.

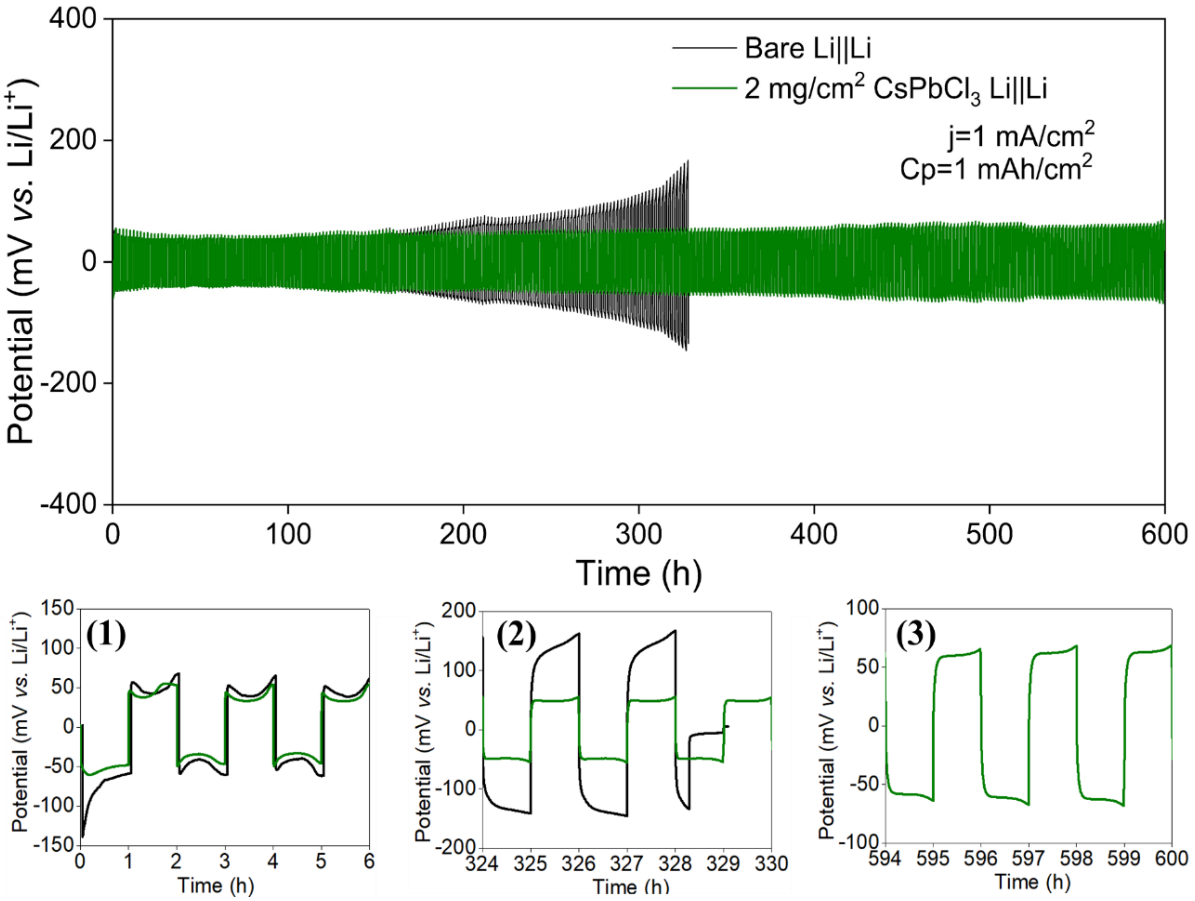

Fig. 33. (a) Galvanostatic cycling of bare and coated Li||Li symmetric cells at areal capacity of 1 mAh/cm^2 with a current density of 1 mAh/cm^2 in 1 M LiFSI in FEC:DEC (1:2) and (b) represents the detailed voltage profiles.

Significant differences appeared between the bare Li||Li cells and coated electrodes over extended cycling. The bare Li||Li symmetric cells showed a noticeable increase in overpotential after 170 h of cycling, and ultimately short-circuiting occurred after 327 h due to the formation of HSAL. In contrast, the $CsPbCl_3$-coated Li||Li cells extended the cycle life of the Li-metal to 600 h with a small increase in overpotential to 80 mV. The extended cycling life and stable performance of the coated Li-metal electrodes demonstrate the protective layer's ability to improve cell stability.

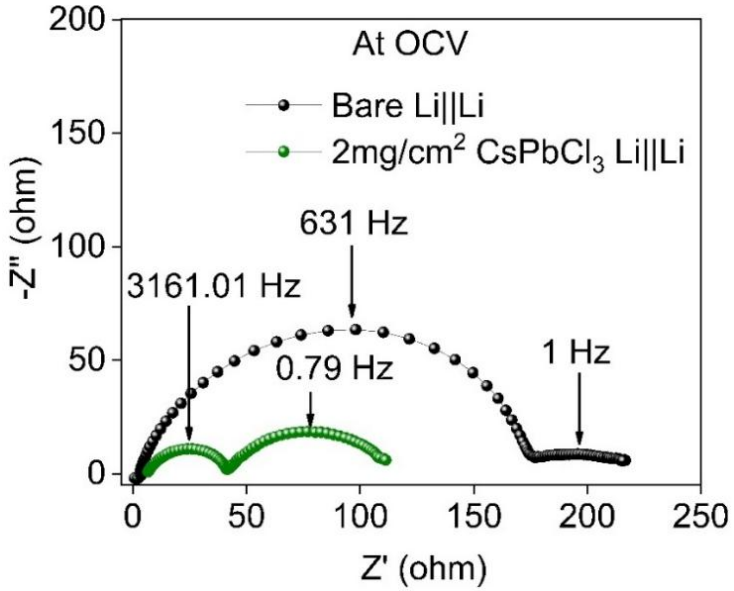

Fig. 34. EIS spectra of bare and coated Li||Li cell at OCV.

Moreover, cycling stability of the coating in Li||Li symmetric cells was also confirmed under higher current density at 2mA/cm^2 and 4mA/cm^2. The Li||Li symmetric cell tests demonstrate that the $CsPbCl_3$ coating improves the electrochemical stability of Li-metal electrodes compared to bare Li. At a current density of 2 mA/cm^2 and areal capacity of 2 mAh/cm^2 (Fig. 35a), the bare Li||Li cell shows a progressive increase in overpotential with pronounced fluctuations over time, indicating unstable Li plating/stripping behavior. While, the $CsPbCl_3$ coated Li||Li cell exhibits a relatively lower overpotential for nearly 200 hours, indicating the ability of the coating to regulate Li deposition. At 4 mA/cm^2 and areal capacity of 4 mAh/cm^2

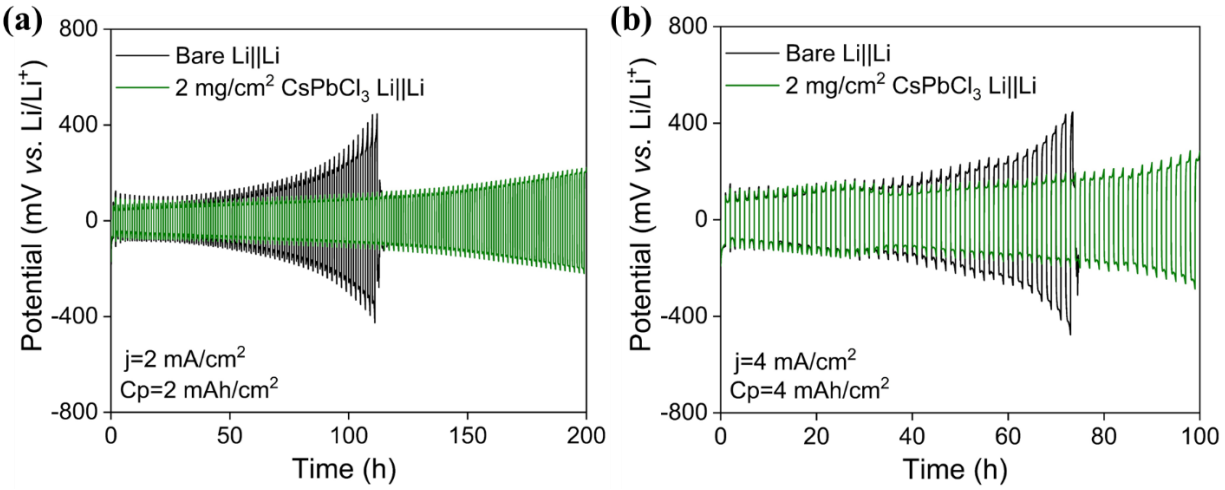

Fig. 35. Galvanostatic cycling of bare and coated Li||Li symmetric cells at (a) a current density of 2 mA/cm^2 & areal capacity of 2 mAh /cm^2 (b) current density of 4 mA/cm^2 & areal capacity of 4 mAh/cm^2.

(Fig. 35b), the bare Li||Li cell fails within ~72 h. Meanwhile, the $CsPbCl_3$-coated Li||Li cell continues to operate for ~ 100 h, however, a gradual increase in overpotential is observed under these harsher conditions. These results demonstrate that the $CsPbCl_3$ coating acts as a protective interface that can promotes uniform Li deposition. However, at higher current densities and capacities, the protection is less effective, suggesting that further optimization of the coating is required. To further investigate the impact of the coating, SEM analysis was performed on the electrode surfaces after 20 cycles. The bare Li electrode displayed a typical porous high surface area structure with significant quantities of mossy Li covering most of the electrode surface (Fig. 36a).

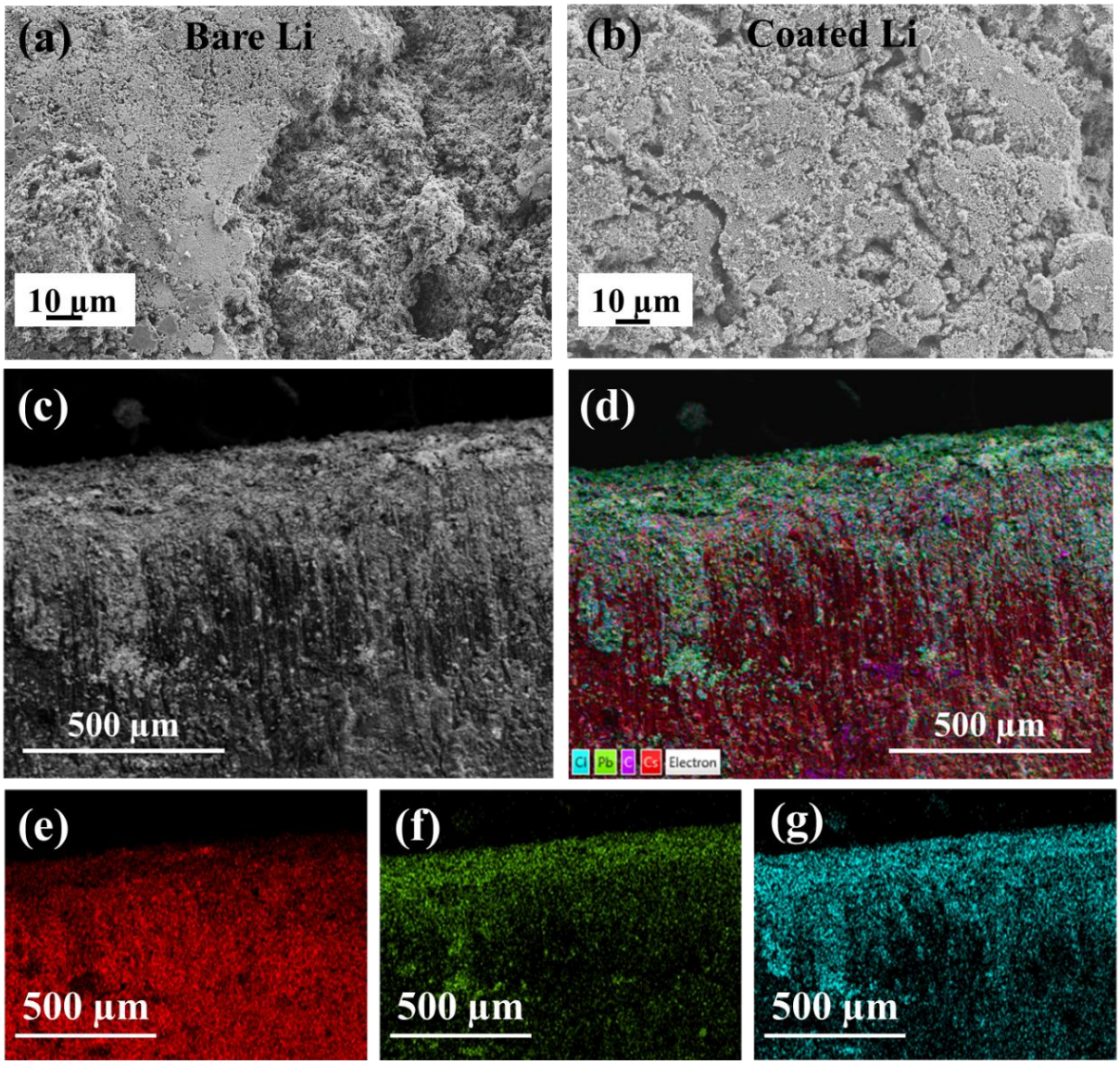

Fig. 36. SEM images of (a) Bare Li-metal and (b) $CsPbCl_3$-coated Li-metal after 20 cycles. (c) Cross-section of $CsPbCl_3$ coating on Li after 20 cycles (d) EDX mapping of coated $CsPbCl_3$ cross-section showing the elemental distribution of (e) Cs, (f) Pb, and (g) Cl.

In contrast, the coated electrode surface was close to pristine coating morphology (Fig. 30b), suggesting close to intact coating (Fig. 36b). The cross-sectional SEM also suggests that the coating remains adhered to the Li surface post-cycling, with no obvious signs of delamination (Fig. 36c). Furthermore, the elemental maps (Fig. 36d-g) show a distinct gradient in the distribution of Cs, Pb, and Cl across the interface. These elements appear more concentrated near the top of the coating and gradually diminish toward the Li bulk. This gradient may indicate partial interdiffusion of the coating components into the Li substrate, although we acknowledge that this could also be influenced by the cross-section preparation method.

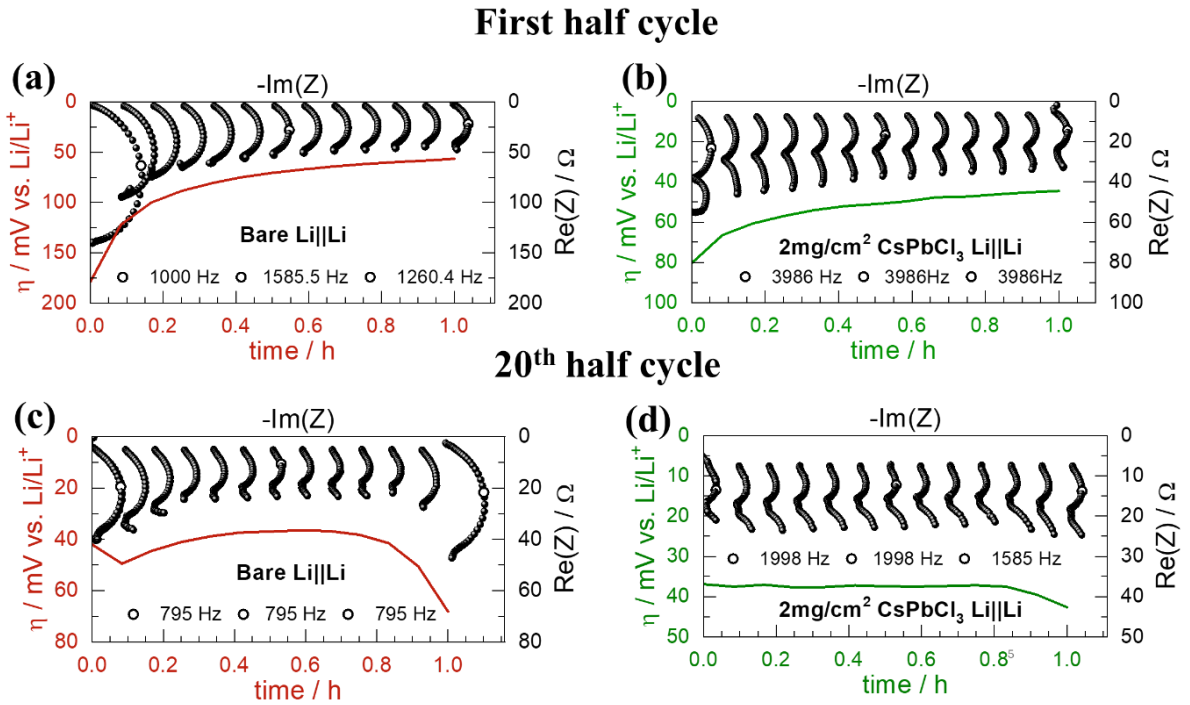

Fig. 37. Operando impedance measurement (black points, scale on top and right) and overpotential (red and green curve, scale on bottom and left). Symbols mark peak frequencies of the 1st, 7th and 13th spectrum. First half cycle (a) bare Li||Li (b) $CsPbCl_3$ coated Li||Li. 20th half cycle (c) Bare Li||Li and (d) $CsPbCl_3$ coated Li||Li.

To explore the factors behind the improved cycling stability of coated Li-metal electrodes, we performed *operando* EIS on symmetric Li||Li cells with bare and coated electrodes. Fig. 37 presents the impedance spectrums as stacked Nyquist plots rotated by 90°, with the low-frequency data points precisely aligned with the simultaneously measured overpotential values (shown in red and green). The arc assignment was done according to a previously published transmission line model for pristine Li and Li with high surface area deposits.[119] The resistance and capacitance of the high-frequency arc measured in both coated and bare Li EIS spectra corresponded well with the model contribution of the migration of Li-ions in the compact SEI

layer. The discussed resistance values were extracted directly from the EIS spectra as the difference in resistance values between the beginning and end of the impedance arc and no fitting was carried out.

The coated Li electrode (Fig. 37b) exhibits a lower initial interfacial resistance (R_{SEI}) of ~32 Ω in the high-frequency region, compared to ~137 Ω for the bare Li electrode (Fig. 37a). Furthermore, R_{SEI} remains relatively stable throughout the first half cycle for the coated electrode, with the final R_{SEI} value of ~ 20 Ω, corresponding to 37.5% reduction. In contrast, the bare Li shows significant variation in the arc size over time, with the final R_{SEI} of ~ 40 Ω, representing 71% decrease from its initial value. This is indicative of high HSAL formation, which contributes to increased interfacial heterogeneity and instability during cycling.

These differences become even more pronounced over extended cycling. By the 20th cycle, *operando* EIS data reveals a substantial increase in overpotential during the second half of the stripping cycle for the bare Li electrode (Fig. 37c), whereas the coated electrode maintains a more stable overpotential profile (Fig. 37d). The rise in overpotential for bare Li is attributed to the progressive consumption of the accessible HSAL deposits. Once these deposits are depleted, Li stripping must proceed from the bulk of the flat electrode, leading to pitting and a plateau in overpotential, as reported in literature.[120]

Overall, *operando* EIS analysis highlights critical differences in interface evolution between bare and $CsPbCl_3$ coated electrodes. In bare Li||Li cells, R_{SEI} exhibited substantial fluctuations of up to ~ 40%, corresponding to ongoing HSAL formation and SEI growth. In contrast, the coated electrodes demonstrated comparatively improved interfacial stability, with R_{SEI} variations limited to ~10%. These findings support the role of the $CsPbCl_3$ coating in suppressing HSAL formation, maintaining a stable electrode/electrolyte interface, and enhancing the cycling performance of Li-metal electrodes.

Ex-situ XPS analysis (after 1st and 20th cycle) was performed to understand the critical insights into the chemical evolution of the $CsPbCl_3$ coating in the bulk during cycling and its role in enhanced interfacial stability observed in *operando* impedance results. Fig. 38a presents the Pb 4f XPS spectrum of $CsPbCl_3$-coated Li electrodes before and after cycling. After the 1st and 20th cycles, the characteristic Pb^{2+} doublet associated with $CsPbCl_3$ exhibits a slight shift toward lower BE, suggesting partial reduction of Pb^{2+} species. Additionally, new peaks emerge at even lower BE values (~141 eV and ~136 eV), corresponding to metallic Pb^0.

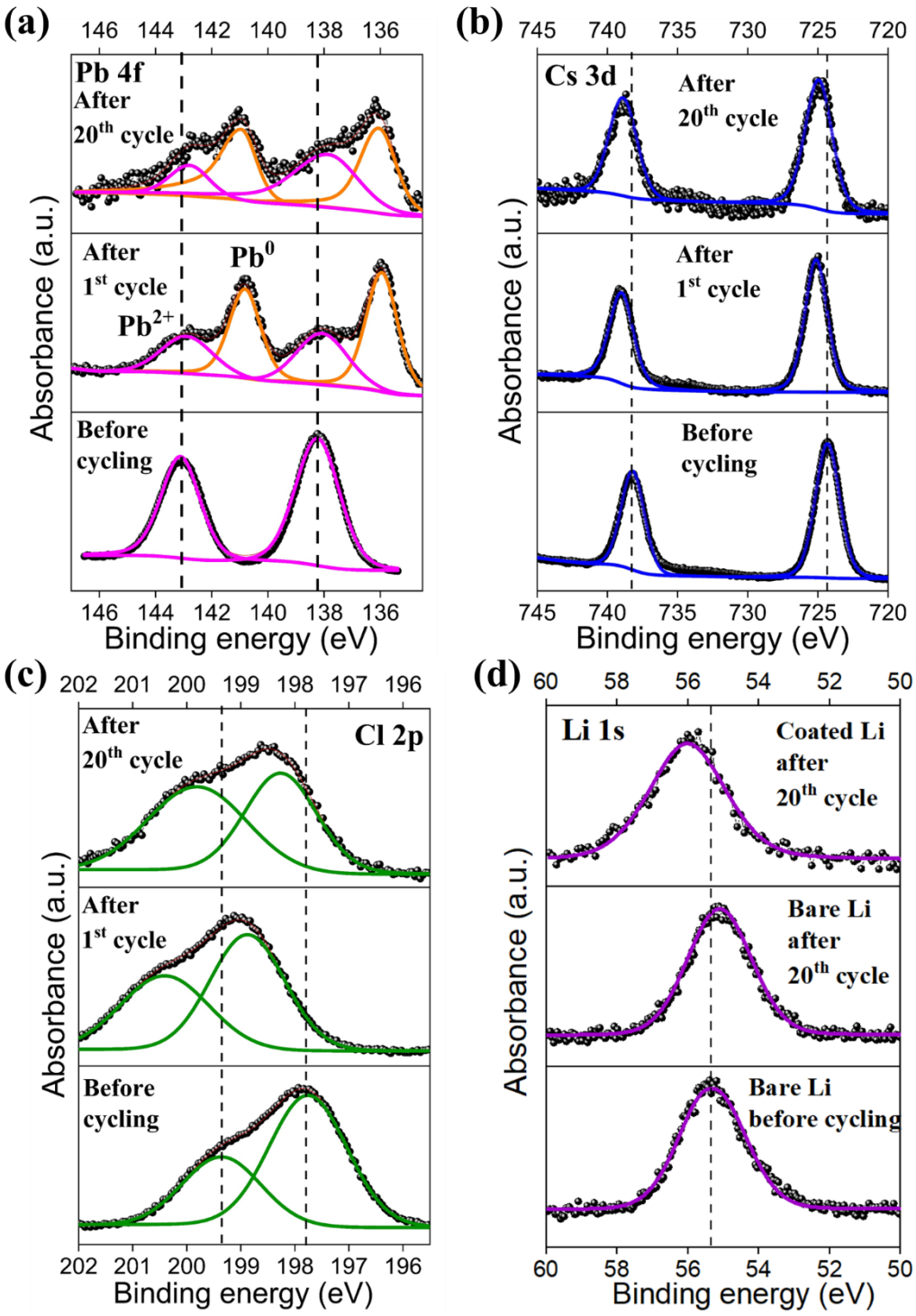

Fig. 38. XPS spectra of the $CsPbCl_3$-coated Li before and after cycling (a) Pb 4f, (b) Cs 3d, (c) Cl 2p, and (d) Li 1s peak positions.

This indicates the formation of Li_xPb_y alloys and Pb at the electrode surface during cycling. These Li-Pb alloys serve as lithophilic nucleation sites, lowering the energy barrier for Li deposition.[120] This observation aligns with the galvanostatic cycling results (Fig. 35) and SEM images (Fig. 36b), where the coated electrode maintains a relatively smooth surface morphology post-cycling, in contrast to the porous, mossy Li growth seen on the bare Li

electrode (Fig. 36a). A minor shift (~0.5 eV) of the Cs 3d peaks (Fig. 38b) toward higher BE was also observed, but this is within the instrumental energy resolution (~0.65 eV) and is considered negligible. Interestingly, EDX cross-sectional mapping (Fig. 36e) shows Cs enrichment near the Li interface rather than on the surface, which may suggest migration of Cs into the inner layers of the coating during cycling. A possible explanation, as hypothesized in

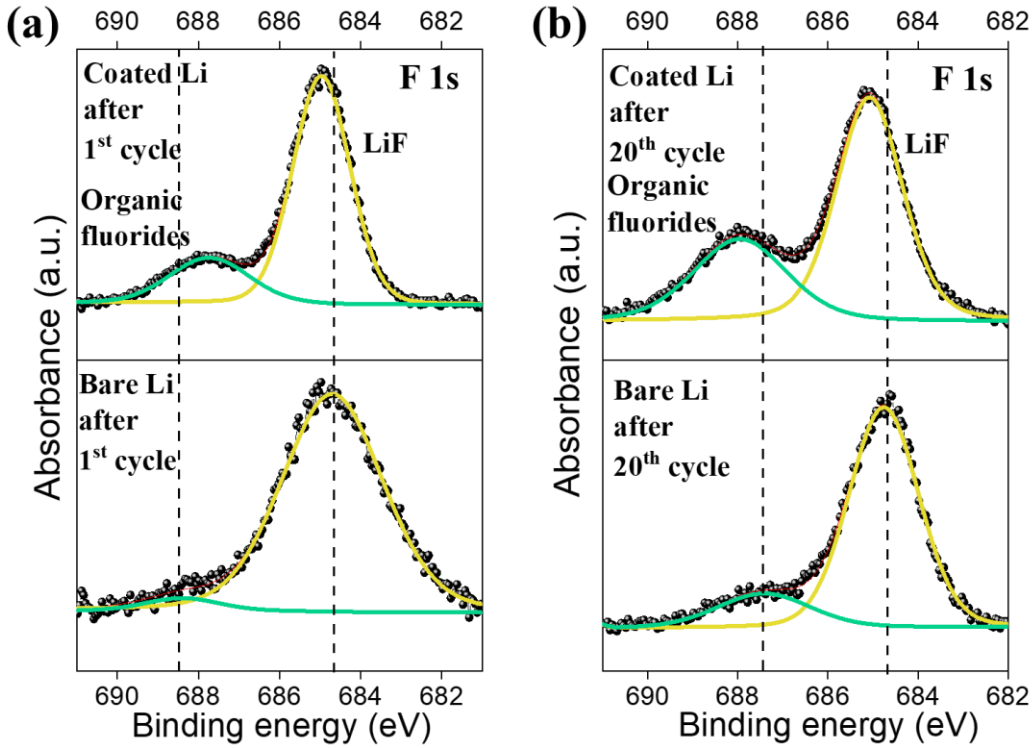

Fig. 39. XPS spectra of the F 1s of $CsPbCl_3$ coated Li and bare Li after cycling (b) 1st cycle (c) 20th cycle.

previous literature,[121] is the transient formation of Cs-containing intermediates (like $CsLi_2Cl_3$ or CsCl) that decompose into Cs^+, contributing to SEI formation. However, we do not have direct evidence for this mechanism at present, and a more detailed study would be required to confirm it. The Cl 2p peaks exhibited an unexpected shift toward higher BE after the 1st cycle, contrary to the typical lower BE expected for LiCl. This shift suggests significant interfacial interactions between decomposition products and the organic components of the electrolyte (FEC: DEC). As shown in Fig. 38c, the higher BE of Cl after the first cycle could result from the coordination of LiCl with polar functional groups such as $–CO_3$ and –O– within the SEI matrix, modifying their electronic environments. After 20 cycles, the Cl 2p peaks shift slightly back toward lower BE, though they remain higher than coated Li before cycling. This may suggest a growing contribution of inorganic LiCl near the surface, likely due to continued perovskite decomposition and the release of Cl^- ions, which then form LiCl domains. Similarly,

the Li 1s spectra (Fig. 38d) show a slight shift (~0.7 eV) toward higher BE, which could be attributed to the coordination of Li^+ with Cl^- or organic species such as Li_2CO_3 or ROLi.

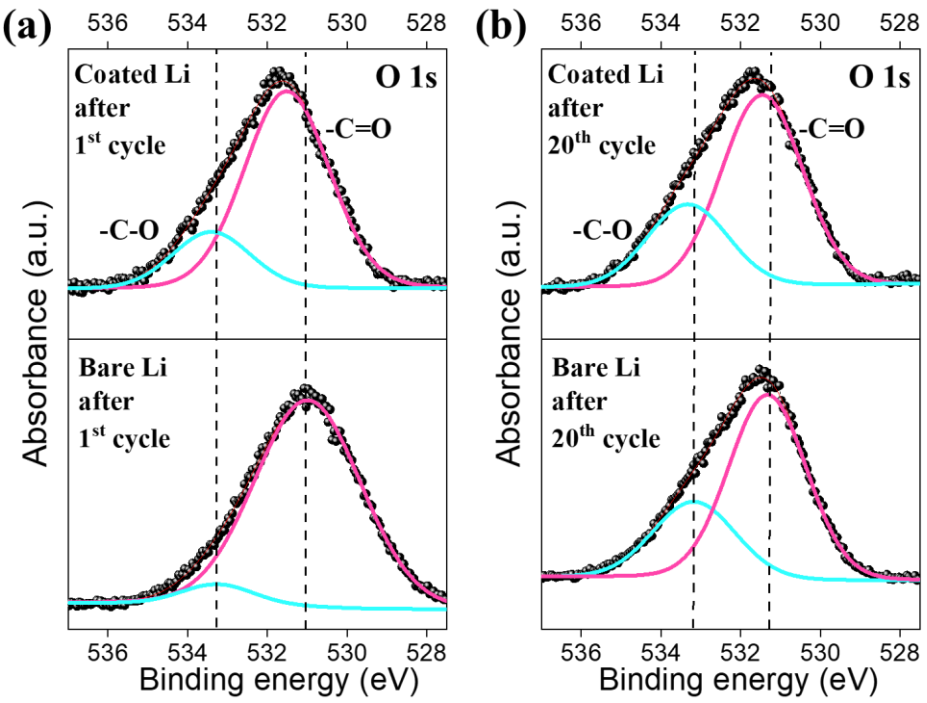

Fig. 40. XPS spectra of the O 1s of $CsPbCl_3$ coated Li and bare Li after cycling (b) 1st cycle (c) 20th cycle.

The F 1s spectra (Fig. 39) consistently display two peaks, LiF (~684.5 eV) and organic fluorides (~688.4 eV) on both bare and coated electrodes after 1 and 20 cycles. The O 1s spectra (Fig. 40) also reveal two dominant peaks at 531.5 eV and 533.6 eV, corresponding to carbonyl (–C=O) and alkoxy (–C–O) groups, respectively. Moreover, the formation of Pb, Li_xPb_y, and LiCl was also confirmed from *ex-situ* XRD as shown in Fig. 41a. For Cs, there is no evidence of potential Cs-based phases detected in XRD. Collectively, these findings suggest that the $CsPbCl_3$ coating undergoes a conversion-type reaction upon cycling, leading to the formation of a hybrid SEI composed of Pb, Li_xPb_y alloys, LiCl, and modified organic/inorganic species (schematic below). This composite SEI offers enhanced ionic conductivity and mechanical robustness, contributing to reduced interfacial resistance and improved cycling stability. However, a full discussion on the SEI evolution requires *operando* XRD and in-depth XPS analysis, which is beyond the scope of this work and will be addressed in a follow-up work.

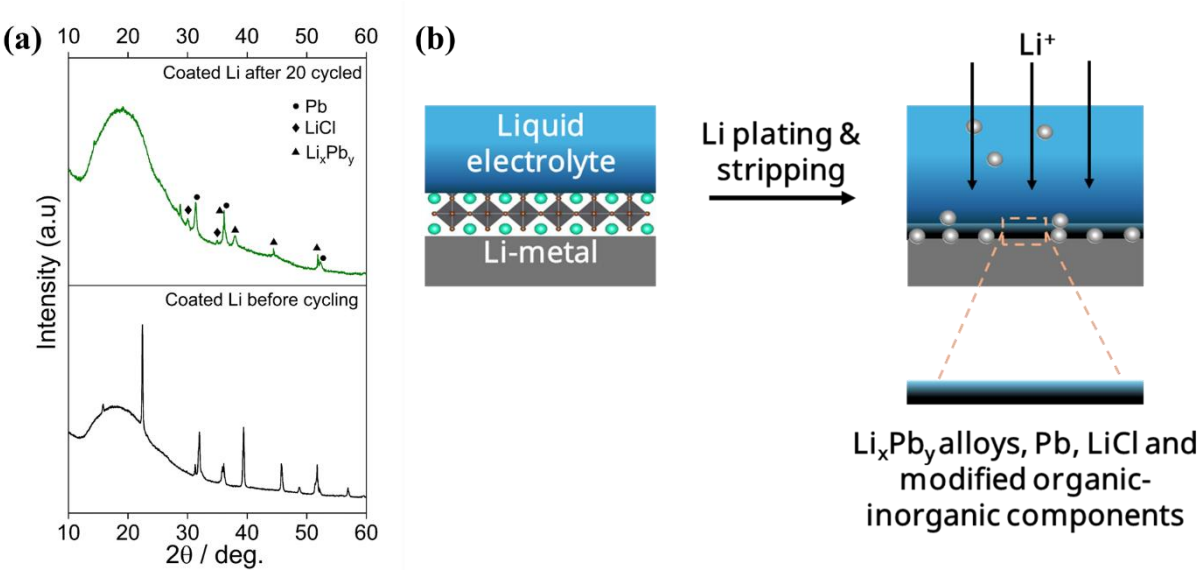

Fig. 41. (a) *Ex-situ* XRD of coated-Li before and after cycling. (b)Schematic illustration of $CsPbCl_3$ ASEI evolution during cycling.

3.2.5. Electrochemical characterization of Li||Cu asymmetric cells

In symmetric Li||Li cells, the unlimited Li reservoir hinders the accurate determination of Coulombic efficiency (CE). To address this limitation, asymmetric Li||Cu cells with a finite Li supply were employed. In this setup, a fixed amount of Li (17.2 µm, corresponding to 4 mAh/cm^2) was initially deposited onto the copper substrate. The cells were then cycled for 10 cycles at 0.5 mAh/cm^2 per cycle (equivalent to 2.16 µm of Li plated and stripped per cycle), before an exhaustive final stripping of Cu at 4 mA/cm^2. This approach allows for precise CE calculation by comparing the total charge from the initial Li reservoir with the charge recovered during the final stripping process. Additionally, a high-capacity single preconditioning cycle was implemented to enhance the copper substrate's stability, thereby reducing passivation effects and mitigating the so-called “ramp-up” phenomenon that can otherwise introduce inaccuracies in CE measurement. Fig. 42 compares the performance of asymmetric Li||Cu cells with bare and coated copper substrates. Initially, the CE of the coated Cu (97.12%) was slightly lower than that of the bare Cu (97.5%), attributed to the initial Li consumption due to the conversion reaction involving the $CsPbCl_3$ coating. To offset this initial Li loss, the number of preconditioning cycles was increased from one to three. Interestingly, while the CE of the bare Cu decreased from 97.5% to 96.1% likely due to HASL formation, the CE of the coated Cu improved from 97.12% to 98%. This enhancement is presumably due to the complete conversion of $CsPbCl_3$ into Pb, Li_xPb_y alloys, LiCl, and modified organic/inorganic interphase

components (as discussed in the previous section), which promote improved Li utilization. Furthermore, similar to the behaviour observed in symmetric cells, a smoother galvanostatic profile with improved kinetics was observed for the coated Cu, which is consistent with the presence of Li_xPb_y alloys.

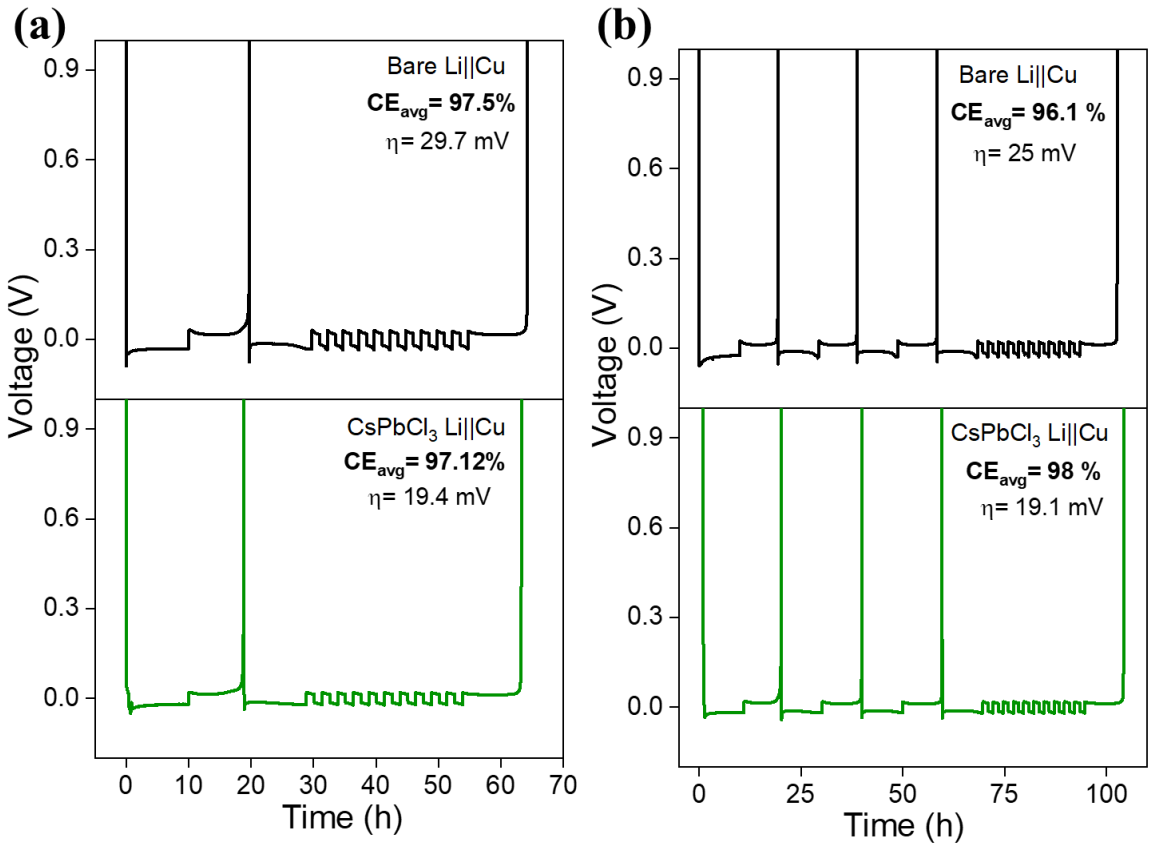

Fig. 42. Utilization tests using the Adams protocol to calculate Coulombic efficiency of bare and $CsPbCl_3$-coated Li||Cu cells (a) one preconditioning cycle and (b) three preconditioning cycles.

We also conducted galvanostatic Li plating and stripping tests at a current density of 0.5 mA/cm^2 and a capacity of 0.5 mAh/cm^2 (Fig. 43). During the initial cycle, the bare Cu||Li cell exhibited a higher CE (~98%) compared to the $CsPbCl_3$-coated Cu||Li cell (~82%). The lower initial CE in the coated system can be attributed to Li consumption during the electrochemical conversion of the perovskite coating, as discussed previously. However, with subsequent cycling, the CE of the coated Cu||Li cell gradually increased to ~92%, indicating the formation of a stable SEI. Furthermore, the bare Cu||Li cell failed after 24 cycles, suggesting the depletion of active Li and loss of electrochemical stability. In contrast, the $CsPbCl_3$-coated Cu||Li cell remained stable up to 80 cycles, demonstrating its effectiveness in improving cycle life. The coated cell maintained an average CE of 89.2%, highlighting the beneficial role of the perovskite coating in enhancing interfacial stability during prolonged cycling. To further assess

the effect of the $CsPbCl_3$ coating on Li deposition behaviour, SEM analysis was performed on the electrode surfaces following 2 hours of Li plating at a current density of 0.5 mA/cm^2. Notable differences in Li morphology were observed between the bare Cu and the coated Cu electrodes. In the bare Cu||Li electrode, Li deposition was markedly non-uniform, featuring dendritic structures and deposits that were randomly distributed. Conversely, the $CsPbCl_3$ coated Cu||Li electrode displayed a relatively uniform Li deposition morphology.

The results obtained in the asymmetric system indicate that the $CsPbCl_3$ coating contributes to improved coulombic efficiency, thereby enhancing the practical feasibility of Li-metal battery applications.

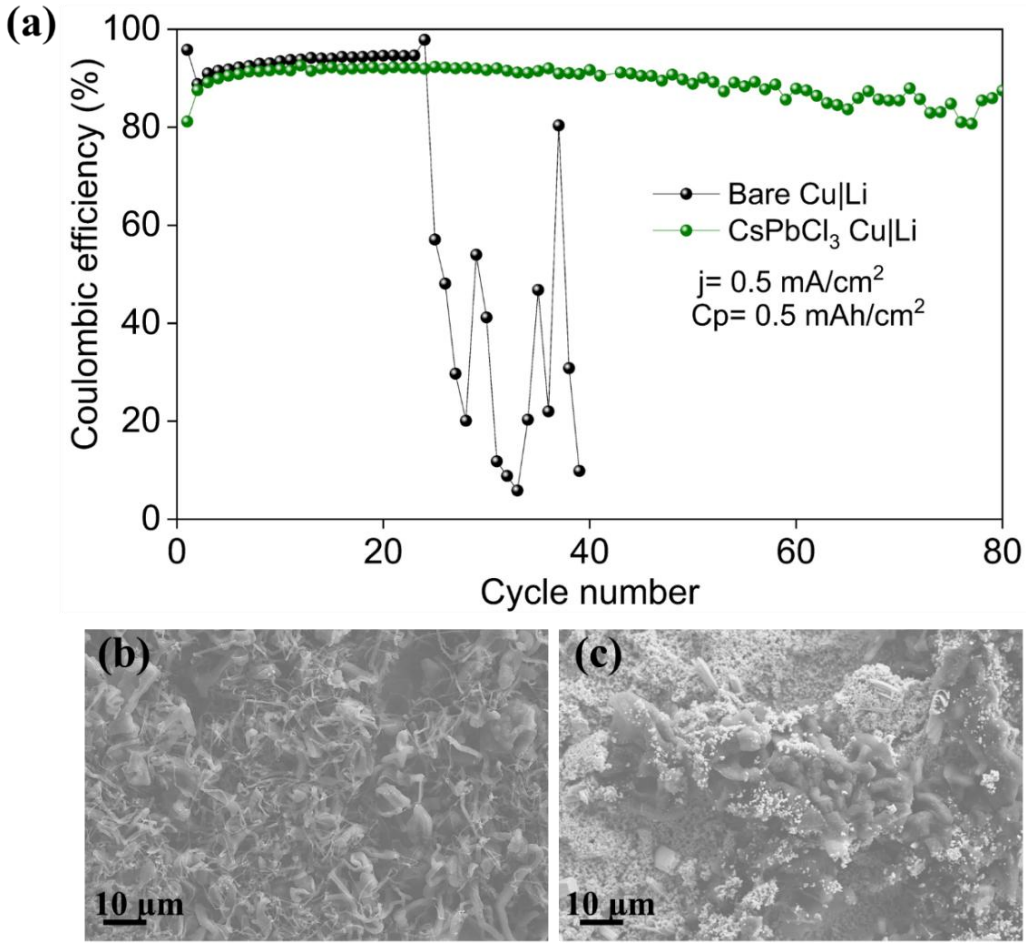

Fig. 43. Coulombic efficiency of bare and $CsPbCl_3$-coated Li||Cu in repeatedly cycling at a fixed capacity of 0.5 mAh/cm^2 with a current density of 0.5 mA/ cm^2. SEM micrographs of (b) bare Cu and (c) $CsPbCl_3$-coated Cu after 2hr of Li deposition.

3.2.6. Electrochemical characterization of Li||LFP full cells

To evaluate the effectiveness of the $CsPbCl_3$ coating, Li||LFP batteries were assembled by pairing bare and $CsPbCl_3$-coated Li-metal anodes with LFP cathodes. The LFP electrodes had active material loadings of 7.6 and 7.5 mg/cm², corresponding to areal capacities of 1.29 and 1.27 mAh/cm², respectively. The CV data (Fig. 44) show that the $CsPbCl_3$-coated cell shows distinct anodic and cathodic peaks but with relatively higher current compared to bare Li, suggesting modified redox kinetics and interfacial dynamics. These differences in current response indicate that the $CsPbCl_3$ coating influences the electrochemical behavior of the full cell. This aligns well with our hypothesis that the $CsPbCl_3$ coating helps form a more robust and chemically distinct SEI likely during the coating process itself rather than relying solely on reactions with the electrolyte.

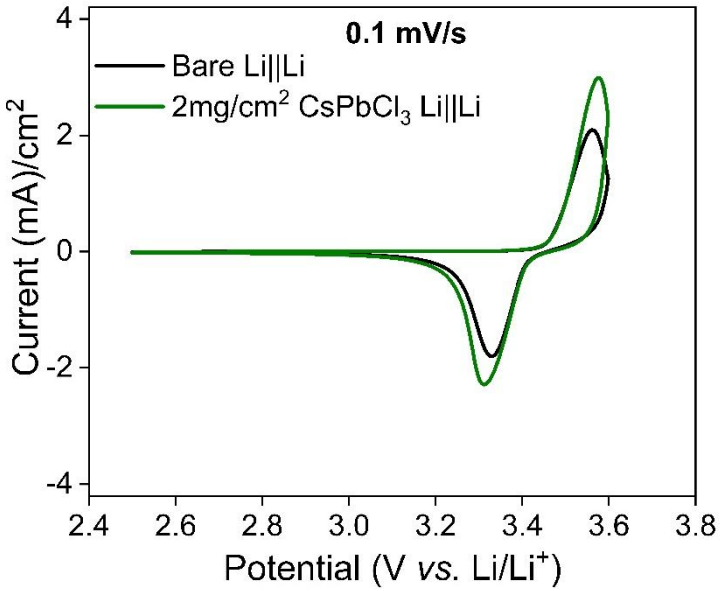

Fig. 44. CV of bare and $CsPbCl_3$ coated Li||LFP full cell.

Furthermore, the cells underwent three initial formation cycles at C/10 before continuous cycling at a 1C rate. During the formation cycles, specific capacities of 145 and 156 mAh/g were achieved for the cells with bare and $CsPbCl_3$-coated Li anodes, corresponding to 85.2% and 91.7% of the theoretical capacity of LFP (170 mAh/g), respectively. Under 1C cycling conditions, the bare Li cell exhibited a specific capacity of approximately 130 mAh/g with notable fluctuations. However, after 150 cycles, the reversible capacity retention dropped sharply to 91.19%, indicating degradation of the LMA. In contrast, the cell featuring the $CsPbCl_3$-coated Li anode demonstrated a stable specific capacity of around 136 mAh/g over 250 cycles (Fig. 45a), keeping a stable reversible capacity retention of 99.46%. Moreover, the

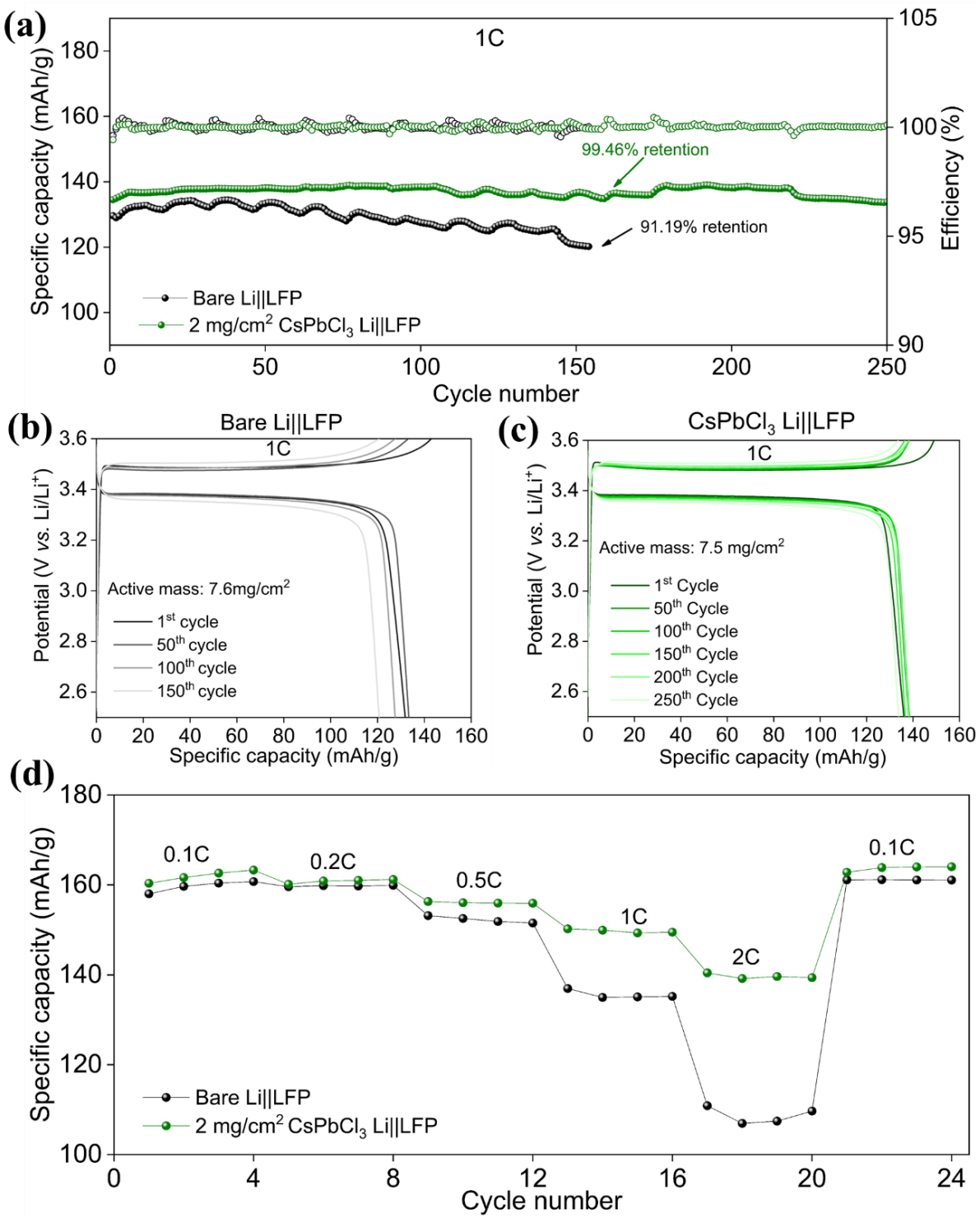

Fig. 45. (a) Related capacity retention and CE during prolonged cycling, up to 250 cycles at 1C. (b) Galvanostatic charge/discharge profiles of Li||LFP battery cells with bare Li anodes, at 1C, and (d) $CsPbCl_3$ coated Li anodes d. Rate capability of Li||LFP cells with bare Li and $CsPbCl_3$ coated Li anodes at different rates from 0.1 to 2C.

performance of the $CsPbCl_3$-coated Li anode battery also shows improved performance compared to that of bare Li. As the current density increases, the $CsPbCl_3$-coated Li|LFP can still deliver high discharge capacities of 163, 161.2, 156.5, 150.2, and 140.3 mAh/g at 0.1, 0.2,

0.5, 1, and 2C (Fig. 45b). Respectively. However, the cell with a bare Li anode displays inferior rate performance; the discharge specific capacities are 160.7, 159.8, 151.55, 135, and 109.5 mAh/g at 0.1, 0.2, 0.5, 1, and 2C, respectively. These results highlight the stabilizing effect of $CsPbCl_3$ coating.

3.2.8. Conclusion and Future Perspective

In this work, we have demonstrated that the $CsPbCl_3$ perovskite enables the formation of a stable Li-metal protective coating that extends the cycle life and mitigates the formation of HSAL. The performance of the coating was tested in both symmetric Li||Li and asymmetric Li||Cu cells to evaluate its stability and CE, respectively. The $CsPbCl_3$-coated Li||Li cells showed a longer and more stable cycle life, with a slower increase in overpotential compared to bare Li at a current density of 1 mA/cm^2 and a capacity of 1 mAh/cm^2. Using the modified Adam's protocol, the coated Li||Cu cells achieved an improved CE of 98%, while the bare Li cells showed a lower CE of 96.1%. *Operando* electrochemical impedance measurements showed that the $CsPbCl_3$ coating helps in suppressing the HSAL formation and maintains a stable electrode/electrolyte interface. XPS results revealed that the $CsPbCl_3$ coating reacts with Li-metal, forming a hybrid SEI made up of Pb, Li_xPb_y alloys, LiCl, and modified organic/inorganic components, which helps in reducing the interfacial resistance and improves cycling stability. In addition, laboratory-scale full cells were assembled using a commercially relevant LFP cathode. The $CsPbCl_3$-coated Li anodes showed improved performance, with 99.46% capacity retention after 250 cycles, compared to 91.19% retention after 150 cycles for bare Li. These results confirm the positive effect of $CsPbCl_3$ coatings in improving the long-term performance of Li-metal batteries. However, to understand the Li-transport mechanism in ASEI, it is essential to perform further characterization techniques such as operando XRD, operando XPS, etc.

3.3. $CsPbCl_3$-based ASEI for graphite and silicon anode protection

3.3.1. Electrochemical performance of coated graphite||Li half cells

To further investigate the effectiveness of the $CsPbCl_3$-based ASEI, we extended our study to other commonly used anode materials, namely graphite and silicon. The motivation for this was twofold. First, graphite is the most widely used commercial anode in LIBs, providing a relevant benchmark to assess whether the protective effect of $CsPbCl_3$ translates to practical electrode systems. Second, silicon is a high-capacity anode material, but it suffers from severe volume expansion and unstable SEI formation during cycling. By testing both graphite and silicon, we aimed to evaluate whether the $CsPbCl_3$ coating could provide interfacial stability not only for Li-metal but also for anodes that undergo different electrochemical processes and degradation mechanisms. The same procedure was followed to produce the coating on the electrodes.

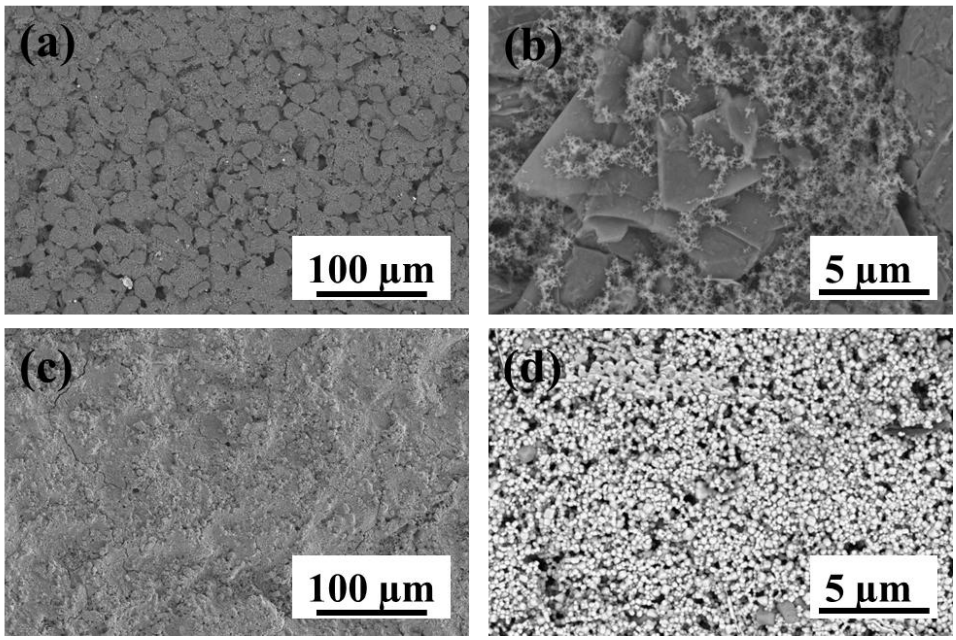

Fig. 46. SEM images of (a) & (b) Pristine graphite and (c) & (d) Coated graphite.

Fig. 46a-b shows the SEM images of pristine graphite, where the flaky morphology typical of graphite particles is clearly visible. Fig. 46c-d shows that the surface is uniformly covered, with the perovskite forming a continuous protective layer across the graphite particles.

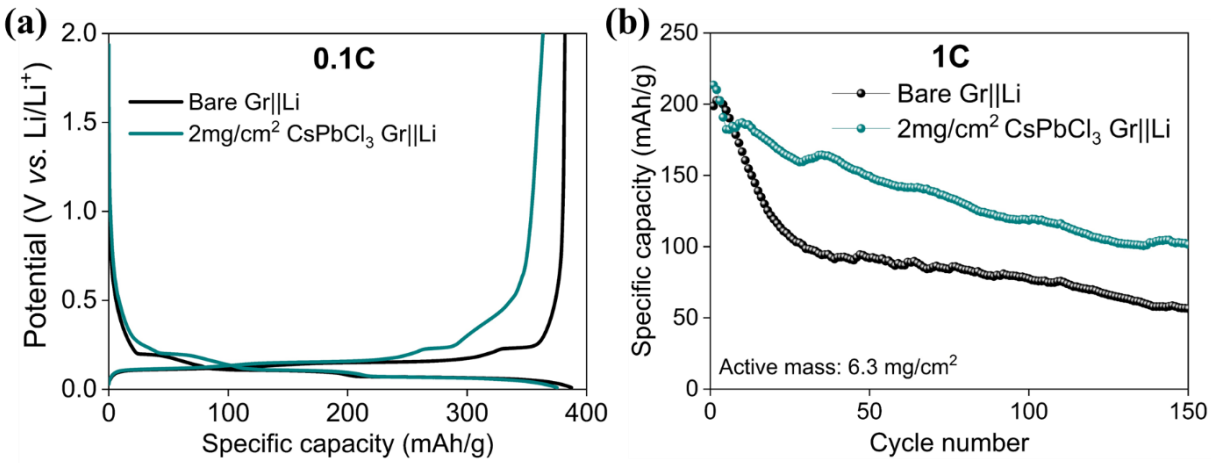

Fig. 47. (a) Galvanostatic charge/discharge profiles at 0.1C and (b) represents the long-term cycling stability of bare and coated graphite cells with bare Li anodes, at 1C.

The electrochemical performance of bare and coated graphite electrodes is compared in Fig. 47. It can be seen that at 1C, the bare graphite electrode suffers from a sharp capacity fade in the initial cycles, retaining less than 50 mAh/g after 150 cycles. In contrast, the $CsPbCl_3$-coated graphite maintains a relatively higher reversible capacity of ~100 mAh/g. However, both the bare and $CsPbCl_3$-coated graphite electrodes exhibit a gradual decline in capacity during cycling. This behavior can be attributed to the use of Li-metal as the counter electrode in half-

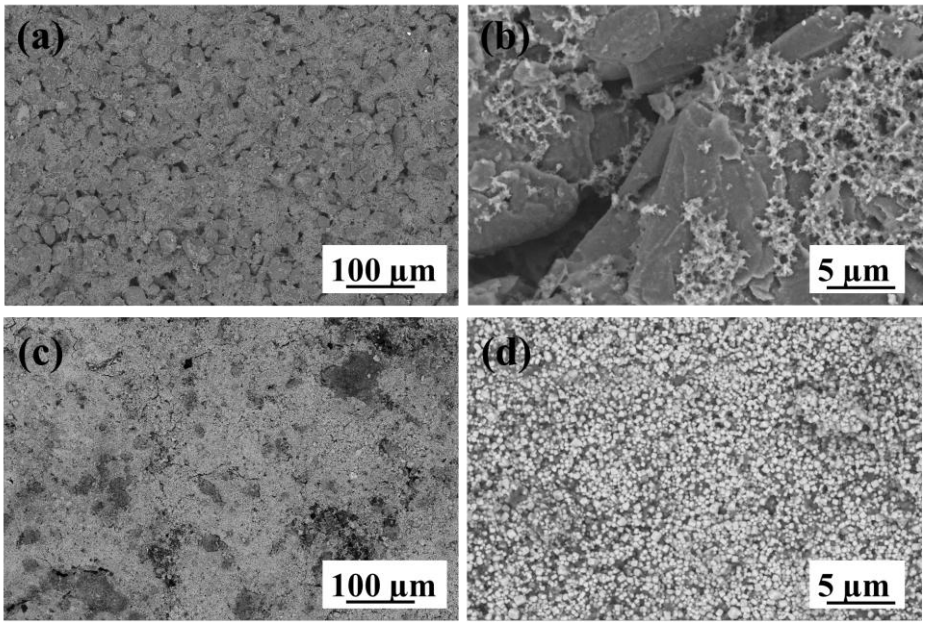

Fig. 48. SEM images of (a) & (b) Pristine graphite and (c) & (d) Coated graphite after 20 cycles.

cell configurations. Due to the continuous parasitic reactions at the Li surface, including electrolyte decomposition, SEI thickening, and dead Li formation lead to an irreversible loss of

active Li. As a result, although the working electrode is stabilized by the $CsPbCl_3$ coating, the overall cell still experiences capacity fading.

The *ex-situ* SEM analysis for the bare graphite electrode (Fig. 48a-b) shows no major visible morphological changes after 20 cycles, which may indicate that the capacity fading observed in the electrochemical profiles is not only due to structural degradation of the graphite itself. In contrast, the $CsPbCl_3$ coating is clearly attached to the graphite electrode surface after cycling, demonstrating its stability under repeated cycling.

3.3.2. Electrochemical performance of coated Si||Li half cells

The protective role of $CsPbCl_3$ ASEI was also evaluated on Si anodes (Fig. 49). As expected, the bare Si electrode displayed severe capacity fading, largely due to the large volume expansion and fracture associated with lithiation/delithiation. The $CsPbCl_3$-coated Si electrode, while still showing gradual capacity decay, maintained a higher reversible capacity over 150 cycles compared to the uncoated counterpart.

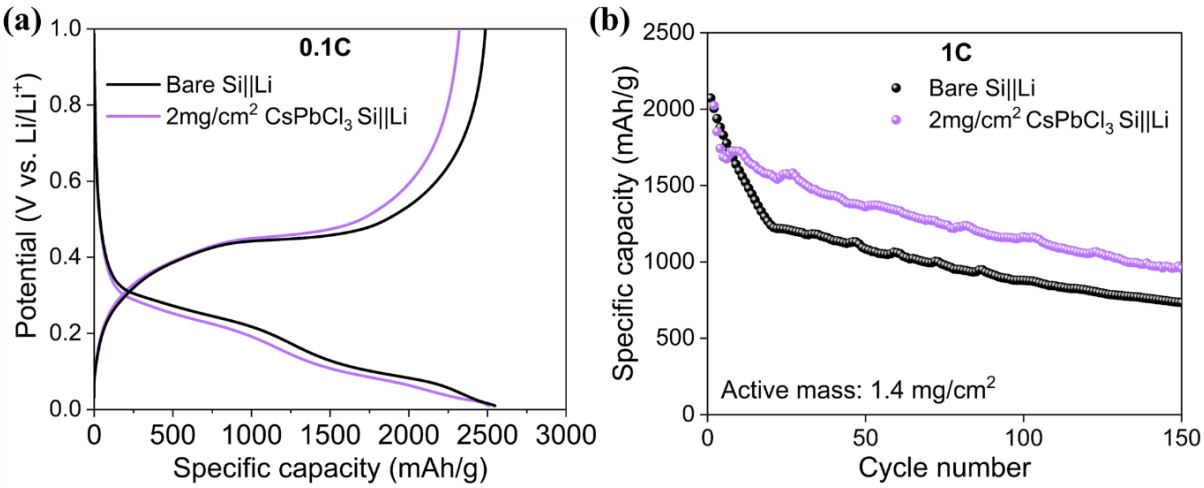

Fig. 49. (a) Galvanostatic charge/discharge profiles at 0.1C and (b) represent the long-term cycling stability of bare and coated Si cells with bare Li anodes, at 1C.

3.3.3. Conclusion and Future Perspective

In conclusion, through electrochemical analysis, it can be seen that $CsPbCl_3$ was successfully demonstrated as an ASEI coating for stabilizing graphite and Si anodes. On graphite, the coating provided a higher reversible capacity and improved retention compared to bare electrodes, while SEM analysis showed that the structural integrity of the coating was preserved even after repeated cycling. Similar results were observed with the Si-anode. The future work should focus

on implementing $CsPbCl_3$-coated graphite and Si in full cells paired with commercial cathodes to validate their long-term performance and practical applicability. Further optimization of the coating thickness and deposition techniques of the perovskite layer may also lead to enhanced interfacial stability and improved Li-ion transport. Moreover, the future study should also focus on the Li-transport mechanism in both systems.. Overall, this study demonstrates the potential of $CsPbCl_3$-based ASEIs as a promising approach to advancing the cycle life and reliability of LIBs.

Supplementary Information

S1. Charge/discharge profile of $CsPbCl_3$-based anode material.

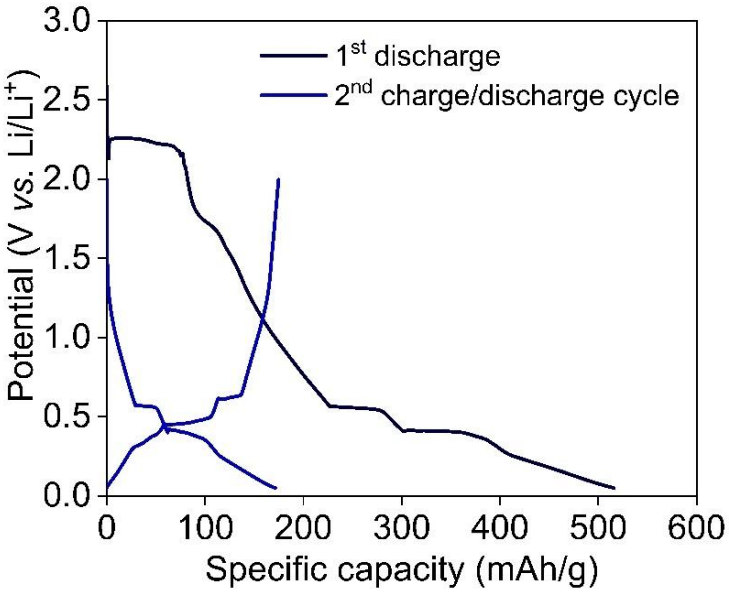

Fig. S1. 1st discharge and 2nd charge/discharge curve of (70:20:10) $CsPbCl_3$ electrode composition in half-cell configuration.

S2. Postmortem SEM of $CsPbCl_3$ anodes

The SEM images and corresponding EDX maps provide further information on the morphological and elemental evolution of $CsPbCl_3$ during cycling. Before cycling, the electrode surface shows well-defined particles with sharp edges (Fig. 18), and the EDX maps indicate that Cs, Pb, and Cl are distributed relatively uniformly, consistent with the intact perovskite phase observed in XRD and the dominant Pb^{2+} signature in XPS (Fig. 19). After the first discharge (Fig. S2), the surface appears more fragmented and roughened, and the EDX maps suggest that the elemental distribution becomes less homogeneous. After 30 cycles (Fig. S3), the morphology becomes even more irregular, with larger agglomerated features. These SEM-EDX results can indicate the breakdown of $CsPbCl_3$ during cycling.

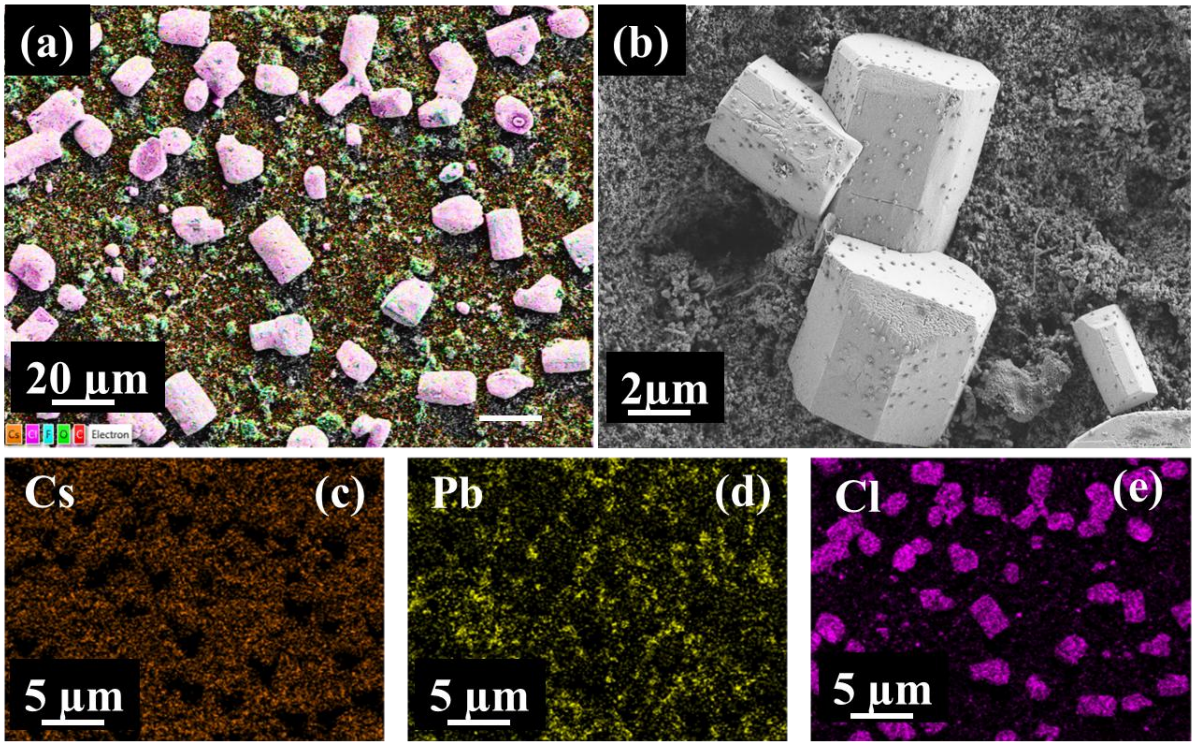

Fig. S2. (a) SEM-EDX images of $CsPbCl_3$ after 1st discharge, (b) magnified view and EDX mapping showing the elemental distribution of (c) Cs, (d) Pb, and (e) Cl.ss

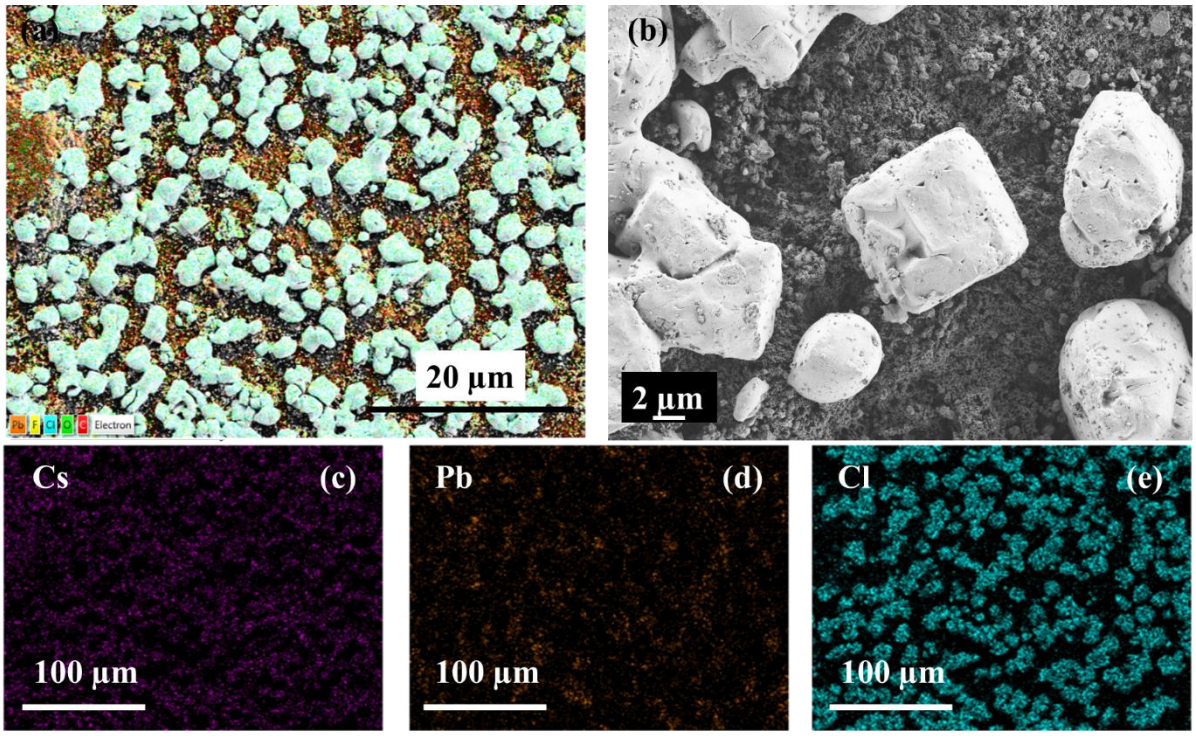

Fig. S3. (a) SEM-EDX images of $CsPbCl_3$ after 30 cycles, (b) magnified view and EDX mapping showing the elemental distribution of (c) Cs, (d) Pb, and (e) Cl.

S3. Electrochemical optimization of mechano-chemically synthesized $CsPbCl_3$-based ASEI

The ASEI on Li-metal was created using the drop casting method. The surface morphology of the $CsPbCl_3$ coating on the Li-metal was examined by using SEM (Fig. S4a). The SEM images show that the coating on the Li-metal surface is relatively continuous, though not uniform. It can also be observed that the perovskite particles are spread across the surface, with some areas showing visible aggregation. The surface features interconnected clusters of particles, along with noticeable voids and gaps in between them.

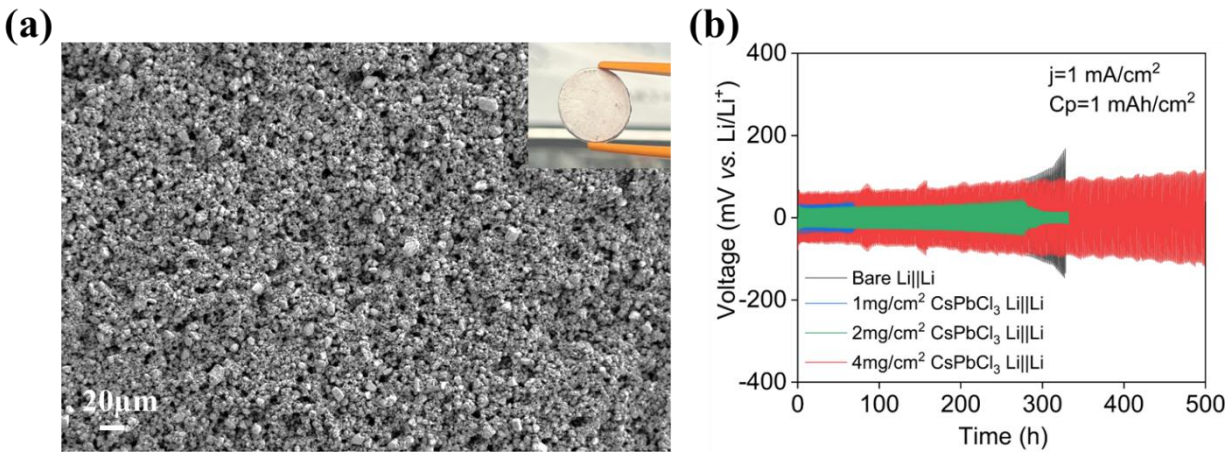

Fig. S4. (a) SEM image of coated $CsPbCl_3$ Li-metal surface. (b) Optimization of $CsPbCl_3$ perovskite content evaluated by galvanostatic cycling in Li||Li symmetric cell.

To determine the optimal $CsPbCl_3$ perovskite content for surface coatings, galvanostatic cycling was performed using Li||Li symmetric cells at an areal capacity of 1 mAh/cm^2 and a current density of 1 mA/cm^2 per charge/discharge cycle, as shown in Fig. S4b. Three different areal loadings, 1 mg/cm^2, 2 mg/cm^2, and 4 mg/cm were evaluated. While the 4 mg/cm^2 coating exhibited the highest overpotential among the three, it also demonstrated the most extended cycling stability. This suggests a trade-off between initial resistance and long-term protection. When comparing the coated Li||Li cell with the bare Li||Li cell, the coated cell initially exhibited a slightly higher overpotential (~60 mV) than the bare cell (~52 mV), likely due to the additional interphase resistance introduced by the protective coating. However, over prolonged cycling, the benefit of the coating became evident. The bare Li||Li cell failed after 327 hours due to short-circuiting, whereas the coated cell remained stable for up to 500 hours, with a final overpotential of approximately 120 mV. To further evaluate the effectiveness of the $CsPbCl_3$ coating, Li||LFP full cells were assembled. These cells underwent three formation cycles at

C/10, followed by continuous cycling at 1C, as shown in Fig. S5a. Initially, the coated Li||LFP cells delivered higher specific capacity compared to the bare cells, maintaining this advantage for up to 100 cycles. However, after 100 cycles, the capacity of the coated cells declined significantly, eventually reaching a level comparable to the bare cells. This degradation is likely

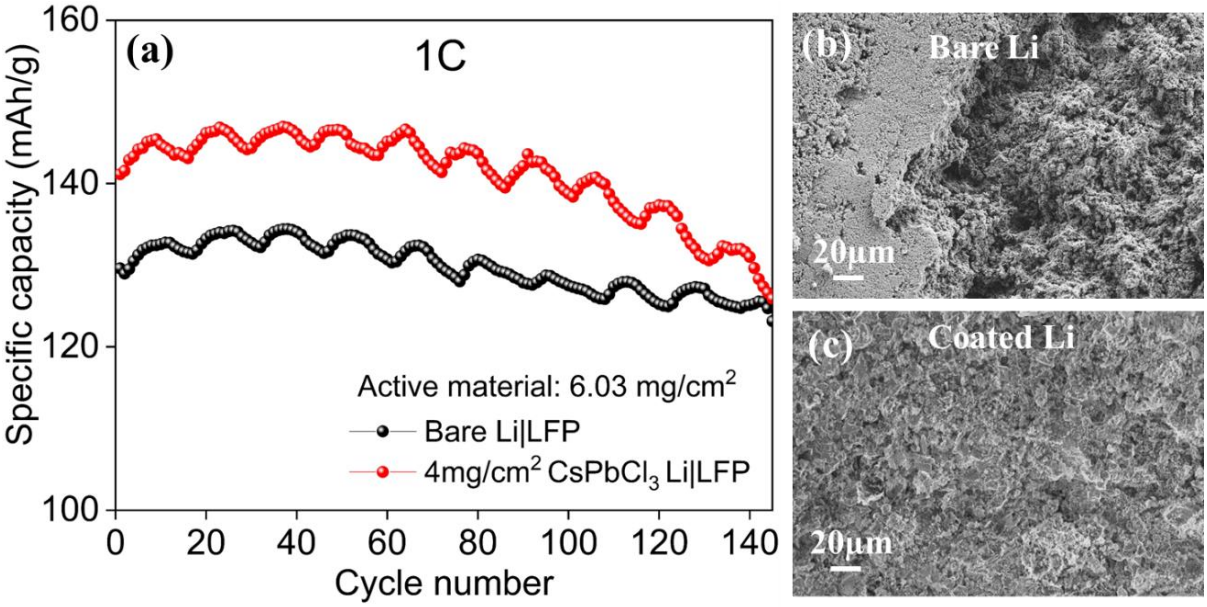

Fig. S5.(a) Long-term cycling stability of bare and coated Li||LFP full cell at 1C. SEM images of (b) bare Li and (c) coated Li after 20 cycles.

due to the porous and agglomerated nature of the coating, which leads to its structural failure. In contrast, such issues are mitigated in symmetric cells due to the large Li reservoir available. To investigate the morphological changes, postmortem SEM was performed (Fig. S5b). The bare Li electrode displayed a typical porous morphology with high surface area and significant amounts of dead Li, covering most of the electrode surface. In contrast, the coated Li electrode exhibited a distinctly different morphology from its pre-cycling state, which might be due to degradation of the coating during cycling. To address challenges such as coating agglomeration, undefined morphology, and the dual-phase nature of the perovskite, $CsPbCl_3$ was later synthesized via a solution-based method. This approach provides better control over coating uniformity and structural stability. The performance improvements associated with this new synthesis method will be discussed in the following section.

S4. Electrochemical characterization of ASEI on Li-metal in LP40

Since 1M LiFSI in FEC: DEC (1:2) represents an advanced electrolyte for Li-metal batteries. We extended our evaluation to LP 40. We performed Li plating/stripping of bare and coated Li||Li symmetric cells at a current density of 1 mA/cm^2 and an areal capacity of 1 mAh/cm^2. As can be seen in Fig. S6, the cell tested with bare Li-metal exhibited an initial overpotential of 195 mV. In contrast, the coated Li cell showed an overpotential of 71 mV. Significant differences appeared between the bare Li||Li cells and coated electrodes over extended cycling. The bare Li||Li symmetric cells showed a noticeable increase in overpotential after 50 h of cycling, and ultimately, short-circuiting occurred after 60 h due to the formation of HSAL. In contrast, the $CsPbCl_3$-coated Li||Li cells extended the cycle life of the Li-metal to 200 h with an increase in overpotential to 150 mV. The extended cycling life of the coated Li-metal electrodes in LP 40 demonstrates the protective layer's ability to improve cell stability.

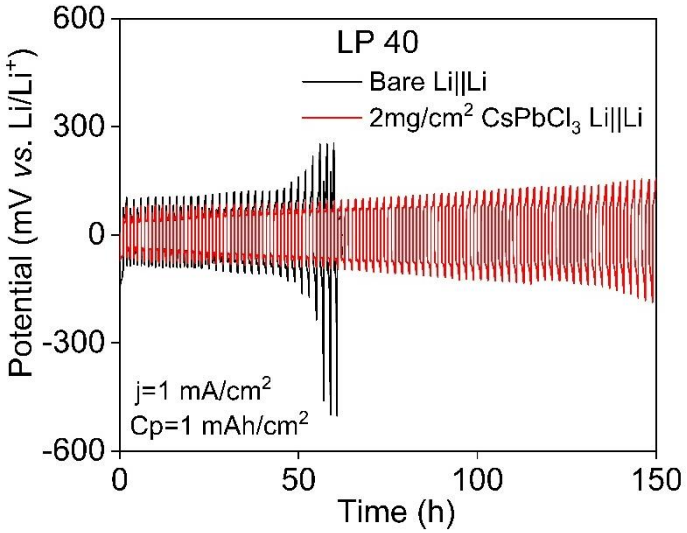

Fig. S6. Galvanostatic cycling of bare and coated Li||Li symmetric cells at a current density of 1 mA/cm^2 & areal capacity of 1 mAh/cm^2 in LP40.

S5. Study of $CsPbCl_3$ electrodes in 1M LiTFSI DOL: DME (1:1) + 1wt% $LiNO_3$

To extend this study, the electrochemical behavior of $CsPbCl_3$ was further investigated in an ether-based electrolyte (1 M LiTFSI in DOL: DME (1:1) with 1 wt% $LiNO_3$) to evaluate whether the conversion–alloying mechanism and phase evolution observed in carbonate

electrolyte are preserved, and to examine any differences in the discharge process or intermediate phases. The first discharge profile and corresponding *ex-situ* XRD patterns at selected potentials provide detailed insight into the reaction pathway in this ether-based system. Interestingly, the first discharge capacity of $CsPbCl_3$ (Fig. S7a) in the ether-based electrolyte was significantly higher (~1000 mAh/g) than in the carbonate-based electrolyte. This excess capacity may be associated with electrolyte decomposition, as DOL and DME are known to undergo reductive decomposition and polymerization at low potentials, forming SEI components such as Li alkoxides and polymeric species.[122] Therefore, while the fundamental conversion-alloying mechanism of $CsPbCl_3$ remains the same, the larger capacity in the ether-based electrolyte includes a substantial contribution from the irreversible electrolyte decomposition and SEI formation.

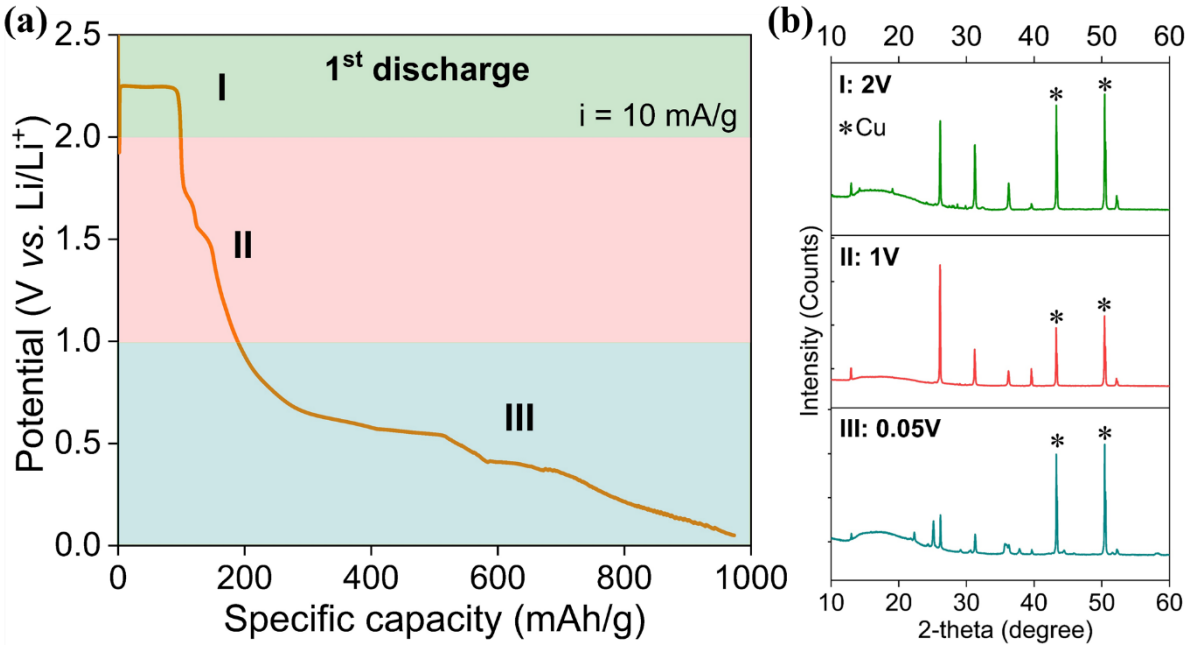

Fig. S7. (a) 1st cycle discharge curve and (b) *ex-situ* XRD pattern at different voltages of $CsPbCl_3$ anode cycled.

Ex-situ XRD analysis (Fig. S7b) shows that upon discharge to 2 V, the crystalline $CsPbCl_3$ phase is no longer observed, and new reflections corresponding to metallic Pb and Li_xPb_y alloy phases emerge. When discharged further to 0.05 V, the intensity of the alloy reflections increases, indicating progressive lithiation of Pb into intermetallic compounds. In addition to these expected phases, three unidentified peaks appear at ~13°, ~26°, and ~40°, which may correspond to intermediate or side products formed during the conversion reaction and require further investigation. The electrochemical behavior in the ether-based electrolyte (Fig. S8)

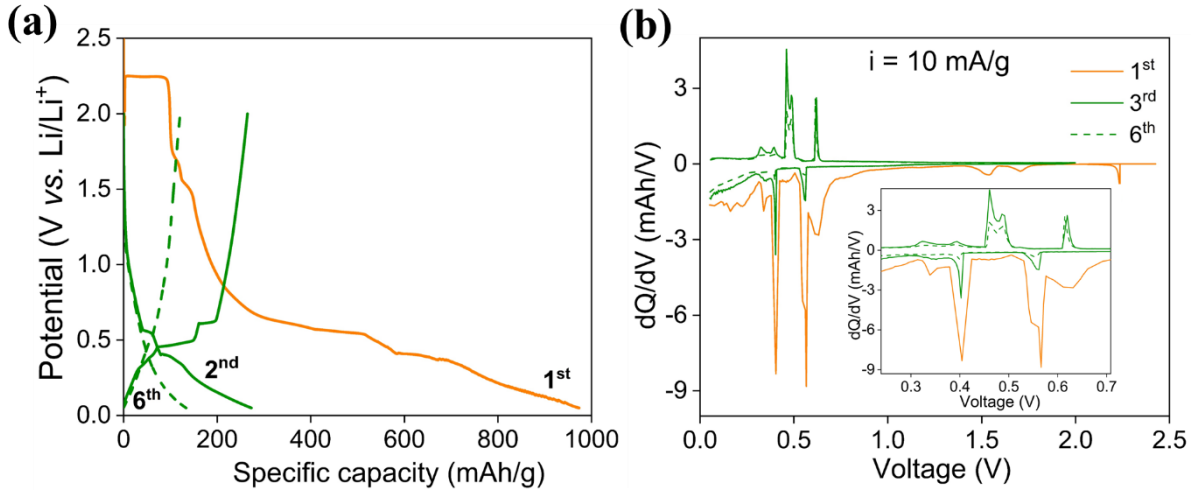

Fig. S8. Charge discharge profiles of $CsPbCl_3$ electrode and (b) their corresponding differential curves.

resembles that in the carbonate-based electrolyte, with a sharp decrease in capacity after the first discharge, likely associated with irreversible structural changes and the formation of inactive by-products. Moreover, the structural evolution of the perovskite-based electrode in an ether-based. After 30 cycles, the diffraction pattern and XPS show a similar structural evolution of $CsPbCl_3$ perovskite. While the overall trends point toward a conversion–alloying pathway, further detailed studies are necessary to fully understand the Li-transport mechanism in MHPs and how it is influenced by different electrolyte environments.

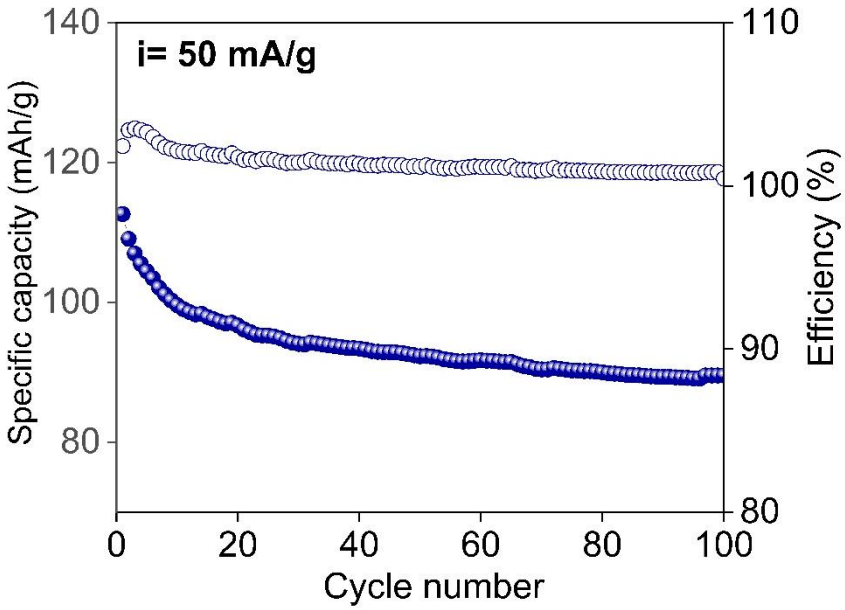

Fig. S9. (a) Related capacity retention and CE during prolonged cycling, up to 100 cycles at 50 mAh/g of $CsPbCl_3$||Li half cells (b) with corresponding galvanostatic charge/discharge profiles.

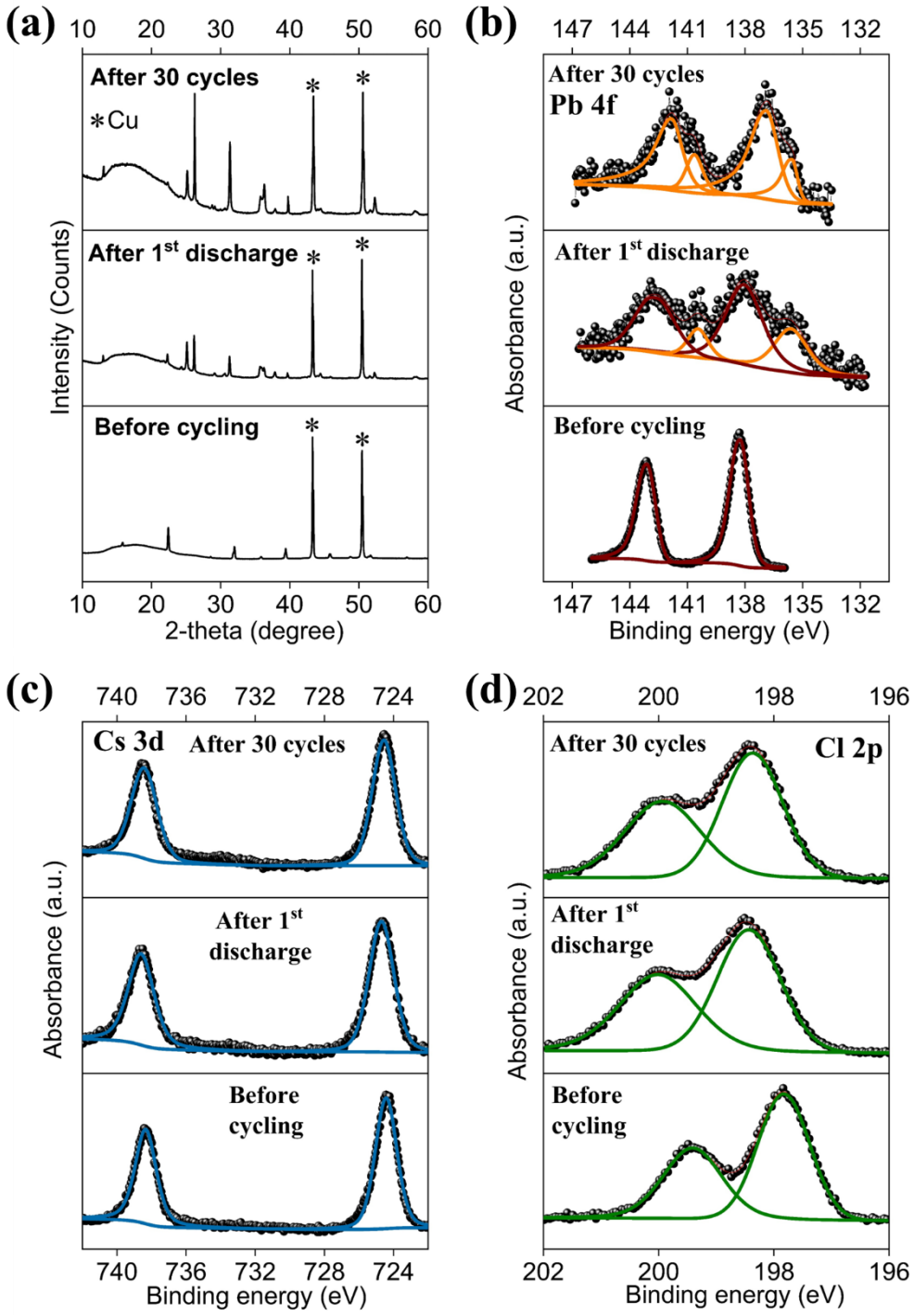

Fig. S10. (a) *Ex-situ* XRD pattern and (b-d) *ex-situ* XPS of $CsPbCl_3$ anode before cycling, after 1st discharge, and after 30 cycles.

References

1 M. Aneke and M. Wang, Energy storage technologies and real-life applications – A state of the art review, *Appl. Energy*, 2016, **179**, 350–377.

2 D. O. Akinyele and R. K. Rayudu, Review of energy storage technologies for sustainable power networks, *Sustain. Energy Technol. Assessments*, 2014, **8**, 74–91.

3 A. T. Nguyen, V. D. Phung, V. O. Mittova, H. D. Ngo, T. N. Vo, M. L. Le Thi, V. H. Nguyen, I. Y. Mittova, M. L. P. Le, Y. N. Ahn, I. T. Kim and T. L. Nguyen, Fabricating nanostructured $HoFeO_3$ perovskite for lithium-ion battery anodes via co-precipitation, *Scr. Mater.*, 2022, **207**, 114259.

4 Q. Wei, F. Xiong, S. Tan, L. Huang, E. H. Lan, B. Dunn and L. Mai, Porous One-Dimensional Nanomaterials: Design, Fabrication and Applications in Electrochemical Energy Storage, *Adv. Mater.*, 2017, **29**, 1602300.

5 C.-Y. Wang, T. Liu, X.-G. Yang, S. Ge, N. V. Stanley, E. S. Rountree, Y. Leng and B. D. McCarthy, Fast charging of energy-dense lithium-ion batteries, *Nature*, 2022, **611**, 485–490.

6 B. Nykvist and M. Nilsson, Rapidly falling costs of battery packs for electric vehicles, *Nat. Clim. Chang.*, 2015, **5**, 329–332.

7 S. Yang, Q. Liang, H. Wu, J. Pi, Z. Wang, Y. Luo, Y. Liu, Z. Long, D. Zhou, Y. Wen, Q. Wang, J. Guo and J. Qiu, Lead-Free Double Perovskite $Cs_2NaErCl_6 : Li^+$ as High-Stability Anodes for Li-Ion Batteries, *J. Phys. Chem. Lett.*, 2022, **13**, 4981–4987.

8 C. P. Grey and D. S. Hall, Prospects for lithium-ion batteries and beyond-a 2030 vision, *Nat. Commun.*, 2020, **11**, 6279.

9 P. U. Nzereogu, A. D. Omah, F. I. Ezema, E. I. Iwuoha and A. C. Nwanya, Anode materials for lithium-ion batteries: A review, *Appl. Surf. Sci. Adv.*, 2022, **9**, 100233.

10 P. Verma, P. Maire and P. Novák, A review of the features and analyses of the solid electrolyte interphase in Li-ion batteries, *Electrochim. Acta*, 2010, **55**, 6332–6341.

11 Al Bedwell, Alternatives to graphite in EV batteries. [Online]. Available; https://www.just-auto.com/features/alternatives-to-graphite-in-ev-batteries/.

12 E. Feyzi, A. K. M R, X. Li, S. Deng, J. Nanda and K. Zaghib, A comprehensive review of silicon anodes for high-energy lithium-ion batteries: Challenges, latest developments, and perspectives, *Next Energy*, 2024, **5**, 100176.

13 Z.-S. Wu, W. Ren, L. Xu, F. Li and H.-M. Cheng, Doped Graphene Sheets As Anode

Materials with Superhigh Rate and Large Capacity for Lithium Ion Batteries, *ACS Nano*, 2011, **5**, 5463–5471.

14 M. N. Obrovac and V. L. Chevrier, Alloy Negative Electrodes for Li-Ion Batteries, *Chem. Rev.*, 2014, **114**, 11444–11502.

15 W.-J. Zhang, A review of the electrochemical performance of alloy anodes for lithium-ion batteries, *J. Power Sources*, 2011, **196**, 13–24.

16 C.-M. Park, J.-H. Kim, H. Kim and H.-J. Sohn, Li-alloy based anode materials for Li secondary batteries, *Chem. Soc. Rev.*, 2010, **39**, 3115.

17 E. Kim, H. An, I. Kang, C. Lee, M. An, S. Chae and Y. Son, Physical limitations of electrode conditions for graphite/Si blended anodes toward high-energy Li-ion batteries, *J. Power Sources*, 2025, **632**, 236314.

18 D. Andre, H. Hain, P. Lamp, F. Maglia and B. Stiaszny, Future high-energy density anode materials from an automotive application perspective, *J. Mater. Chem. A*, 2017, **5**, 17174–17198.

19 F. T. Krauss, I. Pantenburg and B. Roling, Transport of Ions, Molecules, and Electrons across the Solid Electrolyte Interphase: What Is Our Current Level of Understanding?, *Adv. Mater. Interfaces*, 2022, **9**, 8.

20 E. Peled, D. Golodnitsky and G. Ardel, Advanced Model for Solid Electrolyte Interphase Electrodes in Liquid and Polymer Electrolytes, *J. Electrochem. Soc.*, 1997, **144**, L208–L210.

21 E. Peled, The Electrochemical Behavior of Alkali and Alkaline Earth Metals in Nonaqueous Battery Systems—The Solid Electrolyte Interphase Model, *J. Electrochem. Soc.*, 1979, **126**, 2047–2051.

22 P. G. Bruce, S. A. Freunberger, L. J. Hardwick and J.-M. Tarascon, Li–O_2 and Li–S batteries with high energy storage, *Nat. Mater.*, 2012, **11**, 19–29.

23 H. Qutaish, S. A. Han, Y. Rehman, K. Konstantinov, M.-S. Park and J. Ho Kim, Porous carbon architectures with different dimensionalities for lithium metal storage, *Sci. Technol. Adv. Mater.*, 2022, **23**, 169–188.

24 B. Jagger and M. Pasta, Solid electrolyte interphases in lithium metal batteries, *Joule*, 2023, **7**, 2228–2244.

25 R. W. Schmitz, P. Murmann, R. Schmitz, R. Müller, L. Krämer, J. Kasnatscheew, P. Isken, P. Niehoff, S. Nowak, G.-V. Röschenthaler, N. Ignatiev, P. Sartori, S. Passerini, M. Kunze, A. Lex-Balducci, C. Schreiner, I. Cekic-Laskovic and M. Winter, Investigations on novel electrolytes, solvents and SEI additives for use in lithium-ion

batteries: Systematic electrochemical characterization and detailed analysis by spectroscopic methods, *Prog. Solid State Chem.*, 2014, **42**, 65–84.

26 K. Qin, K. Holguin, M. Mohammadiroudbari, J. Huang, E. Y. S. Kim, R. Hall and C. Luo, Strategies in Structure and Electrolyte Design for High-Performance Lithium Metal Batteries, *Adv. Funct. Mater.*, 2021, **31**, 15.

27 M. V. Ordaz, N. Pavlin, M. Gastaldi, C. Gerbaldi and R. Dominko, Protective Coating for Stable Cycling of Li-Metal Batteries Based on Cellulose and Single-Ion Conducting Polymer, *ACS Appl. Mater. Interfaces*, 2024, **16**, 68237–68246.

28 W. Cao, J. Lu, K. Zhou, G. Sun, J. Zheng, Z. Geng and H. Li, Organic-inorganic composite SEI for a stable Li metal anode by in-situ polymerization, *Nano Energy*, 2022, **95**, 106983.

29 W. Wu, D. Ning, J. Zhang, G. Liu, L. Zeng, H. Yao, M. Wang, L. Deng and L. Yao, Ultralight lithiophilic three-dimensional lithium host for stable high-energy-density anode-free lithium metal batteries, *Energy Storage Mater.*, 2023, **63**, 102974.

30 Z. Li, X. Huang, L. Kong, N. Qin, Z. Wang, L. Yin, Y. Li, Q. Gan, K. Liao, S. Gu, T. Zhang, H. Huang, L. Wang, G. Luo, X. Cheng and Z. Lu, Gradient nano-recipes to guide lithium deposition in a tunable reservoir for anode-free batteries, *Energy Storage Mater.*, 2022, **45**, 40–47.

31 H. A. Ishfaq, C. Cruz Cardona, E. Tchernychova, P. Johansson, R. Dominko and S. Drvarič Talian, Enhanced performance of lithium metal batteries via cyclic fluorinated ether based electrolytes, *Energy Storage Mater.*, 2024, **69**, 103375.

32 Y. Zhao, T. Zhou, M. Mensi, J. W. Choi and A. Coskun, Electrolyte engineering via ether solvent fluorination for developing stable non-aqueous lithium metal batteries, *Nat. Commun.*, 2023, **14**, 299.

33 Y. Cui, G. Yu, R. Liu, D. Miao and D. Wu, Quasi-Solid-State Composite Electrolytes with Multifunctional 2D Molecular Brush Fillers for Long-Cycling Lithium Metal Batteries, Chinese J. Chem., 2023, **41**, 2848–2854.

34 W. Luo, Y. Gong, Y. Zhu, Y. Li, Y. Yao, Y. Zhang, K. (Kelvin) Fu, G. Pastel, C. Lin, Y. Mo, E. D. Wachsman and L. Hu, Reducing Interfacial Resistance between Garnet-Structured Solid-State Electrolyte and Li-Metal Anode by a Germanium Layer, *Adv. Mater.*, 2017, **29**, 22.

35 A. Zhamu, G. Chen, C. Liu, D. Neff, Q. Fang, Z. Yu, W. Xiong, Y. Wang, X. Wang, and B. Z. Jang, Reviving rechargeable lithium metal batteries: enabling next-generation high-energy and high-power cells, *Energy Environ. Sci.*, 2012, **5**, 5701–5707.

36 R. Liu, W. Feng, L. Fang, H. Deng, L. Lin, M. Chen, J.-X. Zhong and W. Yin, An ultrathin Li-doped perovskite SEI film with high Li ion flux for a fast charging lithium metal battery, *Energy Adv.*, 2024, **3**, 2999–3006.

37 J. Lopez, A. Pei, J. Y. Oh, G.-J. N. Wang, Y. Cui and Z. Bao, Effects of Polymer Coatings on Electrodeposited Lithium Metal, *J. Am. Chem. Soc.*, 2018, **140**, 11735–11744.

38 A. C. Kozen, C.-F. Lin, O. Zhao, S. B. Lee, G. W. Rubloff and M. Noked, Stabilization of Lithium Metal Anodes by Hybrid Artificial Solid Electrolyte Interphase, *Chem. Mater.*, 2017, **29**, 6298–6307.

39 R. Xu, X.-B. Cheng, C. Yan, X.-Q. Zhang, Y. Xiao, C.-Z. Zhao, J.-Q. Huang and Q. Zhang, Artificial Interphases for Highly Stable Lithium Metal Anode, *Matter*, 2019, **1**, 317–344.

40 W. Zhang, G. E. Eperon and H. J. Snaith, Metal halide perovskites for energy applications, *Nat. Energy*, 2016, **1**, 16048.

41 J. Y. Kim, J.-W. Lee, H. S. Jung, H. Shin and N.-G. Park, High-Efficiency Perovskite Solar Cells, *Chem. Rev.*, 2020, **120**, 7867–7918.

42 C. Yang, W. Hu, J. Liu, C. Han, Q. Gao, A. Mei, Y. Zhou, F. Guo and H. Han, Achievements, challenges, and future prospects for industrialization of perovskite solar cells, *Light Sci. Appl.*, 2024, **13**, 227.

43 J. Han, K. Park, S. Tan, Y. Vaynzof, J. Xue, E. W.-G. Diau, M. G. Bawendi, J.-W. Lee and I. Jeon, Perovskite solar cells, *Nat. Rev. Methods Prim.*, 2025, **5**, 3.

44 L. Yuan, Q. Xue, F. Wang, N. Li, G. I. N. Waterhouse, C. J. Brabec, F. Gao and K. Yan, Perovskite Solar Cells and Light Emitting Diodes: Materials Chemistry, Device Physics and Relationship, *Chem. Rev.*, 2025, **125**, 5057–5162.

45 A. Kojima, K. Teshima, Y. Shirai and T. Miyasaka, Organometal Halide Perovskites as Visible-Light Sensitizers for Photovoltaic Cells, *J. Am. Chem. Soc.*, 2009, **131**, 6050–6051.

46 M. Cheng, Y. Duan, D. Zhang, Z. Xie, H. Li, Q. Cao, Z. Qiu, Y. Chen and Q. Peng, Tailoring Buried Interface and Minimizing Energy Loss Enable Efficient Narrow and Wide Bandgap Inverted Perovskite Solar Cells by Aluminum Glycinate Based Organometallic Molecule, *Adv. Mater.*, 2025, **37**, 10.

47 S. Liu, J. Li, W. Xiao, R. Chen, Z. Sun, Y. Zhang, X. Lei, S. Hu, M. Kober-Czerny, J. Wang, F. Ren, Q. Zhou, H. Raza, Y. Gao, Y. Ji, S. Li, H. Li, L. Qiu, W. Huang, Y. Zhao, B. Xu, Z. Liu, H. J. Snaith, N.-G. Park and W. Chen, Buried interface molecular hybrid for inverted perovskite solar cells, *Nature*, 2024, **632**, 536–542.

48 X.-K. Liu, W. Xu, S. Bai, Y. Jin, J. Wang, R. H. Friend and F. Gao, Metal halide perovskites for light-emitting diodes, *Nat. Mater.*, 2021, **20**, 10–21.

49 Y. Fu, H. Zhu, J. Chen, M. P. Hautzinger, X.-Y. Zhu and S. Jin, Metal halide perovskite nanostructures for optoelectronic applications and the study of physical properties, *Nat. Rev. Mater.*, 2019, **4**, 169–188.

50 L. A. Muscarella and E. M. Hutter, Halide Double-Perovskite Semiconductors beyond Photovoltaics, *ACS Energy Lett.*, 2022, **7**, 2128–2135.

51 H. Dong, C. Ran, W. Gao, M. Li, Y. Xia and W. Huang, Metal Halide Perovskite for next-generation optoelectronics: progresses and prospects, *eLight*, 2023, **3**, 3.

52 W. Gao, C. Chen, C. Ran, H. Zheng, H. Dong, Y. Xia, Y. Chen and W. Huang, A-Site Cation Engineering of Metal Halide Perovskites: Version 3.0 of Efficient Tin-Based Lead-Free Perovskite Solar Cells, *Adv. Funct. Mater.*, 2020, **30**, 34.

53 T. Oku, Crystal structures of perovskite halide compounds used for solar cells, *Rev. Adv. Mater. Sci.*, 2020, **59**, 264–305.

54 H. Tanaka, T. Oku and N. Ueoka, Structural stabilities of organic–inorganic perovskite crystals, *Jpn. J. Appl. Phys.*, 2018, **57**, 08RE12.

55 Z. Li, M. Yang, J.-S. Park, S.-H. Wei, J. J. Berry and K. Zhu, Stabilizing Perovskite Structures by Tuning Tolerance Factor: Formation of Formamidinium and Cesium Lead Iodide Solid-State Alloys, *Chem. Mater.*, 2016, **28**, 284–292.

56 Y. Wang, J. Ren, X. Zhou and G. Zhang, Stability improvements of metal halide perovskite nanocrystals and their optoelectrical applications, *Mater. Chem. Front.*, 2023, **7**, 2175–2207.

57 W. Gao, C. Chen, C. Ran, H. Zheng, H. Dong, Y. Xia, Y. Chen and W. Huang, A-Site Cation Engineering of Metal Halide Perovskites: Version 3.0 of Efficient Tin-Based Lead-Free Perovskite Solar Cells, *Adv. Funct. Mater.*, 2020, **30**, 2000794.

58 D. Duan, C. Ge, M. Z. Rahaman, C.-H. Lin, Y. Shi, H. Lin, H. Hu and T. Wu, Recent progress with one-dimensional metal halide perovskites: from rational synthesis to optoelectronic applications, *NPG Asia Mater.*, 2023, **15**, 8.

59 J. Huang, Y. Yuan, Y. Shao and Y. Yan, Understanding the physical properties of hybrid perovskites for photovoltaic applications, *Nat. Rev. Mater.*, 2017, **2**, 17042.

60 J.-W. Lee, S. Tan, S. Il Seok, Y. Yang and N.-G. Park, Rethinking the A cation in halide perovskites, *Science.*, 2022, **375**, 6583.

61 M. G. Goesten and R. Hoffmann, Mirrors of Bonding in Metal Halide Perovskites, *J. Am. Chem. Soc.*, 2018, **140**, 12996–13010.

62 J. Han, Y. Li, P. Zhang, B. Xu, X. Xu and Z. Quan, Cooperative Regulation of ns^2 Lone-Pair Expression Realizes Distinct Excitonic Emissions in Hybrid Germanium, Tin, and Lead Halides, *J. Am. Chem. Soc.*, 2025, **147**, 1291–1299.

63 I. Y. H Chang, C. H. Park and K. Matsuishi, First-Principles Study of the Structural and the Electronic Properties of the Lead-Halide-Based Inorganic-Organic Perovskites $(CH_3NH_3)PbX_3$ and $CsPbX_3$ (X= Cl, Br, I), 2004, **44**, 889-893.

64 C. W. Myung, J. Yun, G. Lee and K. S. Kim, A New Perspective on the Role of A-Site Cations in Perovskite Solar Cells, *Adv. Energy Mater.*, 2018, **8**, 1702898.

65 G. E. Eperon, S. D. Stranks, C. Menelaou, M. B. Johnston, L. M. Herz and H. J. Snaith, Formamidinium lead trihalide: a broadly tunable perovskite for efficient planar heterojunction solar cells, *Energy Environ. Sci.*, 2014, **7**, 982.

66 J. Qin, Z. Che, Y. Kang, C. Liu, D. Wu, H. Yang, X. Hu and Y. Zhan, Towards operation-stabilizing perovskite solar cells: Fundamental materials, device designs, and commercial applications, *InfoMat*., 2024, **6**, e12522

67 M. Nishat, M. K. Hossain, M. R. Hossain, S. Khanom, F. Ahmed and M. A. Hossain, Role of metal and anions in organo-metal halide perovskites $CH_3NH_3MX_3$ (M: Cu, Zn, Ga, Ge, Sn, Pb; X: Cl, Br, I) on structural and optoelectronic properties for photovoltaic applications, *RSC Adv.*, 2022, **12**, 13281–13294.

68 A. Soultati, M. Tountas, K. K. Armadorou, A. R. bin M. Yusoff, M. Vasilopoulou and M. K. Nazeeruddin, Synthetic approaches for perovskite thin films and single-crystals, *Energy Adv.*, 2023, **2**, 1075–1115.

69 S. Tao, I. Schmidt, G. Brocks, J. Jiang, I. Tranca, K. Meerholz and S. Olthof, Absolute energy level positions in tin- and lead-based halide perovskites, *Nat. Commun.*, 2019, **10,** 2560.

70 K. Chen, S. Schünemann, S. Song and H. Tüysüz, Structural effects on optoelectronic properties of halide perovskites, *Chem. Soc. Rev.*, 2018, **47**, 7045–7077.

71 A. Alaei, A. Circelli, Y. Yuan, Y. Yang and S. S. Lee, Polymorphism in metal halide perovskites, *Mater. Adv.*, 2021, **2**, 47–63.

72 M. Saski, S. Sobczak, P. Ratajczyk, M. Terlecki, W. Marynowski, A. Borkenhagen, I. Justyniak, A. Katrusiak and J. Lewiński, Unprecedented Richness of Temperature- and Pressure-Induced Polymorphism in 1D Lead Iodide Perovskite, *Small.*, 2024, **20**, 2403685.

73 M. Simenas, A. Gagor, J. Banys and M. Maczka, Phase Transitions and Dynamics in Mixed Three- and Low-Dimensional Lead Halide Perovskites, *Chem. Rev.*, 2024, 124,

2281–2326.

74 H. Jin, Y.-J. Zeng, J. A. Steele, M. B. J. Roeffaers, J. Hofkens and E. Debroye, Phase stabilization of cesium lead iodide perovskites for use in efficient optoelectronic devices, *NPG Asia Mater.*, 2024, **16**, 24.

75 A. Marronnier, G. Roma, S. Boyer-Richard, L. Pedesseau, J.-M. Jancu, Y. Bonnassieux, C. Katan, C. C. Stoumpos, M. G. Kanatzidis and J. Even, Anharmonicity and Disorder in the Black Phases of Cesium Lead Iodide Used for Stable Inorganic Perovskite Solar Cells, *ACS Nano*, 2018, **12**, 3477–3486.

76 L. Kong, G. Liu, J. Gong, Q. Hu, R. D. Schaller, P. Dera, D. Zhang, Z. Liu, W. Yang, K. Zhu, Y. Tang, C. Wang, S.-H. Wei, T. Xu and H. Mao, Simultaneous band-gap narrowing and carrier-lifetime prolongation of organic–inorganic trihalide perovskites, *Proc. Natl. Acad. Sci.*, 2016, **113**, 8910–8915.

77 D. D. Nematov, A. S. Burkhonzoda, M. S. Kurboniyon, U. Zafari, K. T. Kholmurodov, M. G. Brik, T. Yamamoto and F. Shokir, The Effect of Phase Changes on Optoelectronic Properties of Lead-Free CsSnI3 Perovskites, *J. Electron. Mater.*, 2025, **54**, 1634–1644.

78 P. Zhu and J. Zhu, Low-dimensional metal halide perovskites and related optoelectronic applications, *InfoMat*, 2020, **2**, 341–378.

79 G. Wang, S. Mei, J. Liao, W. Wang, Y. Tang, Q. Zhang, Z. Tang, B. Wu and G. Xing, Advances of Nonlinear Photonics in Low-Dimensional Halide Perovskites, *Small.*, 2021, **17**, 2100809.

80 M. Li, R. Begum, J. Fu, Q. Xu, T. M. Koh, S. A. Veldhuis, M. Grätzel, N. Mathews, S. Mhaisalkar and T. C. Sum, Low threshold and efficient multiple exciton generation in halide perovskite nanocrystals, *Nat. Commun.*, 2018, **9**, 4197.

81 M. C. Brennan, J. E. Herr, T. S. Nguyen-Beck, J. Zinna, S. Draguta, S. Rouvimov, J. Parkhill and M. Kuno, Origin of the Size-Dependent Stokes Shift in $CsPbBr_3$ Perovskite Nanocrystals, *J. Am. Chem. Soc.*, 2017, **139**, 12201–12208.

82 P. Vashishtha, D. Z. Metin, M. E. Cryer, K. Chen, J. M. Hodgkiss, N. Gaston and J. E. Halpert, Shape-, Size-, and Composition-Controlled Thallium Lead Halide Perovskite Nanowires and Nanocrystals with Tunable Band Gaps, *Chem. Mater.*, 2018, **30**, 2973–2982.

83 K. Leng, I. Abdelwahab, I. Verzhbitskiy, M. Telychko, L. Chu, W. Fu, X. Chi, N. Guo, Z. Chen, Z. Chen, C. Zhang, Q.-H. Xu, J. Lu, M. Chhowalla, G. Eda and K. P. Loh, Molecularly thin two-dimensional hybrid perovskites with tunable optoelectronic properties due to reversible surface relaxation, *Nat. Mater.*, 2018, **17**, 908–914.

84 J. Xing, Y. Zhao, M. Askerka, L. N. Quan, X. Gong, W. Zhao, J. Zhao, H. Tan, G. Long, L. Gao, Z. Yang, O. Voznyy, J. Tang, Z.-H. Lu, Q. Xiong and E. H. Sargent, Color-stable highly luminescent sky-blue perovskite light-emitting diodes, *Nat. Commun.*, 2018, **9**, 3541.

85 H.-R. Xia, W.-T. Sun and L.-M. Peng, Hydrothermal synthesis of organometal halide perovskites for Li-ion batteries, *Chem. Commun.*, 2015, **51**, 13787–13790.

86 J. A. Dawson, A. J. Naylor, C. Eames, M. Roberts, W. Zhang, H. J. Snaith, P. G. Bruce and M. S. Islam, Mechanisms of Lithium Intercalation and Conversion Processes in Organic–Inorganic Halide Perovskites, *ACS Energy Lett.*, 2017, **2**, 1818–1824.

87 N. Vicente and G. Garcia-Belmonte, Methylammonium Lead Bromide Perovskite Battery Anodes Reversibly Host High Li-Ion Concentrations, *J. Phys. Chem. Lett.*, 2017, **8**, 1371–1374.

88 N. Vicente, D. Bresser, S. Passerini and G. Garcia-Belmonte, Probing the 3-step Lithium Storage Mechanism in $CH_3NH_3PbBr_3$ Perovskite Electrode by *Operando* -XRD Analysis, *ChemElectroChem*, 2019, **6**, 456–460.

89 P. Pal and A. Ghosh, Three-Dimensional $CsPbCl_3$ Perovskite Anode for Quasi-Solid-State Li-Ion and Dual-Ion Batteries: Mechanism of Li^+ Conversion Process in Perovskite, *Phys. Rev. Appl.*, 2020, **14**, 064010.

90 X.-H. Wu, M.-J. Zhao, Y. Chai, Z. Liu, W.-J. Jiang, L.-B. Yang, B.-J. Feng, J.-J. Liu, Q. Yu, K.-Z. Du and Y. Zhao, Unlocking the atomic-scale mechanism of structural evolutions during (de)lithiation and negative-fading in CsPbBr3 anodes, *Energy Storage Mater.*, 2025, **75**, 104043.

91 N. Kaisar, T. Paul, P.-W. Chi, Y.-H. Su, A. Singh, C.-W. Chu, M.-K. Wu and P. M. Wu, Electrochemical Performance of Orthorhombic $CsPbI_3$ Perovskite in Li-Ion Batteries, *Materials (Basel).*, 2021, **14**, 5718.

92 D. Ramirez, Y. Suto, N. C. Rosero-Navarro, A. Miura, K. Tadanaga and F. Jaramillo, Structural and Electrochemical Evaluation of Three- and Two-Dimensional Organohalide Perovskites and Their Influence on the Reversibility of Lithium Intercalation, *Inorg. Chem.*, 2018, **57**, 4181–4188.

93 L. T. López, D. Ramírez, F. Jaramillo and J. A. Calderón, Novel hybrid organic-inorganic $CH_3NH_3NiCl_3$ active material for high-capacity and sustainable lithium-ion batteries, *Electrochim. Acta*, 2020, **357**, 136882.

94 Q. Wang, T. Yang, H. Wang, J. Zhang, X. Guo, Z. Yang, S. Lu and W. Qin, Morphological and chemical tuning of lead halide perovskite mesocrystals as long-life

anode materials in lithium-ion batteries, *CrystEngComm*, 2019, **21**, 1048–1059.

95 Q. Jiang, M. Chen, J. Li, M. Wang, X. Zeng, T. Besara, J. Lu, Y. Xin, X. Shan, B. Pan, C. Wang, S. Lin, T. Siegrist, Q. Xiao and Z. Yu, Electrochemical Doping of Halide Perovskites with Ion Intercalation, *ACS Nano*, 2017, **11**, 1073–1079.

96 S. Liu, K. Zhang, L. Tan, S. Qi, G. Liu, J. Chen and Y. Lou, All-inorganic halide perovskite $CsPbBr_3$@CNTs composite enabling superior lithium storage performance with pseudocapacitive contribution, *Electrochim. Acta*, 2021, **367**, 137352.

97 M. Tathavadekar, S. Krishnamurthy, A. Banerjee, S. Nagane, Y. Gawli, A. Suryawanshi, S. Bhat, D. Puthusseri, A. D. Mohite and S. Ogale, Low-dimensional hybrid perovskites as high-performance anodes for alkali-ion batteries, *J. Mater. Chem. A*, 2017, **5**, 18634–18642.

98 X.-Q. Zhang, X.-B. Cheng, X. Chen, C. Yan and Q. Zhang, Fluoroethylene Carbonate Additives to Render Uniform Li Deposits in Lithium Metal Batteries, *Adv. Funct. Mater.*, 2017, **27**, 1605989.

99 Y.-G. Lee, S. Ryu, T. Sugimoto, T. Yu, W. Chang, Y. Yang, C. Jung, J. Woo, S. G. Kang, H. N. Han, S.-G. Doo, Y. Hwang, H. Chang, J.-M. Lee, and J.-Y. Sun, Dendrite-Free Lithium Deposition for Lithium Metal Anodes with Interconnected Microsphere Protection, *Chem. Mater.*, 2017, **29**, 5906–5914.

100 D. Rehnlund, F. Lindgren, S. Böhme, T. Nordh, Y. Zou, J. Pettersson, U. Bexell, M. Boman, K. Edström, and L. Nyholm, Lithium trapping in alloy forming electrodes and current collectors for lithium-based batteries, *Energy Environ. Sci.*, 2017, **10**, 1350–1357.

101 S. Rajendran, N. K. Thangavel, K. Mahankali, and L. M. R. Arava, Toward Moisture-Stable and Dendrite-Free Garnet-Type Solid-State Electrolytes, *ACS Appl. Energy Mater.*, 2020, **3**, 6775–6784.

102 X.-B. Cheng, T.-Z. Hou, R. Zhang, H.-J. Peng, C.-Z. Zhao, J.-Q. Huang and Q. Zhang, Dendrite-Free Lithium Deposition Induced by Uniformly Distributed Lithium Ions for Efficient Lithium Metal Batteries, *Adv. Mater.*, 2016, **28**, 2888–2895.

103 X.-B. Cheng, C. Yan, X. Chen, C. Guan, J.-Q. Huang, H.-J. Peng, R. Zhang, S.-T. Yang and Q. Zhang, Implantable Solid Electrolyte Interphase in Lithium-Metal Batteries, *Chem*, 2017, **2**, 258–270.

104 F. Ding, W. Xu, G. L. Graff, J. Zhang, M. L. Sushko, X. Chen, Y. Shao, M. H. Engelhard, Z. Nie, J. Xiao, X. Liu, P. V. Sushko, J. Liu, and J.-G. Zhang, Dendrite-Free Lithium Deposition via Self-Healing Electrostatic Shield Mechanism, *J. Am. Chem. Soc.*, 2013,

135, 4450–4456.

105 N. Liu, J. Baek, S. M. Kim, S. Hong, Y. K. Hong, Y. S. Kim, H.-S. Kim, S. Kim and J. Park, Improving the Stability of High-Performance Multilayer MoS_2 Field-Effect Transistors, *ACS Appl. Mater. Interfaces*, 2017, **9**, 42943–42950.

106 Q. Wu, G. Wang, Q. Huang, S. Xie, J. Huang and X. Wang, Perovskite-type $La_{0.6}Sr_{0.4}Co_{0.2}Fe_{0.8}O_{3-\delta}$ as an artificial interphase layer for dendrite-free Li metal anodes, *Chem. Eng. J.*, 2022, **444**, 136340.

107 Z. Yu, Y. Cui and Z. Bao, Design Principles of Artificial Solid Electrolyte Interphases for Lithium-Metal Anodes, *Cell Reports Phys. Sci.*, 2020, **1**, 100119.

108 X.-B. Cheng, R. Zhang, C.-Z. Zhao and Q. Zhang, Toward Safe Lithium Metal Anode in Rechargeable Batteries: A Review, *Chem. Rev.*, 2017, **117**, 10403–10473.

109 Y. Zhang, Y. Liu, J. Zhou, D. Wang, L. Tan and C. Yi, 3D cubic framework of fluoride perovskite SEI inducing uniform lithium deposition for air-stable and dendrite-free lithium metal anodes, *Chem. Eng. J.*, 2022, **431**, 134266.

110 Y.-C. Yin, Q. Wang, J.-T. Yang, F. Li, G. Zhang, C.-H. Jiang, H.-S. Mo, J.-S. Yao, K.-H. Wang, F. Zhou, H.-X. Ju and H.-B. Yao, Metal chloride perovskite thin film-based interfacial layer for shielding lithium metal from liquid electrolyte, *Nat. Commun.*, 2020, **11**, 1761.

111 N. Kaisar, A. Singh, P.-Y. Yang, Y.-T. Chen, S. Li, C.-W. Pao, S. Jou and C.-W. Chu, Long-lifespan lithium–metal batteries obtained using a perovskite intercalation layer to stabilize the lithium electrode, *J. Mater. Chem. A*, 2020, **8**, 9137–9145.

112 C. Yi, J. Luo, S. Meloni, A. Boziki, N. Ashari-Astani, C. Grätzel, S. M. Zakeeruddin, U. Röthlisberger and M. Grätzel, Entropic stabilization of mixed A-cation ABX_3 metal halide perovskites for high performance perovskite solar cells, *Energy Environ. Sci.*, 2016, **9**, 656–662.

113 S. Bai, P. Da, C. Li, Z. Wang, Z. Yuan, F. Fu, M. Kawecki, X. Liu, N. Sakai, J. T.-W. Wang, S. Huettner, S. Buecheler, M. Fahlman, F. Gao and H. J. Snaith, Planar perovskite solar cells with long-term stability using ionic liquid additives, *Nature*, 2019, **571**, 245–250.

114 M. Kim, G.-H. Kim, T. K. Lee, I. W. Choi, H. W. Choi, Y. Jo, Y. J. Yoon, J. W. Kim, J. Lee, D. Huh, H. Lee, S. K. Kwak, J. Y. Kim and D. S. Kim, Methylammonium Chloride Induces Intermediate Phase Stabilization for Efficient Perovskite Solar Cells, *Joule*, 2019, **3**, 2179–2192.

115 Y. W. Peng, C. P. Wang, G. Kumar, P. L. Hsieh, C. M. Hsieh and M. H. Huang,

Formation of $CsPbCl_3$ Cubes and Edge-Truncated Cuboids at Room Temperature, *ACS Sustain. Chem. Eng.*, 2022, **10**, 1578–1584.

116 J. Bobnar, A. Vizintin, G. Kapun, C. Njel, R. Dedryvère, R. Dominko and B. Genorio, A New Cell Configuration for a More Precise Electrochemical Evaluation of an Artificial Solid-Electrolyte Interphase, *Batter. Supercaps*, 2021, **4**, 623–631.

117 C. Xie, X. Zhang, H. S. Chen and P. Yang, Synthesis-Kinetics of Violet- and Blue-Emitting Perovskite Nanocrystals with High Brightness and Superior Stability toward Flexible Conversion Layer, *Small*, 2024, **20**, 19.

118 K. N. Wood, E. Kazyak, A. F. Chadwick, K.-H. Chen, J.-G. Zhang, K. Thornton and N. P. Dasgupta, Dendrites and Pits: Untangling the Complex Behavior of Lithium Metal Anodes through Operando Video Microscopy, *ACS Cent. Sci.*, 2016, **2**, 790–801.

119 S. Drvarič Talian, G. Kapun, J. Moškon, R. Dominko and M. Gaberšček, Operando impedance spectroscopy with combined dynamic measurements and overvoltage analysis in lithium metal batteries, *Nat. Commun.*, 2025, **16**, 2030.

120 X. Wang, Y. He, S. Tu, L. Fu, Z. Chen, S. Liu, Z. Cai, L. Wang, X. He and Y. Sun, Li plating on alloy with superior electro-mechanical stability for high energy density anode-free batteries, *Energy Storage Mater.*, 2022, **49**, 135–143.

121 X. Liu, R. Wei, S. Fu, W. Xie, S. Xu and J. Zhang, Cs_4PbBr_6 QDs silicate glass-ceramic: A potential anode material for LIBs, *Ceram. Int.*, 2022, **48**, 23293–23299.

122 L. Lodovico, A. Varzi and S. Passerini, Radical Decomposition of Ether-Based Electrolytes for Li-S Batteries, *J. Electrochem. Soc.*, 2017, **164**, A1812–A1819.